BULGARIAN CHEMICAL COMMUNICATIONS

2014 Volume 46 / Number 3 Supplement

Journal of the Chemical Institutes
of the Bulgarian Academy of Sciences
and of the Union of Chemists in Bulgaria

Bulgarian Chemical Communications, Volume 46, Number 3 (pp. 602 – 610) 2014

Structural transitions in the acid-denatured ficin induced by halogenols and alkanols

M.S. Zaroog[1,2], H.A. Kadir[1], S. Tayyab[1]*

[1]*Biomolecular Research Group, Biochemistry Programme, Institute of Biological Sciences, Faculty of Science, University of Malaya, 50603 Kuala Lumpur, Malaysia*

[2]*Present address: Faculty of Applied Medical Sciences, University of Gezira, P.O. Box 20, Wad Medani, Sudan*

Received March 27, 2013; Revised April 24, 2014

The effect of eight different alcohols including halogenols and alkanols on the structural transformation of acid-denatured ficin (ADF) at pH 2.5 was studied using far- and near-UV circular dichroism (CD) and tryptophan fluorescence. Except methanol and ethanol, other alcohols induced α-helical structure in ADF, as revealed by the increase in MRE_{222nm} values. The fluoro alcohols tested showed a higher helix-inducing potential compared to 2-chloroethanol and alkanols. Their effectiveness followed the order: 1,1,1,3,3,3-hexafluoro-2-propanol > 2,2,2-trifluoroethanol > *tert*-butanol > 2-chloroethanol > 1-propanol > 2-propanol. Near-UV CD spectra showed disruption of the tertiary structure in presence of alcohols. Tryptophan fluorescence of ADF was affected differently in presence of these alcohols, showing quenching with fluoro alcohols and enhancement with 2-chloroethanol and alkanols in the order: *tert*-butanol > 2-propanol > 1-propanol > ethanol > methanol. The obtained results suggested that the effectiveness of the alcohols correlated well with the number of fluorine atoms, bulkiness and arrangement of different alkyl groups.

Keywords: ficin, acid-denatured state, alcohol-induced state, structural transition

INTRODUCTION

The study of different conformational states of a protein has received considerable attention in the field of protein folding. These states have been produced by changing pH, temperature and concentration of chemical denaturants [1–4]. Characterization of different intermediates between native and unfolded states of a protein is an important step to understand the mechanism of protein folding [5]. The molten globule state has been shown to be a common intermediate in the folding pathway of many proteins [1, 6, 7]. Acid-denatured states of several proteins have been characterized as the molten globule state [8, 9]. On the other hand, alcohols have been found to induce α-helical structures in proteins [10–12] and these alcohol-induced states might resemble some of the intermediates in the protein folding pathway [13]. Although the exact mechanism of alcohol-induced α-helix formation in proteins remains unclear, the effect is largely correlated to the decrease in the polarity of the solvent, thus weakening the hydrophobic interactions and enhancing the formation of local hydrogen bonds to induce α-helical structures [14]. Stabilization of several acid-denatured proteins by alcohols, especially fluoro alcohols, has been well documented [15–17]. In contrast to other alcohols, both 1,1,1,3,3,3-hexafluoro-2-propanol (HFIP) and 2,2,2-trifluoroethanol (TFE) have been found to possess a high helix-inducing potential in proteins [18–20]. Furthermore, HFIP has also been employed to investigate Alzheimer's amyloid peptides due to its ability to dissociate aggregates [21].

Ficin (E.C. 3.4.22.3), a proteolytic enzyme from the papain family, isolated from the latex of *Ficus* species, has a molecular mass of about 23,800 Da and possesses an essential cysteine residue at its active site [22, 23]. It is a commercial enzyme with several industrial applications such as meat tenderization, photography, chitosan depolymerisation, *etc.* [24]. Although the three-dimensional structure of ficin still remains to be investigated, a few papers have been published recently, showing the effect of pH and chemical denaturants, such as urea and guanidine hydrochloride (GdnHCl) on the conformational stability of ficin [8, 25, 26]. Members of the cysteine protease family

---

* To whom all correspondence should be sent:
E-mail: saadtayyab2004@yahoo.com

i.e. papain, ficin and stem bromelain share common structural characteristics by showing resistance towards urea during destabilization in presence of GdnHCl [13, 25–27]. Such conformational stability of cysteine proteases in presence of the strong chemical denaturant urea is unusual, compared to other globular proteins [28, 29] and requires further research on their structural stability in presence of other chemical denaturants. Although effect of alcohols on both stem bromelain and papain at low pH has been reported [12, 30, 31], data on alcohol–induced structural transition in the acid-denatured state of ficin is lacking. In a previous study, acid-denatured state of ficin has been shown to accumulate between pH 3.0 and pH 2.2, based on the minimum value of the mean residue ellipticity at 222 nm (MRE_{222nm}) in the acid-induced transition [8]. Therefore, we selected the acid-denatured ficin accumulated at pH 2.5 and studied the effect of eight different alcohols including halogen alcohols (halogenols) and alkyl alcohols (alkanols) on its structural transformation using different probes such as far- and near-UV circular dichroism (CD) as well as tryptophan (Trp) fluorescence.

EXPERIMENTAL

Materials

Ficin, from fig tree (*Ficus glabrata*) latex (2 × crystallized) saline suspension, ≥1.5 units/mg protein (Lot 030M7022) as well as different alcohols, whose structures are shown in Fig. 1, *i.e.* 1,1,1,3,3,3-hexafluoro-2-propanol (Lot SHBB0681V), 2,2,2-trifluoroethanol (Lot 1366086), *tert*-butanol (Lot 58396KK), 2-propanol (Lot 77596MK) and methanol (Lot 42296LJ-199) were purchased from Sigma-Aldrich Inc., USA. 2-Chloroethanol (Lot S6221545), 1-propanol (Lot K42188897) and ethanol (Lot K42113283) were obtained from Merck Chemicals, Germany. Commercial ficin was used in all experiments without further purification. All other chemicals used were of analytical grade purity.

Protein concentration

Ficin concentration was determined spectrophotometrically on a Shimadzu double beam spectrophotometer, model UV-2450, using a specific extinction coefficient of 21.0 $(g/100\ ml)^{-1}\ cm^{-1}$ at 280 nm [22].

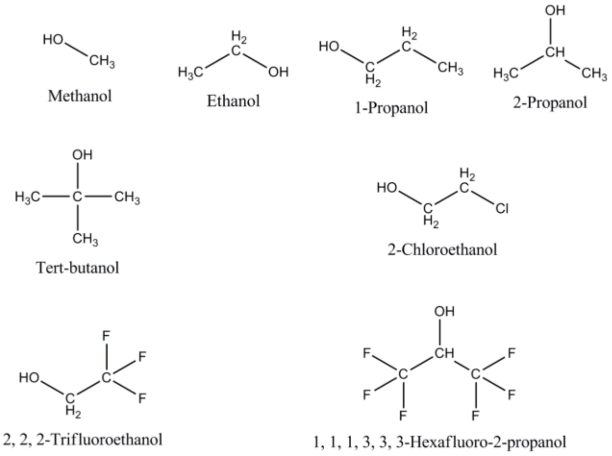

Fig.1. Structural formulae of various alcohols used in this study.

Circular dichroism spectroscopy

CD measurements were performed on a Jasco spectropolarimeter, model J-815, equipped with a thermostatically-controlled cell holder attached to a water bath, under constant nitrogen flow. The instrument was calibrated with (+)-10-camphorsulfonic acid and all measurements were made at 25°C using a scan speed of 100 nm/min and a response time of 1 sec. CD spectra in the far-UV and near-UV regions were recorded using protein concentrations and path lengths of 6.72 μM; 1 mm and 37.8 μM; 10 mm, respectively. The spectra were considered as an average of three scans. CD data were transformed into MRE values in $deg.cm^2.dmol^{-1}$ as described earlier [4]. The α-helical content was calculated from the MRE_{222nm} value following the method of Chen *et al.* [32] using the following equation:

$$\%\ Helix = (MRE_{222nm} - 2340 / 30300) \times 100$$

Fluorescence spectroscopy

Fluorescence measurements were carried out on a Jasco spectrofluorometer, model FP-6500, linked to a data recorder and equipped with a thermostatically-controlled cell holder, attached to a water bath to maintain constant temperature of 25ºC. The fluorescence spectra were recorded in the wavelength range 310–400 nm upon excitation at 295 nm using excitation and emission slits of 10 nm each and a protein concentration of 0.6 μM in a cell of 1 cm path length. Values of the fluorescence intensity obtained at different alcohol concentrations were transformed into relative fluorescence intensity by taking the value of the fluorescence intensity of acid-denatured ficin in the absence of alcohol as 100.

Preparation of acid-denatured and native forms

Acid-denatured form of ficin was prepared by dialyzing out the protein solution against 20 mM glycine-HCl buffer, pH 2.5 at 4 °C for 72 hours and was stored at 4 °C. Ficin solution was dialyzed against 20 mM sodium phosphate buffer, pH 7.0 under similar conditions for the preparation of the native form of the protein.

Conformational transitions

Alcohol-induced conformational transitions of ficin from acid-denatured state at pH 2.5 to alcohol-induced state were studied by taking increasing volumes (0.182–3.828 ml) of various alcohols in different tubes and adjusting the volume to 4.5 ml in each tube with 20 mM glycine-HCl buffer, pH 2.5. Then, a constant volume (0.5 ml) of a stock protein solution, prepared in the same buffer (67.2 μM and 6.0 μM for CD and fluorescence measurements, respectively) was added to each tube. The contents of each tube were mixed well and the mixture was incubated for 30 min at 25°C before CD/fluorescence measurements. Appropriate blanks were prepared by taking similar volumes of alcohols and making the total volume to 5.0 ml with 20 mM glycine-HCl buffer, pH 2.5. Far-UV CD spectral signal was used to monitor the secondary structural changes in the protein, whereas near-UV CD spectroscopy and Trp fluorescence were employed to study the tertiary structural changes. The contribution of the blank solution (containing buffer and alcohol) in both far- and near-UV CD spectral range was directly subtracted from the CD spectra of the test solutions. Rayleigh scattering measurements were made by measuring the emission spectra of various protein samples in the wavelength range 300-400 nm upon excitation at 350 nm. Lines in the transition curves were drawn as a guide for the eyes using the curve fitting mode of SIGMAPLOT software, version 11. The concentration of alcohol required to achieve 50% helix-induced transition (mid-point concentration) or C_m value was obtained from the transition curves at 50% of the helix-transition, whereas the m (dependence of ΔG_H on alcohol concentration) values were determined in the same way as described earlier [4].

RESULTS AND DISCUSSION

Far-UV CD spectra

Figure 2 shows the far-UV CD spectra of different conformational states of ficin obtained at pH 7.0 (native state) and at pH 2.5 both in the absence (acid-denatured state) and presence of 8 M TFE (alcohol-induced state).

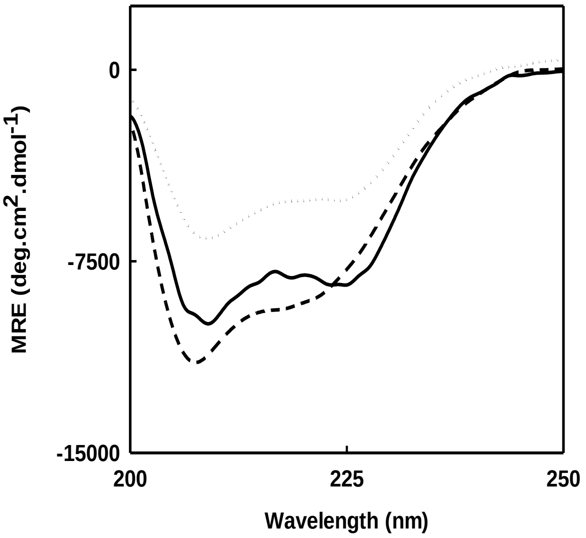

Fig. 2. Far-UV CD spectra of native ficin in 20 mM sodium phosphate buffer, pH 7.0 (──) and acid-denatured ficin in 20 mM glycine-HCl buffer, pH 2.5, both in absence (….) and presence (---) of 8 M TFE, obtained at 25°C using a protein concentration of 6.72 μM.

As can be seen from the figure, the CD spectrum of native ficin is characterized by the presence of two minima around 208 and 222 nm, which are indicative of the presence of α-helical structure in the protein [33]. Using the MRE_{222nm} value, the percentage helical content in the native state of ficin was calculated as ~20%. This value was similar to the one reported earlier [34]. Although acid-denatured ficin at pH 2.5 retained CD spectral characteristics, it showed a significant decrease in the MRE values in the whole wavelength range of CD spectra. About 39% decrease in MRE_{222nm} was observed in the acid-denatured state of ficin by taking MRE_{222nm} of native ficin as 100%. In an earlier report [8], about 30% decrease in MRE_{222nm} was shown at pH 2.5. Such a decrease in MRE_{222nm} value suggested a significant loss (11%) in the α-helical content while it was calculated to be 9% in the acid-denatured state. Presence of 8 M TFE in the incubation mixture of acid-denatured ficin (ADF) showed a marked increase in the MRE values, which were found even higher at certain wavelengths than MRE values of the native state. A comparison of MRE_{222nm}, obtained with ADF both in the absence and presence of 8 M TFE suggested 74% increase in MRE_{222nm} in presence of 8 M TFE, corresponding to 12% increase in the α-helical content. These results were in accordance with several earlier reports suggesting a strong helix-inducing potential of TFE [11, 15, 18, 19].

Alcohol-induced conformational transitions

Alcohols have been known to induce the formation of α-helical structure in proteins [15–18]. Alcohols with lower concentration required to produce 50% change in the structural transition are said to be more effective than others. Hence, the effectiveness of each alcohol differs from protein to protein and also varies among different alcohols [18–20]. In order to investigate the helix-inducing potential, as well as the effectiveness of various alcohols, *i.e.* fluoro alcohols (HFIP and TFE), chloro alcohol (2-chloroethanol) and both straight-chain and branched-chain alkanols (methanol, ethanol, 1-propanol, 2-propanol and *tert*-butanol), ADF was incubated at pH 2.5 with increasing concentrations of each of these alcohols for 30 min at 25°C and induction of α-helical structure was studied using far-UV CD spectra. Figure 3 shows TFE-induced structural changes in ADF at pH 2.5 as monitored by far-UV CD spectra within the concentration range 1.0-8.0 M. Presence of TFE at lower (≤ 2.0 M), as well as higher (≥ 7.0 M) concentrations produced minimal changes in the CD spectra, whereas a marked increase in the MRE values was observed within the TFE concentration range 3.0-6.0 M.

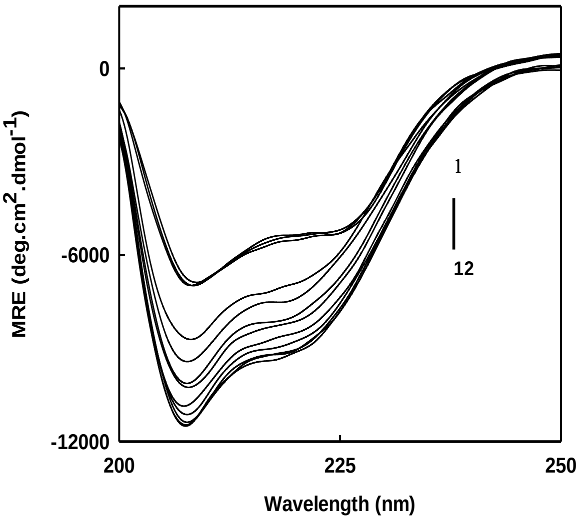

Fig. 3. Far-UV CD spectra of acid-denatured ficin in 20 mM glycine-HCl buffer, pH 2.5, obtained at 25°C using a protein concentration of 6.72 μM in absence and presence of increasing TFE concentrations (from top to bottom): 0, 1.0, 2.0, 3.0, 3.5, 4.0, 4.5, 5.0, 6.0, 7.0, 7.5, 8.0 M.

In other words, a threshold concentration of TFE (~2.0 M) was required to induce significant α-helical structure in ADF, as reflected by the increase in MRE_{222nm} value which reached a maximum value at 7.0 M TFE concentration and remained unaffected thereafter (Fig. 3). Such transition was suggestive of TFE-induced refolding of acid-denatured state into a TFE-induced state, which can be clearly seen from Fig. 4 where MRE_{222nm} values of ADF obtained at different TFE concentrations are plotted against alcohol concentration.

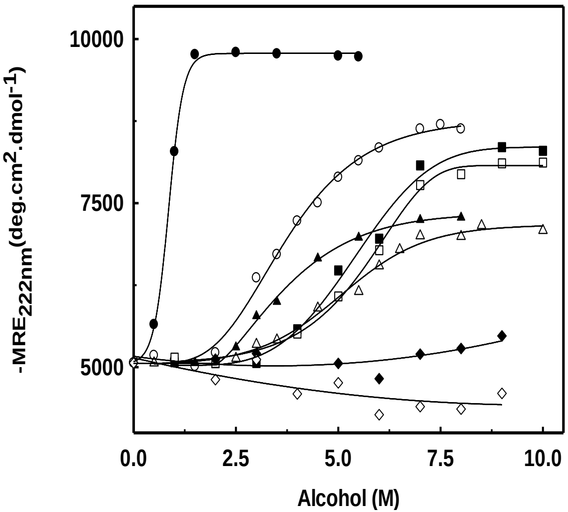

Fig. 4. Alcohol-induced structural transitions of acid-denatured ficin monitored by MRE_{222nm} at 25°C, using a protein concentration of 6.72 μM. Transitions obtained with various alcohols are shown with different symbols: HFIP (●), TFE (○), *tert*-butanol (▲), 2-propanol (Δ), 2-chloroethanol (■), 1-propanol (□), ethanol (♦), methanol (◊).

Similar structural transitions were studied with different alcohols by monitoring the MRE_{222nm} values of ADF at increasing concentrations of these alcohols and the results are shown in Fig. 4. The alcohol concentration range selected in this study was sufficient to achieve the completion of the transition in most of the cases. Out of the eight alcohols studied, two short chain alkanols (methanol and ethanol) were found ineffective in inducing significant α-helical structure in ADF. Methanol at higher concentration was found to slightly disrupt the α-helical structure present in ADF whereas a slight increase in MRE_{222nm} value was noticed at higher ethanol concentrations. Although the remaining six alcohols were found effective in inducing the α-helical structure in ADF, differences in both the extent of the α-helical structure induced (MRE_{222nm} values) at the highest alcohol concentration and the concentration of alcohol required to achieve the maximal α- helical structure (MRE_{222nm} values) were observed.

Table 1. Characteristics of alcohol-induced transition of acid-denatured ficin obtained by MRE_{222nm} measurements.*

Alcohol	*m* (cal/mol/M)	C_m (M)	Maximum MRE_{222nm} ($deg.cm^2.mol^{-1}$)	α-Helix (%)
		Alkanols		
1-Propanol	590	5.6	8117	19
2-Propanol	585	5.6	7156	16
tert-Butanol	612	3.6	7282	16
		Halogenols		
2-Chloroethanol	595	5.4	8353	20
2,2,2-Trifluoroethanol	636	3.5	8624	21
1,1,1,3,3,3-Hexafluoro-2-propanol	4085	0.8	9793	25

* Values of *m*, C_m and maximum MRE_{222nm} were obtained from Figure 4 as described in the Experimental section.

Both fluoro alcohols (HFIP and TFE) showed the strongest helix-inducing potential in ADF among all alcohols used in this study. More precisely, HFIP was found to be the strongest one as it required the lowest concentration to induce the maximal α-helical structure as reflected from the highest MRE_{222nm} value (Fig. 4). Quantitative analysis of the titration curves shown in Fig. 4 was made by determining the *m* and C_m values as described in the Experimental section and these values along with the maximum MRE_{222nm} values achieved at the highest alcohol concentration and % helix content are listed in Table 1.

As can be seen from both Fig. 4 and Table 1, HFIP had the highest m value (4085 cal/mol/M), as well as the lowest C_m value (0.8 M) among all alcohols studied, whereas 2-propanol was found least effective in inducing the α-helical structure, as reflected from the lowest m value (585 cal/mol/M) and highest C_m value (5.6 M), thus requiring the highest alcohol concentration to achieve the maximum MRE_{222nm} value. Although different alcohols seem to induce different states based on the MRE_{222nm} values achieved at their highest concentration, MRE_{222nm} was still maximum with HFIP and minimum with 2-propanol (Fig. 4 and Table 1).

In general, halogenols showed higher influence in inducing the α-helical structure in ADF compared to alkanols. Several earlier studies have also shown stronger helix-inducing potential of halogenols than alkanols [11, 15, 16, 18]. Among halogenols, both HFIP and TFE were found as the most effective α-helix inducers in ADF, correlating positively with the number of fluorine (F) atoms in the alcohol, *e.g.* HFIP being more effective than TFE. This was in agreement with earlier reports, suggesting higher helix-inducing potential of HFIP due to the presence of a bulky alkyl group and abundance of F atoms [11, 15]. Although the effectiveness of halogenols has been found to increase in the group, as chlorine substituted alcohols have been shown to be more effective α-helix inducers compared to fluorine substituted alcohols [15], the presence of multiple F atoms in fluoro alcohols (HFIP and TFE) has been found to surpass the difference in effectiveness due to the presence of Cl and F atoms in halogenols [11, 15]. This is illustrated by the greater effectiveness of HFIP containing 6 F atoms in inducing α-helix than TFE containing 3 F atoms (Fig. 4 and Table 1). Among alkanols, the helix-inducing potential varied with the number of methyl groups (bulkiness) in the alcohol, being more effective with *tert*-butanol compared to 1-propanol, though branching in 2-propanol slightly decreased its potentiality. Resuming, the effectiveness of different alcohols in inducing α-helical structure in ADF was found to follow the order: HFIP > TFE > *tert*-butanol > 2-chloroethanol > 1-propanol > 2-propanol. This order was in agreement with previous reports showing similar effectiveness of various alcohols in inducing α-helix in other proteins [15, 16]. In view of the above and regardless of the mechanism, the number of the halogen atoms in halogenols and the bulkiness of the alkyl group along with their structural arrangements in the alcohol are considered to be important factors in determining the effectiveness of these alcohols in inducing the α-helical structure [11, 18, 20].

Near-UV CD spectra

In order to study the effect of alcohol on the tertiary structure of ADF, near-UV CD spectra of native ficin and ADF both in absence and presence of 8.0 M TFE were recorded in the wavelength range 250-300 nm (Fig. 5). Near-UV CD spectroscopy is a useful approach to study the tertiary structural changes in proteins by monitoring the change in the environment of aromatic amino acids [35]. As can be seen from Fig. 5, two maxima

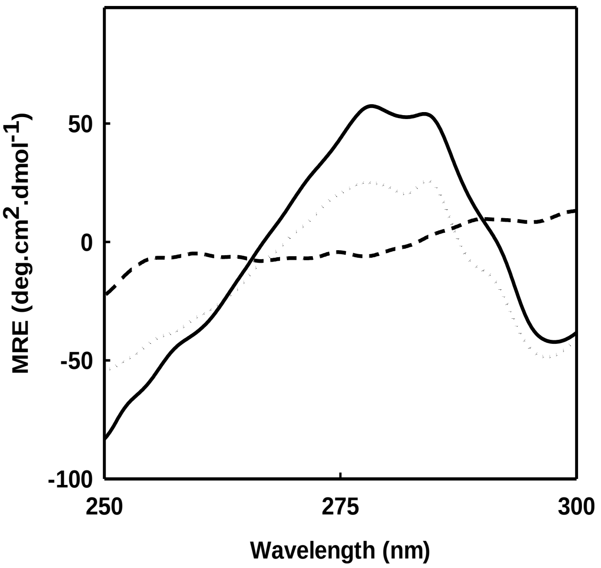

Fig. 5. Near-UV CD spectra of native ficin in 20 mM sodium phosphate buffer, pH 7.0(—) and acid-denatured ficin in 20 mM glycine-HCl buffer, pH 2.5, both in absence (…) and presence (---) of 8 M TFE, obtained at 25ºC using a protein concentration of 37.8 μM.

at 277 nm and 283 nm along with a minimum at 298 nm characterized the near-UV CD spectrum of the native enzyme. These features were similar to those described in an earlier report [8]. While these signals were retained in the near-UV CD spectrum of ADF, MRE values at both maxima were significantly reduced. Presence of 8 M TFE in the ADF solution resulted in a complete loss of these signals, suggesting disruption of the tertiary structure of the protein in this case. These results agreed well with previous reports showing loss in the protein tertiary structure in the presence of alcohols at higher concentrations [36, 37].

Fluorescence spectra

To validate the results obtained from near-UV CD spectra about the alcohol-induced tertiary structural changes in ficin at pH 2.5, Trp fluorescence spectra of native ficin and ADF both in absence and presence of 5.5 M *tert*-butanol were studied (Fig. 6). As evident from the figure, the fluorescence spectrum of native ficin is characterized by the presence of an emission maximum at 344 nm, which is blue shifted by 3 nm and is accompanied by a 26% decrease in the fluorescence intensity at pH 2.5. Devaraj *et al.* [8] also reported significant decrease in the fluorescence intensity along with a blue shift in the fluorescence spectrum of ficin at acidic pH. Decrease in the fluorescence intensity at the emission maximum was indicative of the change in the microenvironment around the Trp residues from nonpolar to polar, suggesting tertiary structural changes in the protein.

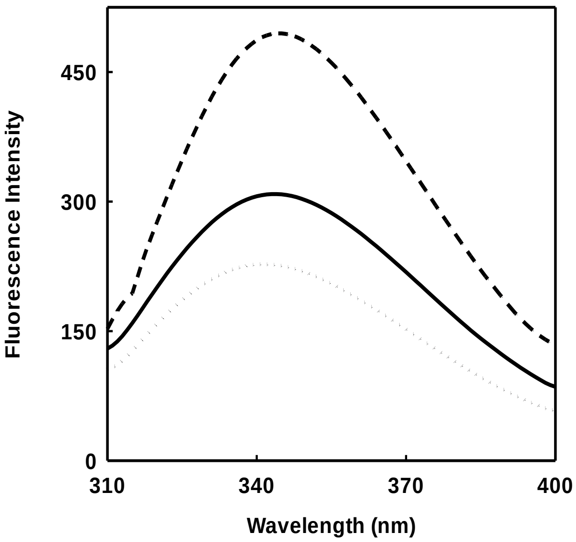

Fig. 6. Tryptophan fluorescence spectra of different conformational states of ficin obtained at 25ºC using a protein concentration of 0.6 μM upon excitation at 295 nm. Native state at pH 7.0 (—), acid-denatured state at pH 2.5 (…..) and acid-denatured state in the presence of 5.5 M tert-butanol (---).

These results supported our near-UV CD spectral data showing tertiary structural changes at pH 2.5. The possible reason for the small blue shift observed in the fluorescence spectrum of ficin at pH 2.5 stems from the heterogeneity of the fluorescence of multi-Trp residues [38] as ficin contains 6 Trp residues [22]. A marked increase in the fluorescence intensity along with normalization of the emission maximum (344 nm) was observed in the fluorescence spectrum of ficin at pH 2.5 in presence of 5.5 M *tert*-butanol. Such an increase in the fluorescence intensity indicated movement of Trp residues in the nonpolar environment. This seems probable, as these alcohols induced increased α-helical structure in ADF, as evident from Fig. 4. In the presence of increased helical structure in the alcohol-induced state of ficin, burial of Trp residues within and in between helical segments cannot be ruled out which might explain the increase in the fluorescence intensity. The increase in fluorescence intensity of ADF in presence of 5.5 M *tert*-butanol should not be taken as an indicator of reformation of the tertiary structure in the protein, as near-UV CD data had already confirmed disruption of the tertiary structure.

tert-Butanol-induced increase in the Trp fluorescence intensity of ficin at pH 2.5 prompted us to study the effect of various alcohols on the Trp fluorescence intensity of ADF. Titration results of ficin at pH 2.5 with increasing concentrations of different alcohols monitored by Trp fluorescence measurements at 341 nm are shown in Fig. 7.

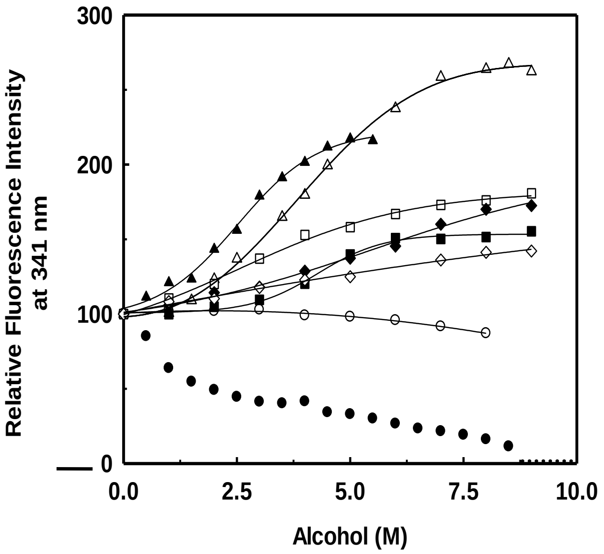

Fig. 7. Alcohol-induced structural transitions of acid-denatured ficin monitored by Trp fluorescence at 25ºC using a protein concentration of 0.6 µM upon excitation at 295 nm. Transitions obtained with various alcohols are shown with different symbols: HFIP (●), TFE (○), *tert*-butanol (▲), 2-propanol (Δ), 2-chloroethanol (■), 1-propanol (□), ethanol (♦), methanol (◊).

The possibility of aggregation in the presence of alcohol was ruled out based on the insignificant light scattering in these samples. Both fluoro alcohols (HFIP and TFE) showed anomalous behavior compared to that shown by other alcohols. For example, increasing concentrations of HFIP led to a significant quenching of Trp fluorescence in the initial range of alcohol concentrations, which sloped off at higher alcohol concentrations (Fig. 7). TFE also produced a decrease in the fluorescence intensity but it was much smaller than that obtained with HFIP and was observed only at higher alcohol concentrations. In an earlier study, specific quenching of Trp fluorescence intensity of cytochrome c was also observed in presence of HFIP [16]. Such quenching of Trp fluorescence can be ascribed to the energy transfer from Trp residues to other constituents of the protein. The decrease in the Trp fluorescence intensity of ficin at pH 2.5 in presence of lower HFIP concentrations reflected a compact denatured state, as has been shown in an earlier study with cytochrome c [16]. Contrary to it, all alkanols produced an increase in Trp fluorescence intensity with the increase in alcohol concentration. However, different alkanols showed different behavior in terms of the extent of increase in the fluorescence intensity and the concentration of alcohol required to achieve maximum fluorescence intensity for such alcohol. Of the six alkanols, both *tert*-butanol and 2-propanol were found more effective in bringing transition from acid-denatured state to an alcohol-induced state, compared to other alkanols. In general, the order of effectiveness among various alkanols was found to be: *tert*-butanol > 2-propanol > 1-propanol > ethanol > methanol. Similar order of effectiveness of various alkanols was observed in an earlier study on human serum albumin [18]. In view of these results, bulkiness of the alkyl group seems to be the main factor controlling the effectiveness of these alcohols.

As shown above, addition of both halogenols and alkanols induced α-helical structure in ADF, while with regard to disrupting the tertiary structure at higher concentrations, halogenols were more effective than alkanols. On the other hand, alkanols increased Trp fluorescence intensity while halogenols quenched it. Although many studies have shown the role of alcohols to increase the helical content of proteins, the mechanism by which alcohols induce the formation of α-helix has not been established yet [39]. A direct interaction of alcohol in micelle-like form [40] with the unfolded protein has been suggested to induce helical structure by decreasing the environmental polarity around the polypeptide chain, thus stabilizing the local hydrogen bonds [14]. The stronger ability of HFIP to form micelle-like HFIP clusters has also been proposed to explain the increase in its effectiveness in inducing helical structure. In view of these, the greater effectiveness of fluoro alcohols might be attributed to the bulkiness of the alkyl group, the presence of multiple F atoms and the formation of micelle-like clusters in an alcohol-water mixture. Although ficin showed unusual resistance towards urea denaturation [25, 26], it was found similar to other globular proteins in terms of its behavior towards alcohol-induced transition.

Both halogenols and alkanols (except ethanol and methanol) were found to induce an α-helical structure in ADF in the following order: HFIP > TFE > *tert*-butanol > 2-chloroethanol > 1-propanol > 2-propanol. However, the presence of these alcohols led to the disruption of the tertiary structure of ficin, as evident by the near UV CD spectra and Trp fluorescence. This behavior was similar to that observed with other globular proteins.

Acknowledgements: *This work was financially supported by the University of Malaya Research Grant (RG012/09AFR). The authors thank the Dean, Faculty of Science and the Head, Institute of Biological Sciences, University of Malaya for providing the necessary facilities to complete this work.*

REFERENCES

1 S. Dave, S. Mahajan, V. Chandra, H. K. Dkhar, Sambhavi, P. Gupta, *Arch. Biochem. Biophys.* **499**, 26 (2010).

2 S. Nakamura, Y. Seki, E. Katoh, S. Kidokoro, *Biochemistry* **50**, 3116 (2011).

3 T. Iida, S. Nishimura, M. Mochizuki, S. Uchiyama, T. Ohkubo, Y. Urade, A. Tanaka, T. Inui, *FEBS J.* **275**, 233 (2008).

4 S. Muzammil, Y. Kumar, S. Tayyab, *Proteins: Struct. Funct. Genet.* **40**, 29 (2000).

5 L. C. Wu, R. Grandori, J. Carey, *Protein Sci.* **3**, 369 (1994).

6 M. S. Zaroog, S. Tayyab, *Process Biochem.* **47**, 775 (2012).

7 S. Nakamura, T. Baba, S. Kidokoro, *Biophys. Chem.* **127**, 103 (2007).

8 K. B. Devaraj, P. R. Kumar, V. Prakash, *Int. J. Biol. Macromol.* **45**, 248 (2009).

9 S. Muzammil, Y. Kumar, S. Tayyab, *Eur. J. Biochem.* **266**, 26 (1999).

10 P. Sen, B. Ahmad, G. Rabbani, R. H. Khan, *Int. J. Biol. Macromol.* **46**, 250 (2010).

11 N. Hirota, K. Mizuno, Y. Goto, *Protein Sci.* **6**, 416 (1997).

12 S. Dave, H. K. Dkhar, M. P. Singh, G. Gupta, V. Chandra, S. Mahajan, P. Gupta, *Int. J. Biochem. Cell Biol.* **42**, 938 (2010).

13 S. Dave, S. Mahajan, V. Chandra, P. Gupta, *Int. J. Biol. Macromol.* **49**, 536 (2011).

14 P. D. Thomas, K. A. Dill, *Protein Sci.* **2**, 2050 (1993).

15 N. Hirota-Nakaoka, Y. Goto, *Bioorg. Med. Chem.* **7**, 67 (1999).

16 T. Konno, J. Iwashita, K. Nagayama, *Protein Sci.* **9**, 564 (2000).

17 Y. Luo, R. L. Baldwin, *J. Mol. Biol.* **279**, 49 (1998).

18 Y. Kumar, S. Tayyab, S. Muzammil, *Arch. Biochem. Biophys.* **426**, 3 (2004).

19 D. Hong, M. Hoshino, R. Kuboi, Y. Goto, *J. Am. Chem. Soc.* **121**, 8427 (1999).

20 N. Hirota, K. Mizuno, Y. Goto, *J. Mol. Biol.* **275**, 365 (1998).

21 S. J. Wood, B. Maleeff, T. Hart, R. Wetzel, *J. Mol. Biol.* **256**, 870 (1996).

22 I. E. Liener, B. Friedenson, *Methods Enzymol.* **19**, 261 (1970).

23 B. Friedenson, I. E. Liener, *Arch. Biochem. Biophys.* **149**, 169 (1972).

24 Z. Grzonka, F. Kasprzykowski, W. Wiczk, in: Industrial Enzymes: Structure, Function and Applications, J. Polaina, A. P. MacCabe, (eds.), Springer, Dordrecht, The Netherlands, 2007, p. 181.

25 N. A. A. Sidek, A. A. A. Halim, S. Tayyab, *Turk. J. Biochem.* **35**, 45 (2010).

26 K. B. Devaraj, P. R. Kumar, V. Prakash, *Process Biochem.* **46**, 458 (2011).

27 N.A.A. Sidek, Z. Alias, S. Tayyab, *Bulg. Chem. Commun.* **45**, 93 (2013).

28 P. Qu, H. Lu, X. Ding, Y. Tao, Z. Lu, *Spectrochim. Acta Part A* **74**, 1224 (2009).

29 L. Bian, T. Zhang, X. Yang, L. Liu, X. Zheng, *Chinese J. Chem.* **29**, 813 (2011).

30 S. K. Haq, S. Rasheedi, P. Sharma, B. Ahmad, R. H. Khan, *Int. J. Biochem. Cell Biol.* **37**, 361 (2005).

31 A. Naeem, K. A. Khan, R. H. Khan, *Arch. Biochem. Biophys.* **432**, 79 (2004).

32 Y-H. Chen, J. T. Yang, H. M. Martinez, *Biochemistry* **11**, 4120 (1972).

33 H. Chakraborty, B. R. Lentz, *Biochemistry* **51**, 1005 (2012).

34 China papers, available online at http://mt.china-papers.com/1/?p=161250 (2010)

35 D. E. Kamen, Y. Griko, R. W. Woody, *Biochemistry* **39**, 15932 (2000).

36 F. Khan, R. H. Khan, S. Muzammil, *Biochim. Biophys. Acta* **1481**, 229 (2000).

37 Y. O. Kamatari, T. Konno, M. Kataoka, K. Akasaka, *J. Mol. Biol.* **259**, 512 (1996).

38 M. R. Eftink, C. A. Ghiron, *Biochemistry* **15**, 672 (1976).

39 K. Yoshida, J. Kawaguchi, S. Lee, T. Yamaguchi, *Pure Appl. Chem.* **80**, 1337 (2008).

40 S. Kuprin, A. Graslund, A. Ehrenberg, M. H. J. Koch, *Biochem. Biophys. Res. Commun.* **217**, 1151 (1995).

СТРУКТУРНИТЕ ПРЕХОДИ В КИСЕЛИННО ДЕНАТУРИРАН ФИЦИН, ИНДУЦИРАНИ ОТ ХАЛОГЕНОЛИ И АЛКАНОЛИ

М. С. Заруг[1,2], Х. А. Кадир[1], С. Тайяб[1 *]

[1] Изследователска група "Биомолекули", Институт по биологични науки, Научен факултет, Малайски университет, 50603 Куала Лумпур, Малайзия

[2] Постоянен адрес:Факултет по приложни медицински науки, Университет в Гезира, П.К. 20, Уад Медани, Судан

Полученена на 27 март 2013 г.; ревизирана на 24 април 2014

(Резюме)

Изследван е ефекта на осем различни алкохоли, включително халогеноли и алканоли, върху структурната трансформация на киселинно-денатуриран фицин (ADF) при Н 2.5 с помощта на далечно и близко-вълнов UV кръгов дихроизъм (CD) и флуоресценция на триптофан. Освен метанола и етанола всички останали алкохоли индуцират α-спираловидна структура на ADF, което се вижда от повишаването на MRE_{222nm}- стойностите. Флуор-заместените алкохоли показват по-висок спирало-индуциращ потенциал в сравнение с 2-хлоретанола и алканолите. Тяхана ефективност е в реда: 1,1,1,3,3,3-хексафлуоро-2-пропанол > 2,2,2-трифлуороетанол > *tert*-бутанол > 2-хлоретанол > 1-пропанол > 2- пропанол. Близките UV CD - спектри показват разкъсване на третичната структура в присъствие на алкохоли. Триптофановата флуоресценция на ADF се влияе различно в присъствие на тези алкохоли, показвайки подтискане при флуоро-алкохолите и повишение при 2-хлоретанола и алканолите в реда: *tert*-бутанол > 2-пропанол > 1-пропанол > етанол > метанол. Получените резултати показват, че ефективността на алкохолите добре се корелира с броя на флуорните атоми, размера и разположението на различните алкилови групи.

Bulgarian Chemical Communications, Volume 46, Number 3(pp. 611– 615) 2014

Analytical solution of a transient Hartmann flow with Hall current and ion slip using finite Fourier transform

W. Abd El-Meged*, H. Attia and M. Elbarawy

Department of Engineering Mathematics and Physics, Faculty of Engineering, El-Fayoum University, El-Fayoum 63514, Egypt

Received August 8, 2013; Revised November 18, 2013

The transient Hartmann flow of an electrically conducting viscous incompressible fluid bound by two parallel insulating porous plates is studied using finite Fourier transform. An external uniform magnetic field is applied while the fluid motion is subjected to a constant pressure gradient. The Hall current and the ion slip are taken into consideration in the momentum equations. The effect of the Hall current and ion slip on the velocity and distribution of the flow is investigated.

Key words: Hartmann flow; Finite Fourier sine transform (FFST); Laplace transform (LT); conducting fluid; Hall current; Ion slip.

INTRODUCTION

The Hartmann flow defined as a magnetohydrodynamic (MHD) flow between two parallel plates is a classical issue that has many applications in MHD pumps, MHD power generators, accelerators, aerodynamics heating, and petroleum industry. In ref. [1] the influence of a transverse uniform magnetic field on the flow of a conducting fluid between two insulated infinite parallel stationary plates is studied. Then a lot of research work has been done concerning the Hartmann flow under different physical effects [2-11]. In most cases the Hall and ion slip terms were ignored in applying Ohm’s law as they have no marked effect for small and moderate values of the magnetic field. However, when an application of MHD requests a strong magnetic field, the influence of electromagnetic force becomes noticeable [4]. Under these conditions, the Hall current and ion slip are important as they will affect the magnitude and direction of the current density and consequently affect the magnetic force term. In ref. [6] the Hall effect on the steady motion of electrically conducting and viscous fluids in channels was studied. In [8-9] the effect on the steady MHD Couette flow with heat transfer was studied. The temperatures of the two plates were assumed either to be constant [8] or to vary linearly along the plates in the direction of the flow [9]. In [11] the effect of Hall current on the steady Hartmann flow subjected to a uniform suction and injection at the bounding plates was studied. Later, in [12] the problem of the unsteady state with heat transfer was extended taking into consideration the Hall effect while neglecting the ion slip. In [13] the ion slip was taken into consideration and the equations of motion were solved analytically using the Laplace transform (LT) method. The energy equation was solved numerically using the finite difference method taking into consideration the Joule and viscous dissipations.

In this paper, an analytical solution is presented for the transient flow of an incompressible, viscous, electrically conducting fluid between two infinite insulating horizontal plates with the consideration of both the Hall current and ion slip. The fluid is acted upon by a constant pressure gradient in the axial direction, while a uniform magnetic field is applied perpendicular to the plates. The induced magnetic field is neglected by assuming a very small magnetic Reynolds number. The momentum equations are solved analytically using Finite Fourier Sine transform (FFST). The effect of the magnetic field, the Hall current, and the ion slip on the velocity distribution is studied.

DESCRIPTION OF THE PROBLEM

The two insulating porous plates are located at $y = \pm h$ and extended from $x = 0$ to ∞ and from $z = 0$ to ∞ as shown in Fig.1.

The fluid flow between the two plates is influenced by a constant pressure gradient $\frac{dP}{dx}$ in

---

* To whom all correspondence should be sent:
E-mail: waleed.abdelmagied@invensys.com;

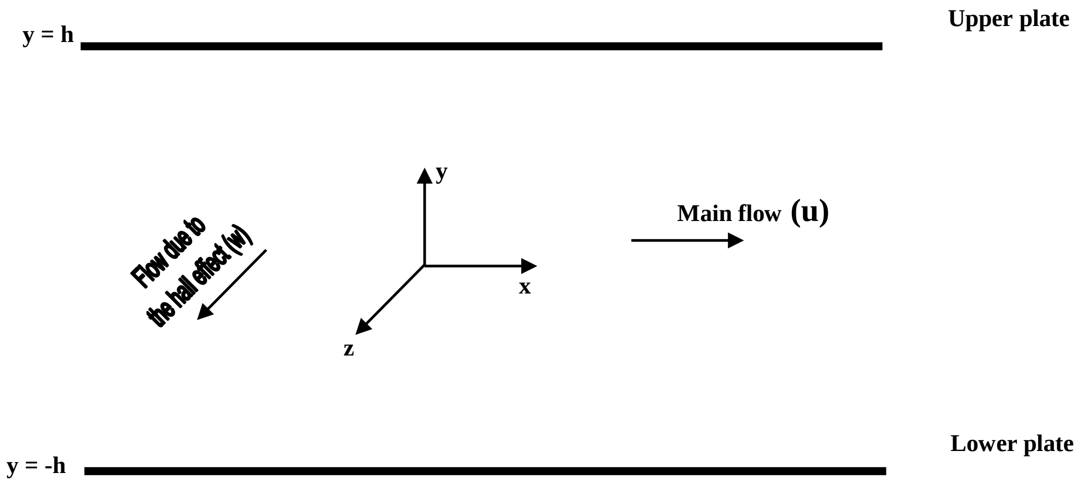

Fig. 1. Schematic diagram of the system.

the x-direction. The whole system is subject to a uniform magnetic field in the positive y-direction while the induced magnetic field is neglected. The existence of the Hall term gives rise to the z-component of the velocity. Thus the velocity vector of the fluid is given as:

$$\underline{v}(y,t)=u(y,t)\underline{i}+w(y,t)\underline{k} \qquad (1)$$

The fluid flow is governed by the momentum equation

$$\rho\frac{Dv}{Dt}=\mu\nabla^2 v-\nabla P+J\wedge B_o \qquad (2)$$

where ρ and μ are the density and the coefficient of viscosity of the fluid, respectively. If the Hall and ion slip terms are retained, the current density J is given by

$$J=\sigma\left\{v\wedge B_o-\beta(J\wedge B_o)+\frac{\beta B_i}{B_o}(J\wedge B_o)\wedge B_o\right\} \qquad (3)$$

where σ is the electric conductivity of the fluid, β is the Hall factor and B_i is the ion slip parameter [4]. Eqn. (3) may be solved in J to yield

$$J\wedge B_o=-\frac{\sigma B_o^2}{(1+\beta_i\beta_e)^2+\beta_e{}^2}\{((1+\beta_i\beta_e)u+\beta_e w)i+((1+\beta_i\beta_e)w-\beta_e u)k\} \qquad (4)$$

where $\beta_e=\sigma\,\beta\,B_o$ is the Hall parameter [4]. Thus, in terms of Eqns. (1) and (4), the two components of Eqn. (2) read

$$\rho\frac{\partial u}{\partial t}=-\frac{dP}{dx}+\mu\frac{\partial^2 u}{\partial y^2}-\frac{\sigma B_o^2}{(1+\beta_i\beta_e)^2+\beta_e{}^2}((1+\beta_i\beta_e)u+\beta_e w), \qquad (5)$$

$$\rho\frac{\partial w}{\partial t}=\mu\frac{\partial^2 w}{\partial y^2}-\frac{\sigma B_o^2}{(1+\beta_i\beta_e)^2+\beta_e{}^2}((1+\beta_i\beta_e)w-\beta_e u), \qquad (6)$$

The second and third terms on the right-hand side represent the viscous and Joule dissipations, respectively.

The problem is simplified by writing the equations in non-dimensional form. The characteristic length is taken to be h, and the characteristic time is $\frac{\rho h^2}{\mu^2}$ while the characteristic velocity is $\frac{\mu}{\rho h}$. We define the following non-dimensional quantities:

$$\hat{x}=\frac{x}{h},\hat{y}=\frac{y}{h},\hat{z}=\frac{z}{h},\hat{u}=\frac{\rho hu}{\mu},\hat{w}=\frac{\rho hw}{\mu},\hat{P}=\frac{P\rho h^2}{\mu^2},\hat{t}=\frac{t\mu}{\rho h^2},$$

In terms of the above non-dimensional variables and parameters, Eqns. (5)-(6) are written as (the "hats" will be dropped for convenience):

$$\frac{\partial u}{\partial t}=-\frac{dP}{dx}+\frac{\partial^2 u}{\partial y^2}-\frac{Ha^2}{(1+\beta_i\beta_e)^2+\beta_e^2}((1+\beta_i\beta_e)u+\beta_e w) \qquad (7)$$

$$\frac{\partial w}{\partial t}=\frac{\partial^2 w}{\partial y^2}-\frac{Ha^2}{(1+\beta_i\beta_e)^2+\beta_e^2}((1+\beta_i\beta_e)w-\beta_e u) \qquad (8)$$

where Ha is the Hartmann number subjected to the following initial and boundary conditions:

$$u=w=0\ ;\ t\le 0$$
$$u=w=0\ ;\ y=\pm 1 \qquad (9)$$

The main purpose of this paper is to solve the partial differential Eqns. (7), and (8) by FFST.

SOLUTION OF THE EQUATIONS OF MOTION USING FFST

The FFST of a function is defined as:

$$F_s\left(g(y,t)\right)=G_s(n,t)=\int_0^L g(y)\sin\left(\frac{n\pi y}{L}\right)dy\ ;\ 0\le \mathrm{y}\le \mathrm{L}\ ;\ \mathrm{n}=1,2,3,...... \tag{10}$$

where the kernel of the transform is:

$$\sin\ \left(\frac{n\pi y}{L}\right) \tag{11}$$

For transforming the second derivative we use the operational property

$$F_s\left(\frac{d^2g(y)}{dy^2}\right)=\frac{n\pi}{L}\left(\mathrm{g}(0)-\cos(n\pi)\mathrm{g(L)}\right)-\left(\frac{n\pi}{L}\right)^2G_s(n) \tag{12}$$

Thus, if the boundary value problem involves a second-order derivative, extends over a finite domain $0\le \mathrm{y}\le \mathrm{L}$, and has boundary conditions at both ends in the following form:

$$\begin{aligned}g(0,t)&=f_1(t)\\ g(L,t)&=f_2(t)\end{aligned}, \tag{13}$$

then FFST can be used to transform the 2nd-order derivative.

Defining:

$$v=u+iw \tag{14}$$

Eqns. (7) and (8) can be combined as:

$$\frac{\partial v}{\partial t}=-\frac{dP}{dx}+\frac{\partial^2 v}{\partial y^2}-\frac{Ha^2}{(1+\beta_i\beta_e)^2+\beta_e^2}(1+\beta_i\beta_e-i\beta_e)v \tag{15}$$

Applying FFST to Eqn. (15) yields

$$\frac{\partial V_s}{\partial t}+\left(\frac{n^2\pi^2}{4}+k\right)V_s=\frac{dP}{dx}*\frac{2}{n\pi}(\cos n\pi-1) \tag{16}$$

where

$$\mathrm{k}=\frac{Ha^2}{\left(1+\beta_i\beta_e\right)^2+\beta_e^2}\left(1+\beta_i\beta_e-i\beta_e\right) \tag{17}$$

The solution of the linear inhomogeneous partial differential Eqn. (16) under the initial and boundary conditions given in Eqn. (9) is given as

$$V_s(n,t)=\frac{\frac{dP}{dx}*\frac{2}{n\pi}(\cos n\pi-1)}{\left(\frac{n^2\pi^2}{4}+k\right)}\left(1-\mathrm{e}^{-\left(k+\frac{n^2\pi^2}{4}\right)t}\right) \tag{18}$$

The inverse transform of and their real and imaginary components are given by

$$v(y,t)=\sum_{n=1}^{\infty}\left(\frac{\frac{dP}{dx}*\frac{2}{n\pi}(\cos\ n\pi-1)}{\left(\frac{n^2\pi^2}{4}+k\right)}\left(1-\mathrm{e}^{-\left(k+\frac{n^2\pi^2}{4}\right)t}\right)\right)\sin\ \left(\frac{n\pi(y+1)}{2}\right) \tag{19}$$

$$u(y,t)=\mathrm{Re}\{v(y,t)\},\quad w(y,t)=\mathrm{Im}\{v(y,t)\} \tag{20}$$

Figs. 2(a) and 2(b) present the evolution of the profiles of the velocity components u and w versus y for $H_a=3$; $\beta_e=\beta_i=3$; $\frac{dP}{dx}=-5$, and for various values of time t (0.1; 0.5; 1.5; 3.0). The figures show the parabolic shape of the profiles and indicate that both u and w reach their steady state monotonously with time.

RESULTS AND DISCUSSION

As seen in Tables 1 and 2, the comparison between LT as used by Attia [13] and FFST methods for solving the equation of motion for Hartmann flow indicates that the outputs are nearly equal which lends confidence to the results obtained here.

Table 1. Comparison between LT and FFST for calculating u

Y	*t*=0.5		*t*=1.5		*t*=3	
	LT	FFST	LT	FFST	LT	FFST
-1	0	0	0	0	0	0
-0.8	0.5815	0.5811	0.6898	0.6898	0.6936	0.6936
-0.6	0.9968	0.9961	1.2029	1.2028	1.2101	1.2101
-0.4	1.2734	1.2724	1.5571	1.5569	1.567	1.567
-0.2	1.4312	1.43	1.7647	1.7646	1.7764	1.7763
0	1.4825	1.4812	1.8331	1.833	1.8454	1.8453
0.2	1.4312	1.43	1.7647	1.7646	1.7764	1.7763
0.4	1.2734	1.2724	1.5571	1.5569	1.567	1.567
0.6	0.9968	0.9961	1.2029	1.2028	1.2101	1.2101
0.8	0.5815	0.5811	0.6898	0.6898	0.6936	0.6936
1	0	0	0	0	0	0

Table 2. Comparison between LT and FFST for calculating w

Y	*t*=0.5		*t*=1.5		*t*=3	
	LT	FFST	LT	FFST	LT	FFST
-1	0	0	0	0	0	0
-0.8	0.0229	0.0229	0.0438	0.0437	0.0456	0.0456
-0.6	0.0429	0.0428	0.0824	0.0824	0.0859	0.0859
-0.4	0.0579	0.0578	0.1124	0.1124	0.1172	0.1172
-0.2	0.0673	0.0671	0.1313	0.1313	0.1369	0.1369
0	0.0704	0.0703	0.1378	0.1377	0.1436	0.1436
0.2	0.0673	0.0671	0.1313	0.1313	0.1369	0.1369
0.4	0.0579	0.0578	0.1124	0.1124	0.1172	0.1172
0.6	0.0429	0.0428	0.0824	0.0824	0.0859	0.0859
0.8	0.0229	0.0229	0.0438	0.0437	0.0456	0.0456
1	0	0	0	0	0	0

In Fig. 2, the velocity component u reaches the steady state faster than w.

Fig. 3 presents the time evaluation of u and w at y=0 for various values of the Hall parameter β_e , the ion slip parameter β_i at $Ha=1$.

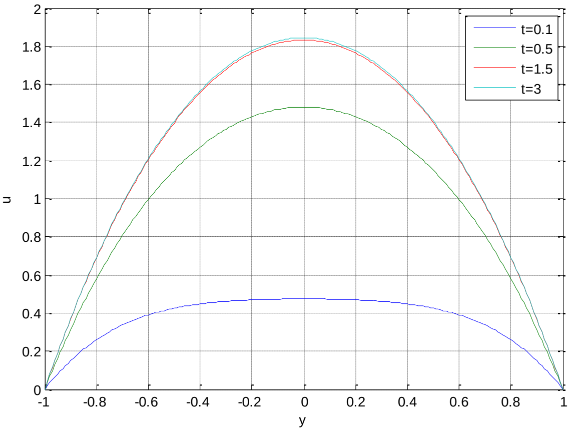

Fig. 2(a). Variation of u *versus* y.

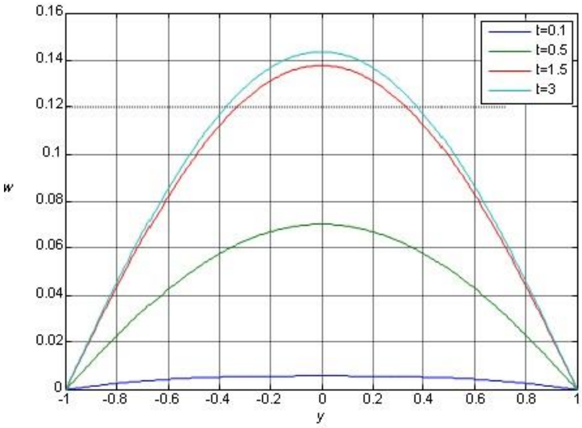

Fig. 2(b). Variation of w *versus* y.

In Fig. 3(a), increasing the parameters β_e and β_i will increase u because the effective conductivity $\frac{\sigma}{(1+\beta_i\beta_e)^2+\beta_e^{\,2}}$ decreases with increasing β_e or β_i which reduces the magnetic damping force on u.

In Fig. 3(b), increasing β_e will increase the velocity component w as a result of the Hall effect, but increasing β_i will decrease w for all values of β_e as a result of decreasing the source term of w ($\frac{\beta_e Ha^2 u}{(1+\beta_i\beta_e)^2+\beta_e^{\,2}}$) and increasing its damping term ($\frac{(1+\beta_i\beta_e)Ha^2 w}{(1+\beta_i\beta_e)^2+\beta_e^{\,2}}$), the influence of ion slip on w becoming clearer for higher values of β_e

In Fig. 3(b), increasing β_e will increase the velocity component w as a result of the Hall effect, but increasing β_i will decrease w for all values of β_e as a result of decreasing the source term of w ($\frac{\beta_e Ha^2 u}{(1+\beta_i\beta_e)^2+\beta_e^{\,2}}$) and increasing its damping term ($\frac{(1+\beta_i\beta_e)Ha^2 w}{(1+\beta_i\beta_e)^2+\beta_e^{\,2}}$), the influence of ion slip on w becoming clearer for higher values of β_e

For large β_e the components u and w overshoot, exceeding their steady state values and then go down towards steady state; the ion slip plays a role in suppressing these overshoots.

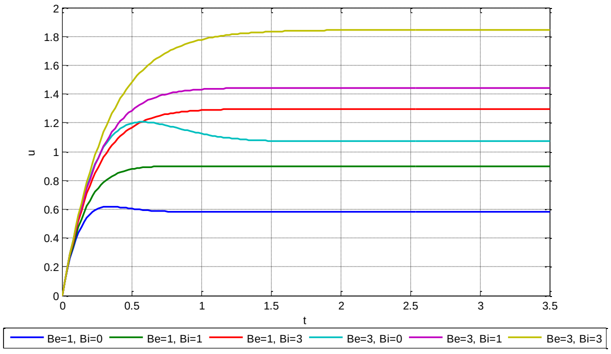

Fig. 3(a). Effect of Hall Parameter β_e and ion slip parameter β_i on the time development of u at y=0.

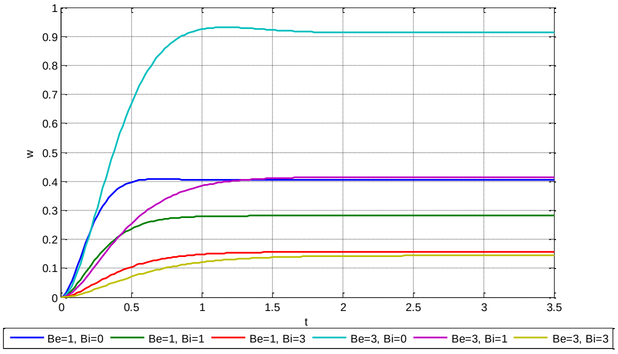

Fig. 3(b). Effect of Hall Parameter β_e and ion slip parameter β_i on the time development of w at y=0.

Fig. 4 presents u, and w at y=0 for various values of the Hartmann number Ha and the ion slip parameter β_i with $\beta_e = 3$.

As shown in Fig. 4(a), for small values of Ha, increasing β_i will slightly decrease u as a result of increasing the damping factor on u; further increasing β_i will increase the effective conductivity and, in turn, will decrease the damping factor on u which increases u; on the other hand, for larger values of Ha, u becomes small; increasing β_i always decrease the effective conductivity and consequently, will increase u, the effect of on u becoming more apparent for large values of Ha.

In Fig. 4(b), increasing the ion slip parameter β_i will decrease w for all values of Ha, its effect is more apparent for higher values of Ha.

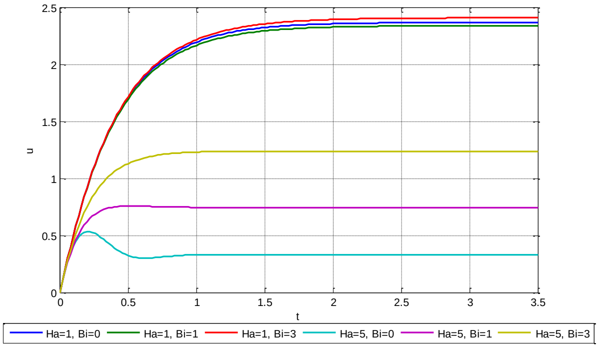

Fig. 4(a). Effect of Hartmann Number Ha and ion slip parameter β_i on the time development of u at y=0

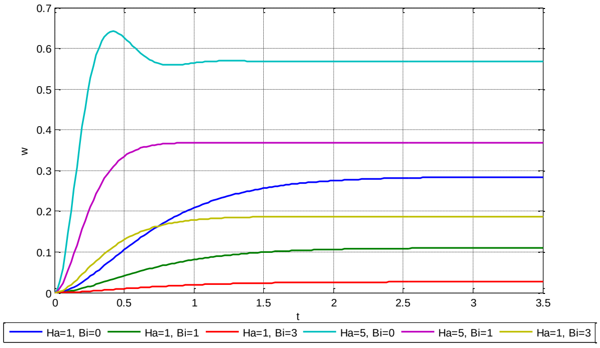

Fig. 4(b). Effect of Hartmann Number Ha and ion slip parameter β_i on the time development of w at Y=0.

CONCLUSIONS

FFST method can be used to obtain an analytical solution for the transient Hartmann flow of an electrically conducting, viscous, incompressible fluid bound by two parallel insulating plates with Hall current and ion slip. The comparison of the FFST method with previously used methods as LT shows that this technique is very simple and gives accurate results for solving the governing momentum equation for the whole range of the physical parameters used.

REFERENCES

1. J Hartmann and F Lazarus kgl. Danske Videnskab. Selskab Mat.-Fys. Medd. 15 (1937).
2. N Tao Journal of Aerospace Science 27 334 (1960).
3. S Nigam and S Singh The Quarterly Journal of Mechanics and Applied Mathematics 13 85 (1960).
4. K Cramer and S Pai (New York: McGraw-Hill) (1973).
5. G Sutton and A Sherman (New York: McGraw-Hill) (1965).
6. I Tani Journal of Aerospace Science 29 287 (1962).
7. H. A. Attia and M. A. M. Abdeen Effect of ion slip on the time-varying Hartmann flow of a non-Newtonian viscoelastic fluid with heat transfer, Journal of Applied Mechanics and Technical Physics 54 268 (March 2013)
8. V Soundalgekar, N Vighnesam and H Takhar IEEE Transactions on Plasma Science PS-7 178 (1979).
9. V Soundalgekar and A Uplekar IEEE Transactions on Plasma Science PS-14 579 (1986).
10. M. A. M. Abdeen, H. A. Attia, W. Abbas and W. Abd El-Meged Effectiveness of porosity on transient generalized Couette flow with Hall effect and variable properties under exponential decaying pressure gradient Indian Journal of Physics 87 767 (August 2013).
11. E Abo-El-Dahab Effect of Hall Currents on Some Magneto-hydrodynamic Flow Problems (Helwan University, Helwan: Master Thesis) (1993).
12. H Attia Canadian Journal of Physics 76 739 (1998).
13. H Attia Physica Scripta 66 470 (2002).

АНАЛИТИЧНО РЕШЕНИЕ НА ЗАДАЧАТА ЗА ПРЕХОДНО ТЕЧЕНИЕ НА HARTMANN С ТОК НА HALL И ЙОННО ПРИПЛЪЗВАНЕ СПОМОЩТА НА КРАЙНА ТРАНСФОРМАЦИЯ НА FOURIER

У. Абд Ел-Мегед*, Х. Атиа, М. Елбарауи

Департамент по физично и математично инженерство, Инженерен факултет, Университет в Ел-Фаюм, Ел-Фаюм 63514, Египет

Постъпила на 8 август, 2013 г.; коригирана на 18 ноември, 2013 г.

(Резюме)

Изследвано е преходното течение на Hartmann flow на електропроводящ несвиваем вискозен флуид между две успоредни изолаторни плочи с помощта на крайна Fourier'ова трансформация. Задачата е решена при прилагане на външно магнитно поле и постоянен градиент на хидравличното налягане. Токът на Hall и приплъзването на йони са отчетени в уравненията на движението. Установено е тяхното влияние върху скоростния профил в течността.

Bulgarian Chemical Communications, Volume 46, Number 3(pp. 616 – 623) 2014

Unsteady non-Darcian flow between two stationery parallel plates in a porous medium with heat transfer subject to uniform suction or injection

H. A. Attia[1], M. A. I. Essawy[2,*], A. H. Khater[3], A. A. Ramadan[3]

[1]*Department of Engineering Mathematics and Physics, Faculty of Engineering, Fayoum University, Egypt*
[2]*Higher Technological Institute (HTI), Giza, Egypt*
[3]*Mathematics Department, Faculty of Science, Beni-Suef University, Egypt*

Received July 29, 2013; Revised December 9, 2013

The unsteady non-Darcian flow in a porous medium of a viscous incompressible fluid bound by two stationery parallel porous plates is studied with heat transfer. A non-Darcy model that obeys the Forchheimer extension is assumed for the characteristics of the porous medium. A uniform and constant pressure gradient is applied in the axial direction whereas uniform suction and injection are applied in the direction normal to the plates. The two plates are kept at constant and different temperatures and the viscous dissipation is not ignored in the energy equation. The effects of porosity of the medium, inertial effects and uniform suction and injection velocity on both the velocity and temperature distributions are investigated.

Key words: Non-Darcian flow; parallel plates; Forchheimer equation; finite difference; numerical solution.

NOMENCLATURE:

x, y	Coordinates in horizontal and vertical directions, respectively
T_1, T_2	Temperature of lower and upper plates, respectively
dp/dx	Fluid pressure gradient
μ	Coefficient of viscosity
ρ	Density of the fluid
K	Darcy permeability of porous medium
β	Porosity parameter
λ	Inertial coefficient
$	Suction parameter
γ	Dimensionless non-Darcian parameter
c	Specific heat capacity of the fluid
k	Thermal conductivity of the fluid
T	Fluid temperature
u	Velocity component in the x-direction
v_o	Constant velocity component in the y-direction
Ec	Eckert number
Pr	Prandtl number
Re	Reynolds number
t	Time

INTRODUCTION

The flow of a viscous electrically conducting fluid between two parallel plates has important applications, e.g., in magnetohydrodynamic (MHD) power generators, MHD pumps, accelerators, aerodynamics heating, electrostatic precipitation, polymer technology, petroleum industry, purification of molten metals from non-metallic inclusions and fluid droplets-sprays [1]. The flow between parallel plates of a Newtonian fluid with heat transfer has been examined by many researchers in the hydrodynamic case [2, 3] considering constant physical properties. The extension of the problem to the MHD case has attracted the attention of many authors [4-8].

Fluid flow in porous media is now one of the most important topics due to its wide applications in both science and engineering [9, 10]. In most of the previous work, the Darcy model was adopted when studying porous flows. The Darcy law is sufficient in studying small rate flows where the Reynolds number is very small. For larger Reynolds numbers the Darcy law is insufficient and a variety of models have been implemented in

---

* To whom all correspondence should be sent:
E-mail: mohamed.essawy@hti.edu.eg

studying flows in porous media. The Darcy–Forchheimer (DF) model is probably the most popular modification to Darcian flows utilized in simulating inertial effects [11-14]. It has been used extensively in chemical engineering analysis and in materials processing simulations. On the other hand, we may indicate the existence of non-Darcian flows (of different kinds) for very low velocity in low-permeability media [15-17].

In this paper, the transient unsteady non-Darcian flow with heat transfer through a porous medium of an incompressible viscous fluid between two infinite horizontal stationery porous plates is investigated and the DF model is used for the characteristics of the porous medium. A constant pressure gradient is applied in the axial direction and uniform suction from above and injection from below is imposed in the direction normal to the plates. The two plates are maintained at two different but constant temperatures. The non-Darcian flow in the porous medium deals with the analysis in which the partial differential equations governing the fluid motion are based on the non-Darcy law (Darcy-Forchheimer flow model) that accounts for the drag exerted by the porous medium [18-20] in addition to the inertial effect [14, 21-26]. The viscous dissipation is taken into consideration in the energy equation. This configuration is a good approximation of some practical situations such as heat exchangers, flow meters, and pipes that connect system components. The cooling of these devices can be achieved by utilizing a porous surface through which a coolant, either a liquid or gas, is forced. Therefore, the results obtained here are important for the design of the wall and the cooling arrangements of these devices. The governing momentum and energy equations are solved numerically using finite difference approximations. The inclusion of the porosity effect, inertial effects as well as the velocity of suction or injection leads to some interesting effects on both the velocity and temperature distribution.

DESCRIPTION OF THE PROBLEM

The two parallel insulating horizontal plates are located at the y = ±h planes and extend from x = -∞ to ∞ and z = -∞ to ∞ embedded in a DF porous medium where a high Reynolds number is assumed [11-14]. The lower and upper plates are kept at the two constant temperatures T1 and T2, respectively, where T2 > T1 and a heat source is included, as shown in Fig (1). The fluid flows between the two plates in a porous medium where the non-Darcy law (Darcy-Forchheimer flow model) is assumed [14, 21-26]. The motion is driven by a constant pressure gradient dp/dx in the x-direction, with uniform suction from above and injection from below applied at t = 0 with velocity v_o in the positive y-direction. Due to the infinite dimensions in the x and z-directions, all quantities apart from the pressure gradient dp/dx which is assumed constant, are independent of the x and z-coordinates, thus the velocity vector of the fluid is given as

$$\vec{v}(y,t) = u(y,t)\,\vec{i} + v_o\,\vec{j}$$

with the initial and boundary conditions u = 0 at t ≤ 0, and u = 0 at y = ±h for t > 0. The temperature T(y,t) at any point in the fluid satisfies both the initial and boundary conditions T=T1 at t ≤ 0, T=T2 at y = +h, and T=T1 at y = -h for t > 0. The fluid flow is governed by the momentum equation [27]

$$\rho\frac{\partial u}{\partial t} + \rho v_o\frac{\partial u}{\partial y} = -\frac{dP}{dx} + \mu\frac{\partial^2 u}{\partial y^2} - \frac{\mu}{K}u - \frac{\rho\lambda}{K}u^2 \tag{1}$$

where ρ and μ are the density of the fluid and the coefficient of viscosity, respectively, K is the Darcy permeability of the porous medium [18-20] and λ is the inertial coefficient (i.e. the non-Darcian Forchheimer geometrical constant which is related to the geometry of the porous medium [14]). The last two terms in the right side of Eq. (1) represent the non-Darcy porosity forces. To find the temperature distribution inside the fluid we use the energy equation [28]

$$\rho c\frac{\partial T}{\partial t} + \rho c v_o\frac{\partial T}{\partial y} = k\frac{\partial^2 T}{\partial y^2} + \mu\left(\frac{\partial u}{\partial y}\right)^2 + \frac{\mu}{K}u^2 \tag{2}$$

where c and k are the specific heat capacity and the thermal conductivity of the fluid, respectively. The last two terms on the right side of Eq.(2) represent the viscous dissipation effect; the first term is the classical expression of the viscous dissipation for a clear fluid (K → ∞), while the second term is the viscous dissipation in the Darcy limit (K → 0) [29]. For a full discussion of modeling this form of viscous dissipation, see [30, 31].

Introducing the following non-dimensional quantities

$$\hat{x} = \frac{x}{h},\ \hat{y} = \frac{y}{h},\ \hat{z} = \frac{z}{h},\ \hat{u} = \frac{\rho h u}{\mu},\ \hat{P} = \frac{P\rho h^2}{\mu^2},\ \hat{t} = \frac{t\mu}{\rho h^2},\ \hat{T} = \frac{T-T_1}{T_2-T_1}$$

$\$ = \rho v_o h/\mu$ (the suction parameter), $\Pr = \mu c/k$ (the Prandtl number), $Ec = \mu^2/\rho^2 c h^2 (T_2 - T_1)$ (the Eckert number), $\beta = h^2/K$ (the porosity parameter), $\gamma = \lambda h / K$ (the dimensionless non-Darcy parameter).

Equations (1), (2) are written as: (the "hats" will be dropped for convenience)

$$\frac{\partial u}{\partial t} + \$ \frac{\partial u}{\partial y} = -\frac{dP}{dx} + \frac{\partial^2 u}{\partial y^2} - \beta u - \gamma u^2 \tag{3}$$

$$\frac{\partial T}{\partial t} + \$ \frac{\partial T}{\partial y} = \frac{1}{\Pr} \frac{\partial^2 T}{\partial y^2} + Ec \left(\frac{\partial u}{\partial y} \right)^2 + \beta \; Ec \; u^2 \tag{4}$$

The initial and boundary conditions for the velocity become

$$u = 0, \; t \le 0 \;\; \& \;\; u = 0, \; y = \pm 1, \; t > 0 \tag{5}$$

and the initial and boundary conditions for the temperature are given by

$$t \le 0 : T = 0 \;\; \& \;\; t > 0 \; : \; T = 1, \; y = +1 \;\; \& \; t > 0 : \; T = 0, \;\; y = -1. \tag{6}$$

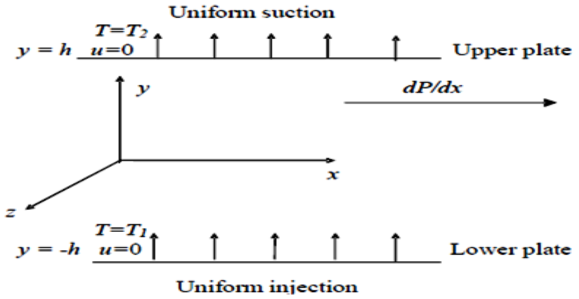

Fig. 1 The geometry of the problem

NUMERICAL SOLUTION OF THE GOVERNING EQUATIONS

Equations (3) and (4) are solved numerically using finite differences [32] under the initial and boundary conditions (5) and (6) to determine the velocity and temperature distributions for different values of the parameters *β*, *γ* and *$*. The Crank-Nicolson implicit method [33] is applied. The finite difference equations are written at the mid-point of the computational cell and the different terms are replaced by their second-order central difference approximations in the *y*-direction. The diffusion term is replaced by the average of the central differences at two successive time levels. Finally, the block tri-diagonal system is solved using Thomas algorithm. All calculations are carried out for $dP/dx = -5$, $Re = 1$, $Pr = 1$ and $Ec = 0.2$, while the results are obtained in a covering range for the non-Darcian parameter, $0.0 \le \gamma \le 2.0$ as [34]. It is found that the unsteady results reduce to those reported by Attia *et. al.* [35] for the cases of Newtonian fluid and Darcian model. These comparisons lend confidence in the accuracy and correctness of the solutions and, in turn, in the convergence of the two series defining the exact solution.

RESULTS AND DISCUSSION

Figures (2 – 4) show the time progression of the velocity profiles till the steady state for ($\$ = 1$) and various values of the porosity and non-Darcian parameters *β* and *γ*.
It is clear that the velocity charts are asymmetric about the $y = 0$ plane because of the suction. It is observed that the velocity component *u* increases monotonously with time. The porosity parameter *β* and the non-Darcian parameter *γ* have a marked effect on the time development of *u*. It is obvious that increasing *β* decreases *u* and its steady state time as a result of increasing the resistive porosity force on *u*, while increasing *γ* for each value of *β* decreases more the velocity *u* and its steady state time which reflects the expected resistance because of the inertial effects. For $\gamma = 0$ in figures (3-a) and (4-a) we mean a flow without additional inertial effects and the Darcian case is obtained to provide an easier quick path for the fluid flow. Fig (2-a) represents the simpler linear Newtonian case where the medium is non-porous with $\beta = \gamma = 0$ obtaining the highest velocity values.

Figures (5 – 7) show the time development of the temperature profiles for ($\$ = 1$) and various values of *β* and *γ*. It is observed that the temperature *T* increases monotonously with *t*. The parameters *β* and *γ* affect the time progression of the temperature *T*; increasing *γ* decreases *T* and its steady state time, as increasing *γ* decreases *u*, which, in turn, decreases the viscous dissipation which decreases *T*. Increasing *β* in the non-Darcian case ($\gamma \neq 0$) increases the temperature and decreases its steady state time because of the viscous dissipation in the Darcy limit. In figures (6 – a) and (7 – a) where ($\gamma = 0$) we obtain the linear Darcian case with higher temperature values for each *β*, while fig (5-a) shows the linear Newtonian case where the medium is non-porous ($\beta = \gamma = 0$) in which the highest temperature values are reached. It is observed that the velocity component *u* and the temperature *T* reach the steady state monotonously and that *u* reaches the steady state faster than *T*. This is expected, since *u* acts as the source of temperature.

Figures (8) and (9) indicate the effect of suction and injection on the time progression of both the velocity *u* and the temperature *T* at the center of the channel, respectively, for various values of *β* and *γ*.

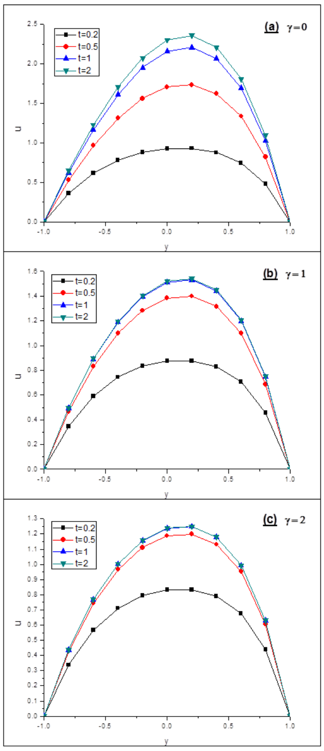

Fig. 2 Time development of the velocity u for $\beta = 0$, $\$ = 1$ and various values of

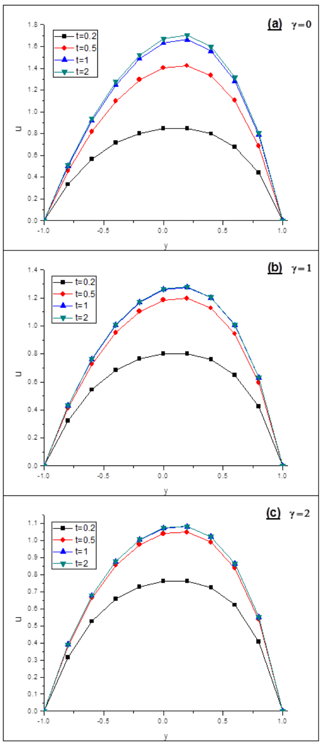

Fig. 3. Time development of the velocity u for $\beta = 1$, $\$ = 1$ and various values of

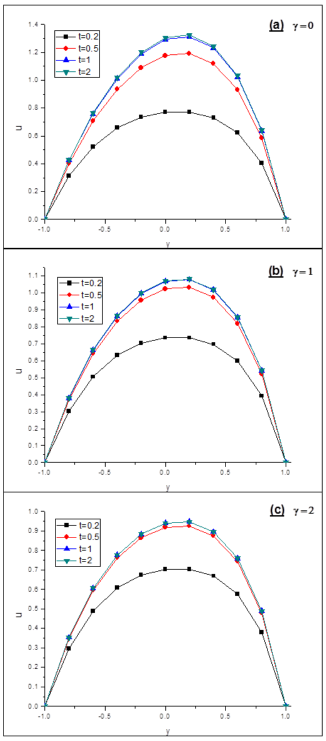

Fig. 4. Time development of the velocity u for $\beta = 2$, $\$ = 1$ and various values of γ

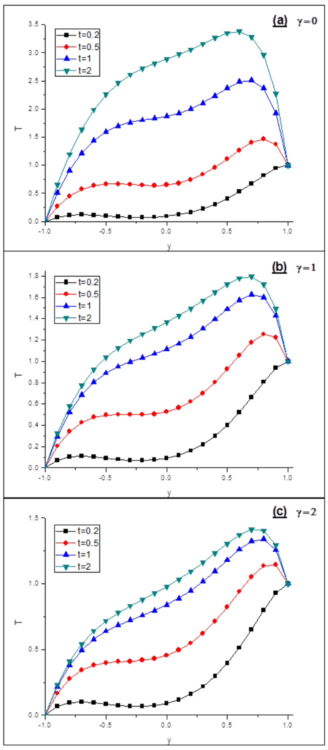

Fig. 5. Time development of the temperature T for $\beta = 0$, $\$ = 1$ and various values of γ

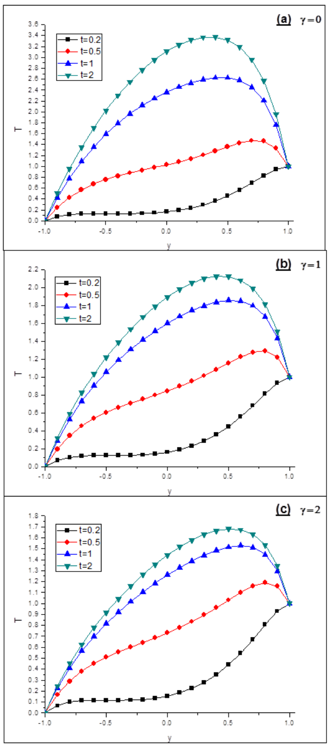

Fig. 6. Time development of the temperature T for $\beta = 1$, $\$ = 1$ and various values of γ

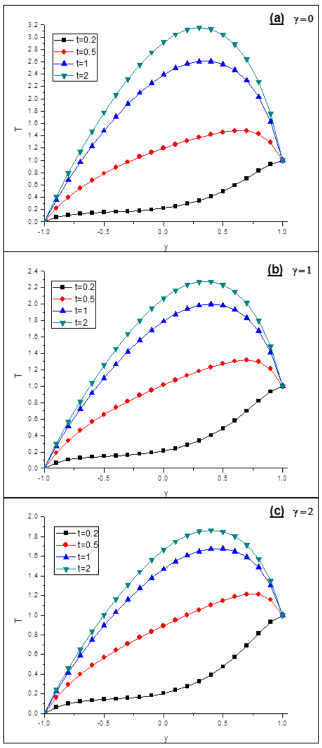

Fig. 7. Time development of the temperature T for $\beta = 2$, $\$ = 1$ and various values of γ

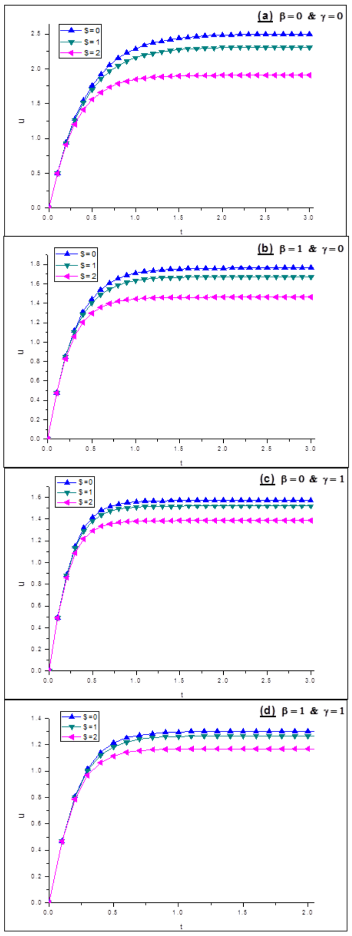

Fig. 8. Effect of the suction parameter *$* on the time development of the velocity *u* at the center of the channel (y = 0) for various values of the parameters β and γ

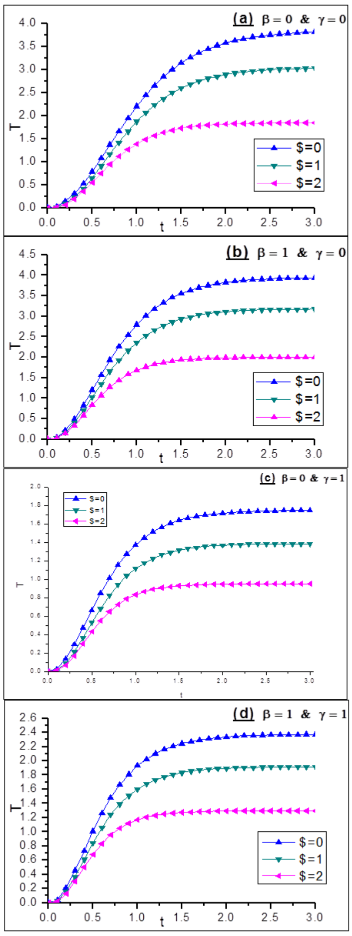

Fig. 9. Effect of the suction parameter *$* on the time development of the temperature *T* at the center of the channel (y = 0) for various values of the parameters β and γ

It is seen that increasing the suction parameter *$* decreases the velocity and its steady state time at the center of the channel due to the convection of the fluid from regions in the lower half to the center which has higher fluid speed. On the other hand, increasing the suction parameter *$* decreases the temperature *T* at the center of the channel which is influenced more by the convection term, which pushes the fluid from the cold lower half towards the center. Figures (8-a) and (9-a) indicate the linear Newtonian case where the plates are non-porous (β = 0) and there are no inertial effects (γ = 0) to obtain the highest velocity and temperature distributions. Figures (8-b) and (9-b) show the Darcian case in which the velocity decreases more because of the porosity of the medium (β = 1) and the temperature profile shows an increase due to the viscous dissipation caused by the porosity drag. Figures (8-c) and (9-c) show that the inertial effects (γ = 1) decrease more the velocity and temperature considering non-porous medium (β = 0). Also, figures (8-d) and (9-d) represent the non-Darcian flow in a porous medium ($\beta = \gamma = 1$) which shows an obvious resistive effect in decreasing *u* and *T* where a noticeable similarity in the velocity profiles for the different values of the suction parameter *$* is achieved. Also, it can be seen from Figure (9) that *T* may exceed the value 1 which is the temperature of the hot plate and this is due to the viscous dissipation.

Tables (1), (2) and (3) summarize the variation of the steady state values of both the velocity *u* and the temperature *T* at the center of the channel (y = 0), respectively, for various values of β and γ and different values of the suction parameter (*$* = 0, 1, 2). The results confirm the inverse proportionality between the parameters β and γ and the velocity *u* and the temperature *T* (considering the viscous dissipation for a clear fluid, $K \rightarrow \infty$) reaching the steady state of both because the increase in the porosity resistance and the inertial effects reduce *u* and hence *T*.

Table 1. Variation of the steady state velocity u at the center of the channel (y = 0) for various values of β, γ and $\$$.

(a) $\$ = 0$	γ = 0	γ = 1	γ = 2
β = 0	2.499986	1.570278	1.266707
β = 1	1.761786	1.301599	1.09713
β = 2	1.354654	1.097677	0.957878
(b) $\$ = 1$	γ = 0	γ = 1	γ = 2
β = 0	2.312212	1.518816	1.238231
β = 1	1.671946	1.264911	1.07488
β = 2	1.304083	1.071377	0.9405971
(c) $\$ = 2$	γ = 0	γ = 1	γ = 2
β = 0	1.907495	1.384467	1.16059
β = 1	1.460687	1.168418	1.014149
β = 2	1.178782	1.001486	0.893262

Table 2. Variation of the steady state temperature T at the center of the channel (y = 0) for various values of β, γ and $\$$ (considering the viscous dissipation for a clear fluid, K → ∞).

(a) $\$ = 0$	γ = 0	γ = 1	γ = 2
β = 0	3.84995	1.75015	1.2918
β = 1	2.115184	1.345975	1.087395
β = 2	1.430434	1.092352	0.9425454
(b) $\$ = 1$	γ = 0	γ = 1	γ = 2
β = 0	3.04365	1.386067	0.9881772
β = 1	1.665431	1.029702	0.8039784
β = 2	1.091862	0.8048577	0.673273
(c) $\$ = 2$	γ = 0	γ = 1	γ = 2
β = 0	1.844335	0.9489002	0.6783103
β = 1	1.078147	0.6951373	0.5387978
β = 2	0.7174322	0.5321741	0.4392434

Table 2. Variation of the steady state temperature T at the center of the channel (y = 0) for various values of β, γ and $\$$ (Considering the viscous dissipation in the Darcy limit, K → 0).

(d) $\$ = 0$	γ = 0	γ = 1	γ = 2
β = 0	3.84995	1.75015	1.2918
β = 1	3.951613	2.376075	1.831821
β = 2	3.632962	2.570357	2.084983
(e) $\$ = 1$	γ = 0	γ = 1	γ = 2
β = 0	3.04365	1.386067	0.9881772
β = 1	3.178412	1.917231	1.455387
β = 2	2.957291	2.08949	1.677764
(f) $\$ = 2$	γ = 0	γ = 1	γ = 2
β = 0	1.844335	0.9489002	0.6783103
β = 1	1.99993	1.296159	0.9982081
β = 2	1.931794	1.423236	1.15748

Furthermore, a direct proportionality between the porosity parameter β and the temperature T is obtained for $\gamma \neq 0$ (considering the viscous dissipation in the Darcy limit, $K \rightarrow 0$); which gives an obvious proof that the viscous dissipation in the Darcy limit considering the quadratic drag formulation depends on the porosity of the medium. The results also showed that increasing the suction parameter $\$$ decreases the velocity and the temperature and that higher velocity and temperature values for various β and γ are obtained at $\$ = 0$.

CONCLUSIONS

The unsteady non-Darcian flow through a porous medium between two stationery parallel plates of a viscous incompressible fluid was studied with heat transfer in the presence of uniform suction and injection considering different modes of viscous dissipation. The effects of porosity of the medium, inertial effects, suction and injection velocity on the velocity and temperature distributions are investigated. It is found that porosity, inertial effects and suction or injection velocity have a marked effect on decreasing the velocity distribution in an inverse proportionality manner. Furthermore, increasing the porosity parameter increases the temperature, while increasing the non-Darcian parameter decreases the temperature for each value of the porosity. Various cases were monitored passing through the Newtonian fluid flow in a non-porous medium, the Darcian flow model and the non-Darcian flow in a porous medium which showed the greatest flow resistance resulting in lower velocity and temperature values.

REFERENCES

1. J. Hartmann, F. Lazarus, Kgl. Danske Videnskab, Selskab, *Mat.-Fys. Medd.* **15**, 6 (1937).
2. A. Orhan, A. Mete, *Applied Energy*, **83**, 856 (2006).
3. B. Tudor, B. Ioana, *Appl. Math. Comp.*, **215**, 2673(2009).
4. R.A. Alpher, *Int. J. Heat and Mass Transfer*, **3**, 108 (1961).
5. S.D. Nigam, S.N. Singh, *Quart. J. Mech. Appl. Math.*, **13**, 85 (1960).
6. H.A. Attia, *African J. Math. Phys.*, **2**, 97 (2005).
7. H.A. Attia, *Kragujevac Journal of Science*, **31**, 11 (2009).
8. S. Erik, K. Vajravelu, A. Robert, G. Van, I. Pop, *Comm. Non. Sc. Num. Sim.*, **16**, 266 (2011).
9. A.E. Scheidegger, The physics of flow through porous media, University of Toronto, 1974.
10. M. Kaviany, Principles of heat transfer in porous media, Springer, 1995.
11. S.L. Lee, J.H. Yang, *Int. J. Heat Mass Transfer*, **40**, 3149 (1997).
12. Jr.J.S. Andrade, U.M.S. Costa, M.P. Almeida, H.A. Makse, H.E. Stanley, *Phys Rev Lett*, **82**, 5249 (1999).
13. N. Jeong, D.H. Choi, C.L. Lin, *J. Micromech. Microeng*, **16**, 2240 (2006).
14. F. Khani, A. Farmany, M. Ahmadzadeh Raji, F. Addul Aziz, Samadi, *Commun. Nonlinear Sci. Numer. Simulat.*, **14**, 3867 (2009).
15. C.E.Neuzil, *water resources research*, **22** (8), 1163, (1986).
16. Yao Yuedong and Ge Jiali, *Petroleum Science*, **8** (1), 55, (2011).
17. H.H. Liu and J. Birkholzer, *Journal of Hydrology*, **475**, 242, (2012).
18. D.D. Joseph, D.A. Nield, G. Papanicolaou, *Water Resources Research*, **18**, 1049 (1982).
19. D.B. Ingham, I. Pop, Transport phenomena in porous media, Pergamon, Oxford, 2002.
20. A.R.A. Khaled, K. Vafai, *Int. J. Heat Mass Transf.*, **46**, 4989 (2003).
21. O. Anwar Bég, Joaquín Zueco, H.S. Takhar, *International Communications in Heat and Mass Transfer*, **35**, 810 (2008).
22. Atul Kumar Singh, Pratibha Agnihotri, N.P. Singh, Ajay Kumar Singh, *International Journal of Heat and Mass Transfer*, **54**, 1111 (2011).
23. Yen-Cho Chen, *International Journal of Heat and Mass Transfer*, **47**, 1257 (2004).
24. Dulal Pal., *Commun. Nonlinear Sci. Numer. Simulat.*, **15**, 3974 (2010).
25. Ahmed A. Afify, *Applied Mathematical Modelling*, **31**, 1621 (2007).
26. Dulal Pal, Hiranmoy Mondal, *Commun. Nonlinear Sci. Numer. Simulat.*, **17**, 672 (2012).
27. H. Schlichting, Boundary layer theory, McGraw-Hill, New York, 1986.
28. S. Kakac, et al., Handbook of Single-Phase convective Heat Transfer , John Wiley, New York, 1987.
29. A.K. Al-Hadhrami, L. Elliott, D.B. Ingham, *Transp. Porous Media*, **49** (3), 265 (2002).
30. A. K. Al-Hadhrami, Fluid Flows Through Channels of Composite Materials, Ph D Thesis, University of Leeds, Leeds, 2001.
31. D. A. Nield, *Transport in Porous Media*, **41**, 349 (2000).
32. W.F. Ames, Numerical solutions of partial differential equations, 2nd ed., Academic Press, New York, 1977.
33. A.R. Mitchell, D.F. Griffiths, The Finite Difference Method in Partial Differential Equations , John Wiley, New York, 1980.
34. M. F. EL-Amin and N. A. Ebrahiem, *Transport in Porous Media*, **64**, 1 (2006).
35. H.A. Attia, M.A.M. Abdeen, and A.E. Abdin, *Journal of Engineering Physics and Thermophysics*, **86** (3), 677 (2013).

НЕСТАЦИОНЕРЕН НЕ-DARCIAN-ОВ ПОТОК МЕЖДУ ДВЕ СТАЦИОНАРНИ УСПОРЕДНИ ПЛОЧИ В ПОРЬОЗНА СРЕДА С ПРЕНОС НА ТОПЛИНА, ПРЕДМЕТ НА ПОСТОЯННО ВСМУКВАНЕ ИЛИ ИНЖЕКТИРАНЕ

Х.А. Атиа[1], М.А.И. Есави[2,*], А.Х. Хатер[3], А.А. Рамадан[3]

[1] *Департамент по физично и математично инженерство, Инженерен факултет, Университет в Ел-Фаюм, Ел-Фаюм 63514, Египет*
[2]*Висш технологичен институт (HTI), Гиза, Египет*
[3]*Департамент по математика, Научен факултет, Университет „Бени-Суеф“, Египетt*

Постъпила на 29 юли, 2013 г; коригирана на 9 декември, 2013 г

(Резюме)

Изучен беше нестационарен не-Darcian-ов поток в порьозна среда на един вискозен несвиваем флуид между две стационарни успоредни плочи с пренос на топлина. Един не-Дарси модел, който се подчинява на разширението на Forchheimer се приема за характеристиките на порестата среда. Еднакъв постоянен градиент на налягането се прилага в аксиална посока, докато еднакво всмукване и инжектиране се прилагат в посока перпендикулярна на плочите. Двете плочи се съхраняват при постоянни и различни температури и дисипацията на вискозитета не се пренебрегва в енергийното уравнението. Изследвани са ефектите на порьозност на средата, инерционните ефекти и постоянни скорости на всмукване и на инжектиране върху скоростния профил и разпределението на температурата са изследвани.

Bulgarian Chemical Communications, Volume 46, Number 3 (pp. 624 – 628) 2014

Preparation, characterization and photocatalytic activity of TiO_2/CoO nanocomposite

B. Khodadadi*[1], M. Sabeti [1], B. Nahri-Niknafs[2], S. Moradi-Dehaghi [3], P. Aberomand-Azar[4], S. Raeis-Farshid[5]

[1]*Department of Chemistry, Faculty of Science, University of Qom, Qom, Iran*
[2]*Department of Chemistry, Faculty of Science, Islamic Azad University, Karaj Branch, Karaj, Iran*
[3]*Department of Chemistry, Faculty of Science, Islamic Azad University, North Tehran Branch, Tehran, Iran*
[4]*Department of Chemistry, Faculty of Science, Islamic Azad University, Science and Research Branch, Tehran, Iran*
[5]*Department of Chemistry, Faculty of Science, Lahijan Branch Islamic Azad University, Lahijan, Iran*

Received July 18, 2013; Revised August 28, 2013

TiO_2/CoO nanocomposites were prepared by the sol-gel method with and without additives such as carboxymethyl cellulose (CMC), polyvinylpyrrolidone, (PVP), and hydroxypropyl cellulose (HPC). The structures and properties were characterized with FT-IR, XRD, SEM, and EDAX techniques. The photocatalytic activity under UV-irradiation to remove organic pollutants was investigated. The results revealed that additives have a significant effect on the particle size distribution and photocatalytic activity of TiO_2/CoO nanocomposites. SEM pictures showed that the particle size of TiO_2/CoO powder with additives was smaller than that of samples without any additive.

Keywords: Sol-Gel, TiO_2/CoO Nanocomposite, Photocatalytic activity

INTRODUCTION

In textile industry, the largest group of coloring materials is that of azo dyes [1–3]. These substances are some of the most important sources of environmental pollutants. In recent years, titanium oxide (TiO_2) is recognized as the most efficient semiconductor photocatalyst for environmental applications due to its potential application in removing of all types of organic pollutants [4–7].

The use of titanium oxide as a photocatalyst has the following advantages: strong oxidizing power, non-toxicity, high photochemical corrosive resistance and cost effectiveness. However, due to the wide band gap (3.2 eV) which requires the use of UV light, TiO_2 is active only under UV irradiation [7].

In order to improve the efficiency of photocatalytic activity and the response to visible irradiation, the catalyst can be modified using various additives. For example, metals or metallic oxides can be added into the TiO_2 structure by doping.

For the preparation of Co-doped TiO_2 nanocomposites several methods were reported, *e.g.,* solid-state method, impregnation method, and chemical coprecipitation method [7–9].

The sol-gel method has significant advantages, such as high purity, good uniformity of the powder microstructure, low-temperature synthesis, and easily controlled reaction conditions and therefore it has been used for the preparation of TiO_2/CoO nanocomposites [4, 7, 10–13].

In this study, Co-doped TiO_2 nanocomposites were prepared by the sol-gel method in presence of CMC, PVP, and HPC in order to investigate the effect of additives on the photocatalytic properties. The synthesized nanocomposites were characterized by Fourier transform infra-red spectroscopy (FT-IR), X-ray diffraction (XRD), scanning electron microscopy (SEM) and energy dispersive X-ray spectroscopy (EDAX). The influence of additives on the photocatalytic activity under UV-radiation was assessed in the decolorization of methyl orange in water using a batch reactor.

EXPERIMENTAL

Materials and Equipments

Titanium tetraisopropoxide (TTIP) (AR analytical grade, Merck Chemical Company) was the titanium source. Cobalt (II) nitrate.$5H_2O$, glacial acetic acid, di-ethanolamine (DEA), absolute ethanol, methyl orange, and deionized water were purchased from Merck Chemical Company and carboxymethyl cellulose (CMC), polyvinyl pyrrolidone (PVP), and hydroxypropyl cellulose (HPC) from Sigma-Aldrich Company. The characteristics of the nanocomposites were determined by the following methods. FT-IR

---

* To whom all correspondence should be sent:
E-mail: Khodadadi@qom.ac.ir

spectra of pellets were recorded in the range of 4000 to 500 cm^{-1} on a Shimadzu FT-IR spectrophotometer. XRD measurements for identifying the nanocomposites phases were performed on a Philips x'pert pro MPD diffractometer with CuK_α radiation from 10 to 80 (2θ) at room temperature. Morphology and microanalysis of the samples were studied by SEM (SEM-XL30, Philips). Ultraviolet-visible (UV-vis) absorption spectra were obtained on a Varian Carry 300 UV-vis spectrometer.

Preparation of Nanocomposites:

TiO_2/CoO nanocomposite powders were prepared using the sol-gel process according to the following procedure.

Preparation of TiO_2 sol: Yellow-colored TiO_2 sol was prepared at room temperature in 3 steps:

Step 1) solution I: TTIP was dissolved in absolute ethanol (at a molar ratio of 1: 9) under vigorous stirring for 10 min.

Step 2) solution II: Acetic acid and deionized water were added to absolute ethanol (at a molar ratio of 6: 1: 10).

Step 3) solution II was added slowly into solution **I** under vigorous stirring for 15 minutes to obtain a yellow transparent sol.

Preparation of CoO sol:

Step 1) solution I: $Co(NO_3)_2.5H_2O$ was dissolved in absolute ethanol (at a molar ratio of 0.1 : 110).

Step 2) solution II: di-ethanolamine and deionized water were added to absolute ethanol (at a molar ratio of 2: 1: 10).

Step 3) solution II was added dropwise into solution I under stirring for 15 minutes to obtain a transparent sol. Then, this sol aged for 72 h to allow it is formed as a gel. Ultimately, obtained gel was calcinated at 500 °C for 2 h.

Photocatalysis conditions:

The photocatalytic activity of the samples was studied on solutions of methyl orange (with a concentration of 5 mg L^{-1}) in deionized water as a pollutant. All experiments were carried out in a photoreactor system with a capacity of 1 liter, shown in Fig. 1.

Firstly, 0.2 g of photocatalyst powder was added into 1 L of pollutant solution and was let in dark for 24 h to eliminate the absorptive effect of the solution on the catalyst. Then it was placed in the photoreactor system which consisted of a cubic borosilicate glass reactor vessel, a cooling water jacket and a 15W UV lamp (Osram) as a light source placed in a quartz tube. The reaction temperature was kept at 25 °C using cooling water.

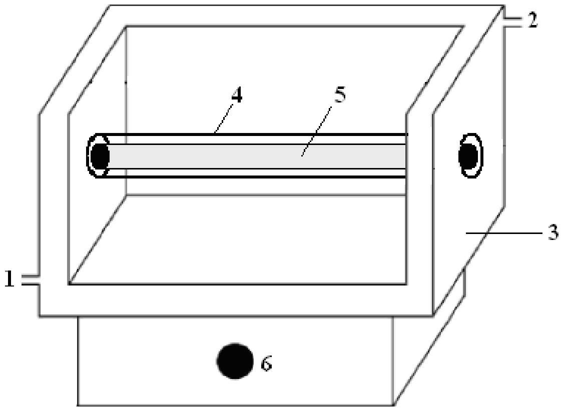

Fig. 1. Schematic diagram of the photoreactor system: 1-water inlet, 2-water outlet, 3-glass jacket, 4-quartz cover, 5-UV lamp, 6-stirrer

The changes in methyl orange concentration were monitored by an UV spectrometer.

RESULTS AND DISCUSSION

FT-IR spectroscopy:

The FT-IR spectra of the TiO_2/ CoO nanocomposite samples are presented in Fig. 2. The stretching vibration of the OH group and molecular H_2O leads to the appearance of the bands at about 3300–3550 cm^{-1} and 1620–1635 cm^{-1}, respectively. Hydrolysis of titanium tetraisopropoxide produced a large amount of propanol, which confirmed the presence of hydroxyl ions in the structure of the samples [13]. The peaks around 550 and 700 cm^{-1} can be attributed to symmetric stretching vibration of the Ti-O-Ti bond and O-Ti-O flexion vibration, respectively [14,15]. The peak at 1035 cm^{-1} may correspond to Ti-O-C bending [16].The interaction between the Ti-O network and the organic polymers (CMC, PVP or HPC) may cause Ti-O-C bonding. Moreover, the bands at 1117 cm^{-1} in the samples can be assigned to asymmetric stretching vibration of the Ti-O bands [17-19]. The peak at 602 cm^{-1} can be assigned to symmetric stretching vibration of the Ti-O-Ti group [18-20].

Furthermore, a band at 2366 cm^{-1} was observed which can be assigned to Co-TiO_2. The peaks at 400 and 1400 cm^{-1} were attributed to the vibration mode of Ti-O bond and those at 1240, 1160 and 1080 cm^{-1} should be due to the Ti-OH bond [21-23].

XRD analysis:

The crystalline structures of the samples were studied by X-ray diffraction analysis and the results are shown in Fig. 3.

In all samples, significant peaks were observed at 2θ=25, 48 which were related to anatase phase (the base peak in the range of $20<2\theta<30$ is an

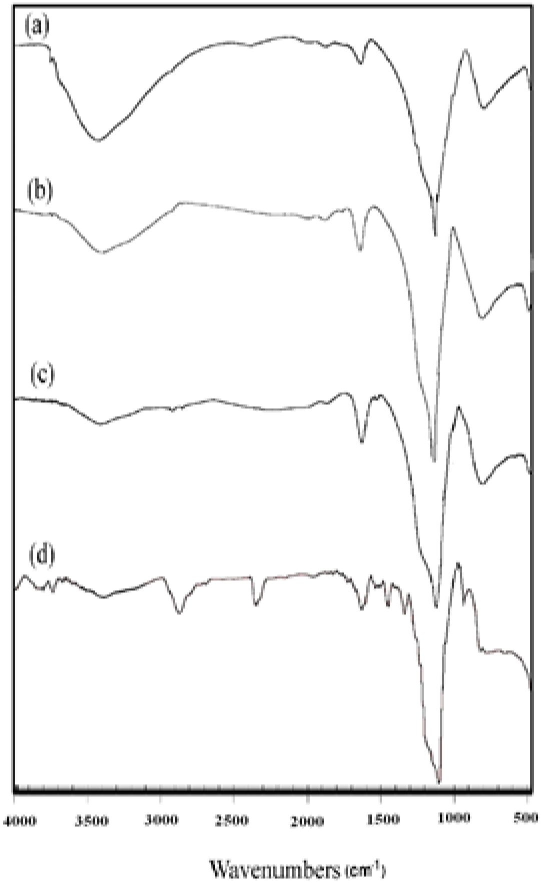

Fig. 2. FT-IR spectra of the sample sols. (a) sample 1, (b) sample 2, (c) sample 3, (d) sample 4

evidence of anatase phase); detectable peaks indexed as TiO_2 with rutile structure 2θ=27 were also observed but the anatase phase dominated. According to the XRD patterns, anatase structure was formed to a lesser extent in sample 1 than in the other samples. As can be seen, in the other samples containing additives, the anatase phase increased and for sample 4 containing HPC additive, the anatase phase peak is sharper than for other samples. This reveals that sample 4 is a very good option for its photocatalytic and self-cleaning ability.

SEM analysis:

Surface morphology of the synthesized nanocomposite powders was evaluated by SEM and the results are shown in Fig. 4. SEM pictures showed that nanoparticles in sample 1 (without additives), contains scattered particles which have different sizes and are agglomerated. Sample 2 with CMC is less agglomerated. The particle size of sample 3, containing PVP is smaller than that in the two previous samples and its distribution is more monotonous [5, 9, 11, 20]. Sample 4 containing HPC has the smallest particle size and the most uniform particle distribution with low agglomeration in comparison with the other samples [7, 8, 21].

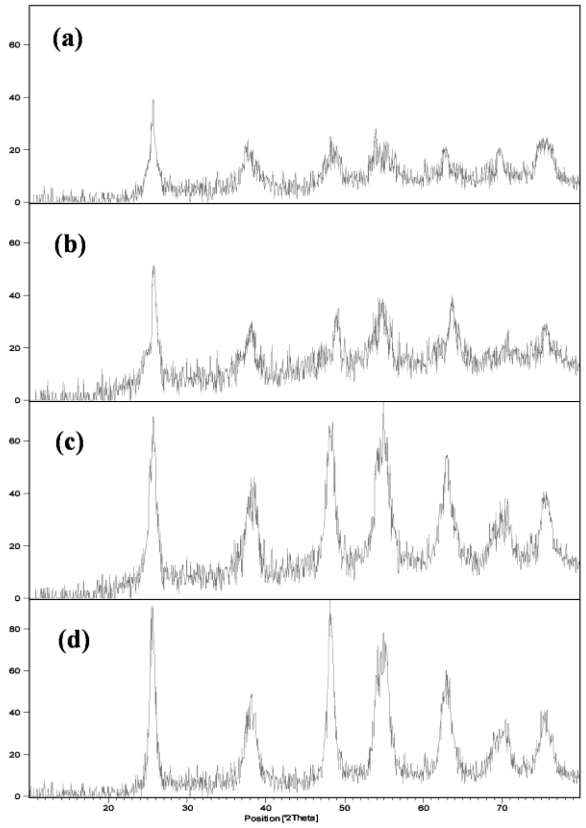

Fig. 3. XRD patterns of sol-gel synthesized Co-TiO_2.
(a) sample 1, (b) sample 2, (c) sample 3, (d) sample 4

EDAX analysis has revealed that TiO_2, SiO_2 and Co are present in all samples. All components and their weight percentages are shown in table 1.

Photocatalytic activity:

To evaluate the photocatalytic activity of the synthesized samples and to examine the role of additives, the solution of methyl orange (with a concentration of 5 ppm) in deionized water was selected as a pollutant solution for photodegradation. Fig. 5 shows the photocatalytic activity of the nanocomposites for decolorization of methyl orange as a function of time at λ = 465 nm. The photocatalytic activity of the sample was enhanced in the presence of additives [2]. Sample 4 containing HPC displayed the highest photocatalytic activity in comparison with the other samples. About 2.5 h after starting the reaction, the absorbance of the methyl orange solution reached 0. Hence, it may be concluded that the organic polymers act as a dispersing factor to avoid accumulation of the nanocomposite particles [23–25].

Table 1. Component and weight percentages of the samples according to EDAX analysis

Component	Wt%(sample1)	Wt%(sample2)	Wt%(sample3)	Wt%(sample4)
TiO_2	89.52	89.75	90.11	91.05
Co	10.48	10.25	9.89	9095
Total	10.00	10.00	100.00	100.00

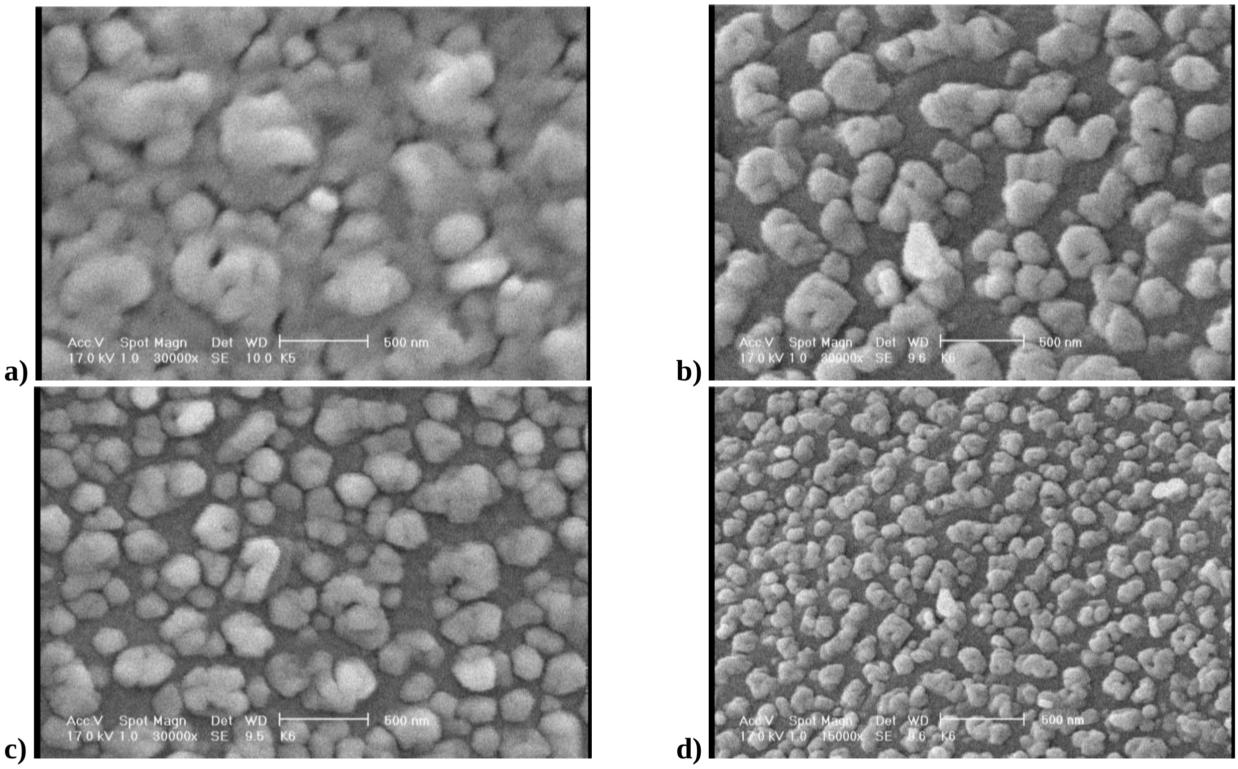

Fig. 4. SEM images of the samples: (a) sample 1, (b) sample 2, (c) sample 3, (d) sample 4

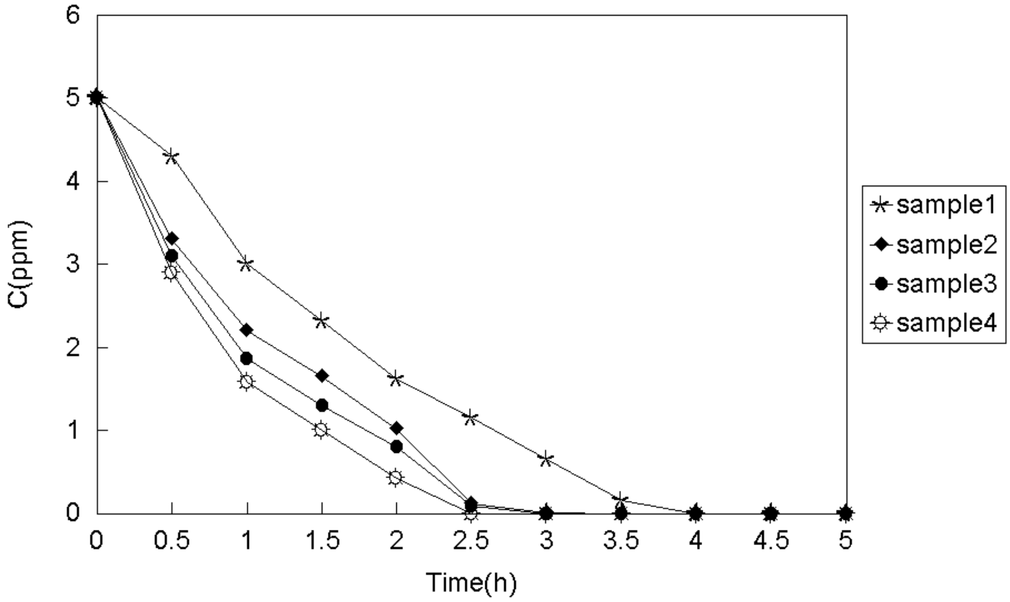

Fig. 5. Photodegradation rate of a methyl orange solution under UV radiation

CONCLUSIONS

This study confirmed that the photocatalytic activity of TiO_2/CoO nanocomposite powders can be improved using additives. Four samples of TiO_2/CoO nanocomposites were prepared by a sol–gel method. The photocatalytic activity of the synthesized nanocomposites, was investigated for degradation of methyl orange in water under UV-irradiation in a batch reactor. It follows from the XRD results that the anatase phase was the dominant phase in all samples and sample **4** showed the best photocatalytic activity. The SEM images indicated that in presence of HPC, both the density of the particles and their size distribution were improved. The results showed that the photocatalytic activity of the nanocomposites increased in presence of additives and HPC was more effective than others.

REFERENCES

1. S. Moradi; P. Aberoomand-Azar; S. Raeis-Farshid; S. Abedini-Khorrami and M. H. Givianrad, *J. Saudi Chem. Soc.*, in press (2012).
2. H. Yu; X. J. Li; S. J. Zheng and W. Xu, *Mater. Chem Phys*., **97**, 59 (2006).
3. P. Aberoomand Azar; S. Moradi Dehaghi; S. Samadi; S. Kamyar and M. Saber Tehrani, *Asian J. Chem.*, **22**, 1619 (2010).
4. J. Tian; L. Chen; J. Dai; X. Wang; Y. Yin and P. Wu, *Ceram. Int.*, **35**, 2261 (2009).
5. X. T. Wang; S. H. Zhong and X. F. Xiao, *J. Mol. Catal. A.*, **229**, 87 (2005).
6. M. H. Liao; C. H. Hsu and D. H. Chen, *J. Solid State Chem.*, **179**, 2020 (2006).
7. R. Khan and T. J. Kim, *J. Hazard. Mater.*, **163**, 1179 (2009).
8. D. L. Liao; C. A. Badour and B. Q. Liao, *J. Photochem. Photobiol. A*., **194**, 11 (2008).
9. J. Tian; L. Chen and Y. Yin, *Surf. Coat. Technol.*, **204**, 205 (2009).
10. K. Karthik; S. K. Pandian and N. V. Jaya, *Appl. Surf. Sci* , **256**, 6829 (2010).
11. J. Wang; J. Li and Y. Xie, *J. Environ. Manag.*, **91**, 677 (2010).
12. C. Chen; Z. Wang; S. Ruan; B. Zou; M. Zhao, F. Wu, *Dyes Pigments*, , **77**, 204 (2008).
13. Z. Zhang; Y. Yuan; Y. Fang; L. Liang; H. Ding and L. Jin, *Talanta*, **73**, 523 (2007).
14. B.A. Sava; A. Diaconu; M. Elisa; C.E.A. Grigorescu; C. Vasiliu and A. Manea, S*uperlattices Microst.*, **42**, 314 (2007).
15. K. Karthik; S. Kesava Pandian and N. Victor Jaya, *Appl. Surf. Sci.*, **256**, 6829 (2010).
16. B. Khodadadi; M. Sabeti; S. Moradi; P. Aberomand Azar and S. Raeis Farshid, *J. Appl. Chem. Res.*, **20**, 36 (2012).
17. K.M. Parida and N. Sahu, *J. Mol. Catal. Chem. A*, **287**, 151, 36 (2008).
18. H. Thoms; M. Epple; M. Froba; J. Wong and A. Reller, *J. Mater. Chem*., **8**, 1447 (1998).
19. M.P. Zheng; M. Gu; Y. Jin and G. Jin, *J. Mater. Sci. Eng. B*, **77**, 55 (2000).
20. M.P. Zheng; M.Y. Gu; Y.P. Jin; H.H. Wang; P.F. Zu; P. Tao and J.B. He, *J. Mater. Sci. Eng. B*., **87**, 197 (2001).
21. K.M. Parida and N. Sahu, *J. Mol. Catal. A: Chem.*, **287**, 151(2008).
22. J. Jiao; Q. Xu and L. Li, *J. Colloid Interface Sci.*, **316**, 596 (2007).
23. M. Houmard; D. Riassetto; F. Roussel; A. Bourgeois; G. Berthomé; J.C. Joud and M. Langlet, *J. Surf. Sci.*, **602**, 3364 (2008).

ПОЛУЧАВАНЕ, ОХАРАКТЕРИЗИРАНЕ И ФОТОКАТАЛИТИЧНА АКТИВНОСТ НА НАНОКОМПОЗИТИ ОТ TiO_2/CoO

Б. Ходадади *[1], М. Сабети[1], Б. Нахри-Никнафс[2], С. Муради-Дехаги [3], П. Абероманд-Азар[4], С. Раеис-Фаршид[5]

[1]*Департамент по химия, Научен факултет, Университет в Кум, Кум, Иран*
[2]*Департамент по химия, Научен факултет, Ислямски университет “Азад”, Клон Карадж, Иран*
[3] *Департамент по химия, Научен факултет, Ислямски университет “Азад”, Клон Северен Техеран, Техеран, Иран*
[4] *Департамент по химия, Научен факултет, Ислямски университет “Азад”, Клон за наука и изследвания, Техеран, Иран*
[5] *Департамент по химия, Научен факултет, Ислямски университет “Азад”, Клон Лахиджан, Лахиджан, Иран*

Постъпила на 18 юли, 2013 г.; коригирана на 28 август, 2013 г.

(Резюме)

Получени са нанокомпозити от TiO_2/CoO по метода зол-гел с и без добавки, като карбоксиметил-целулоза (CMC), поливинилпиролидон (PVP) и хидроксипропил-целулоза (HPC). Структурата и свойствата им са охарактеризирани с FT-IR, XRD, SEM и EDAX. Изследвана е фотокаталитичната активност за отстраняване на органични замърсители при облъчване с UV-лъчи. Резултатите показват, че добавките имат значителен ефект върху разпределението на частиците по размери и фотокаталитичната активност н нанокомпозитите. SEM-изображенията показват, че размерите на частиците в праховете от TiO_2/CoO с добавки са по-малки от тези в проби без добавки.

Bulgarian Chemical Communications, Volume 46, Number 3 (pp. 629 – 639) 2014

Peanut shells and talc powder for removal of hexavalent chromium from aqueous solutions

M. E. Ossman[1,2], M. S. Mansour[3], M. A. Fattah[1*], N. Taha[2], Y. Kiros[4]

[1]Petrochemical Engineering Department, Pharos University, PUA, Alexandria, Egypt
[2]Informatic Research Institute (IRI), City for Scientific Research and Technology Applications (CSRTA), Alexandria, Egypt
[3]Chemical Engineering Department, Alexandria University, Alexandria, Egypt
[4]KTH-Royal Institute of Technology, Department of Chemical Engineering & Technology, Stockholm, Sweden

Received August 19, 2013; Revised October 28, 2013

In this work, talc powder and peanut shells were investigated as potential adsorbents for the removal of hexavalent chromium from aqueous solutions. The effect of important parameters, such as contact time, solution pH and adsorbent dosage were also evaluated for the adsorption process of chromium (IV). The experimental data showed that a contact time of 30 min for peanut shells and 70 min for talc powder and pH of 4 were optimum for the adsorption to reach equilibrium. Furthermore, FT-IR, SEM and BET measurements were made in order to assess the physicochemical properties of the substrates. Langmuir, Freundlich, Temkin and Dubinin-Radushkevich isotherm models were used to fit the equilibrium data, heat and energy of adsorption of both adsorbents. Determinations of the rate of adsorption using kinetic models follow pseudo-first order for peanut shells and talc powder with intraparticle diffusion.

Keywords: Talc powder, peanut shell, hexavalent chromium, removal, wastewater.

INTRODUCTION

The presence of heavy metals in the environment has been of great concern due to the increased concentration of downstream discharge with toxic nature on various habitats affecting many living organisms. Toxicity levels of heavy metals depend on the type of metal, its valence state, its biological role and volume or concentration [1]. Chemical and biological properties of an element species depend very much on its oxidation state, and an accurate determination of different species of a given element is important for the comprehension of its biological and physiological functions, as well as potential toxicity [2]. The occurrence of heavy metals such as chromium derives either from anthropogenic or geogenic activities, in the former case it is mainly from chemical process industry emissions while in the latter it is through natural generation from rock-bearing materials. The transition metal chromium is found in aqueous streams such as wastewater, groundwater, seas and lakes released from different industrial sources and contaminants such as steel and other alloy forming materials and elements, electroplating, dyes and pigments for painting and printing, leather tanning, wood preservation and textiles, photography and surface treatment work as well as chromite from ultramafic rocks [3, 4].

Chromium usually exists in either hexavalent or trivalent form in aqueous media and is considered to be non-degradable. Hexavalent chromium is more toxic than the trivalent one owing to its high mobility across biological cell membrane and its oxidizing potential [5]. Hexavalent chromium is a mutagen, teratogen and carcinogen; chronic inhalation and exposure affect the respiratory tract with ulcerations of the body system and also affect the immune system [3, 6]. Therefore, differentiation and quantification of chromium in the two oxidation states are important in developing a strategic approach to deal with drainage of the wastewater and effluent disposal into the environment.

Various methods have been reported in the literature to remove hexavalent chromium such as reduction [7, 8], electro-coagulation [9], membrane and photocatalysis [10], co-precipitation [11], ion-exchange separation [12, 13] and adsorption, the latter being the most commonly employed method [14-17]. Traditional techniques using commercially available activated carbon for removal of the heavy metal chromium have been the preference of choice due to their accessible high surface area and porous structure leading to high adsorption capacity. However, high cost and dependence on importation of activated carbon by most developing countries would mean that alternatives that are on par with the surface characteristics and efficiency have to be sought for. Nowadays, low cost, environmentally benign and abundant resources are getting

---

* To whom all correspondence should be sent:
E-mail: Marwa.abdelfattah@pua.edu.eg

widespread attention for chromium effluent treatment, where agricultural waste and biomass products are converted into a value-added system as effective adsorbents. Owing to their chemical composition and complex structures of cellulose, hemicellulose and lignin, lignocellulosic materials can be used for adsorbing chromium-with slight or no modifications or treatment through physical and chemical means to have similar properties as activated carbons. Various lignocellulosic and agricultural wastes have been forwarded to maximize the adsorption capacity of Cr(VI) from wastewaters [17-24]. The potential for using complex minerals for the adsorption process of chromium (VI) has not been investigated except sand with major constituent of silica [25]. Talc mineral deposits exist in Egypt and its use as adsorbent material is for the first time presented. Therefore, the aim of this work was to study the possibility of using peanut shells and talc powder as adsorbents for removal of hexavalent chromium from waste water; to assess the important parameters that affect the adsorption process (such as time, pH, and dosage of adsorbents), as well as surface characteristics and properties of the adsorbents. Kinetic models and equilibrium studies were also carried out to substantiate the relationship with the experimental data for both adsorbents.

MATERIALS AND METHODS

Materials

$K_2Cr_2O_7$, sodium diphenylamine sulfonate, NaOH, and H_2SO_4 were all of analytical grade and were used as received. A stock solution of the adsorbate, hexavalent chromium of 10000 mg L^{-1} was prepared by dissolving an appropriate quantity of AR grade $K_2Cr_2O_7$ in 1000 ml of distilled water. The stock solution was further diluted to the desired concentration for obtaining the test solutions. Initial metal ion concentrations ranging from 70 to 3000 mg L^{-1} were prepared. A set of experiments was conducted to optimize and determine the Cr(VI) removal from aqueous solutions under varying process conditions of pH, contact time, amount of adsorbent and adsorbate concentration.

Characterization methods

The surface morphology of peanut shells and talc powder was analyzed using different magnifications by scanning electron microscopy (SEM, JEOL JSM 6360LA). The surface functional groups with binding sites and structure of the solid materials were studied by Fourier transform infrared spectroscopy (FTIR-8400S, Shimadzu). The FT-IR spectra of talc powder and peanut shells were recorded between 500 and 4000 cm^{-1}. The specific surface areas of peanut shell and talc powder were also characterized by the Brunauer-Emmet-Teller (BET) method, where the samples were degassed at120°C and nitrogen was adsorbed at liquid nitrogen temperature (-196 °C). Specific surface areas were calculated from the linear region of the isotherms in a relative P/Po pressure range of 0.06–0.20. Pore size distributions were derived from the adsorption branch of the isotherms by the Barrett–Joyner–Halenda (BJH) method. The total pore volumes were estimated from the amount adsorbed at a relative pressure of P/Po = 0.98.

Preparation of adsorbents and adsorption studies

Two adsorbents, one a biomass waste of peanut shells and another a mineral composite of talc powder, were used for Cr(VI) removal. The peanut shells were collected from local sources, washed with distilled water, cut into suitably sized pieces and dried in an oven at 80 ^{0}C for 2 h. The dried materials were then crushed and sieved into different sizes ranging from 4 mm to 500 μm. The talc powder was washed with distilled water and was subjected to sedimentation in order to remove any surface impurities. After this step, it was dried at 60°C in an oven for 1 h and then stored in a desiccator.

Batch adsorption experiments were conducted in 250 mL conical flasks at a solution pH of 4.0. The adsorbent, each in a different experiment, (0.5, 1, 2 and 3 g L^{-1}) was thoroughly mixed with 100 mL of hexavalent chromium solution (3000 mg L^{-1}) and the suspensions were stirred using IKA RT5 model magnetic stirrer operated at 400 rpm at room temperature. Duplicate samples of 1.0 mL each were collected from the supernatant at predetermined time intervals of 5 to 180 min to verify the reproducibility. These samples were then centrifuged for 5 min and the clear solutions were analyzed for the residual hexavalent chromium concentration. The spectrophotometric technique developed by Dong *et al*. [26] was used to determine the residual hexavalent chromium in the solution. This method is based on the reaction of hexavalent chromium with sodium diphenylamine sulfonate in an acidic medium to form a purple complex (λmax = 550 nm).

The amount of solute adsorbed per unit gram of adsorbent q (mg g^{-1}), was evaluated from the following equation:

$$q = \frac{(C_i - C_f)V}{M} \quad (1)$$

where: V is the volume of the solution, C_i is the initial concentration of the adsorbate solution (mg L^{-1}), C_f is the final concentration (mg L^{-1}) of the solute in the bulk phase at a time (*t*) and *M* is the mass of the adsorbent.

RESULTS AND DISCUSSION

Characterization of the adsorbents

Talc powder $Mg_3[Si_4O_{10}](OH)_2$ is a hydrous silicate material consisting of two major parts of oxides of silicon and magnesium with the chemical composition shown in Table 1.

Table 1. BET-surface area and chemical properties of the talc powder used.

Type	Value
Specific surface area (m^2/g)	4.3
SiO_2 (%)	63.26
MgO (%)	26.71
Al_2O_3 (%)	1.47
Fe_2O_3 (%)	0.54
CaO (%)	0.75
K_2O (%)	0.31
Na_2O (%)	0.13

It is one of the softest minerals ever known, having a hardness of 1 according to the Mohs scale. Its available surface area for adsorption or other wider area industrial application markedly depends on the particle size of the powder. Its specific surface area was found to be 4.3 m^2 g^{-1}. A schematic diagram of the chemical structure of talc powder is shown in Fig. 1. The particle size distribution for talc powder used was between 30 and 350 nm and the mean particle size was 158 nm with a pore volume corresponding to 0.09 cm^3 g^{-1}.

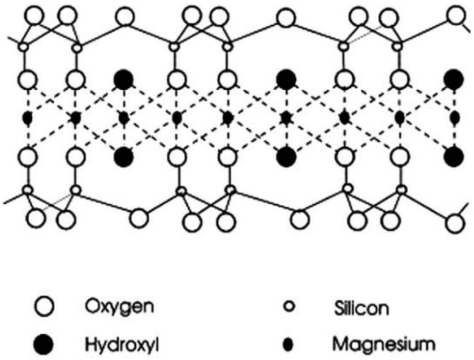

Fig. 1 Schematic diagram of the crystal structure of talc powder as viewed along the x-axis [27].

Peanut shells after the treatment steps had a specific surface area of 0.861 m^2 g^{-1}, a pore volume of 0.0036 cm^3 g^{-1} and an average particle diameter of 100 μm. Morphological analyses of the peanut shells and talc powder samples were performed by scanning electron microscopy (SEM) and are presented in Figs. 2a-2d for the respective adsorbent under different magnifications.

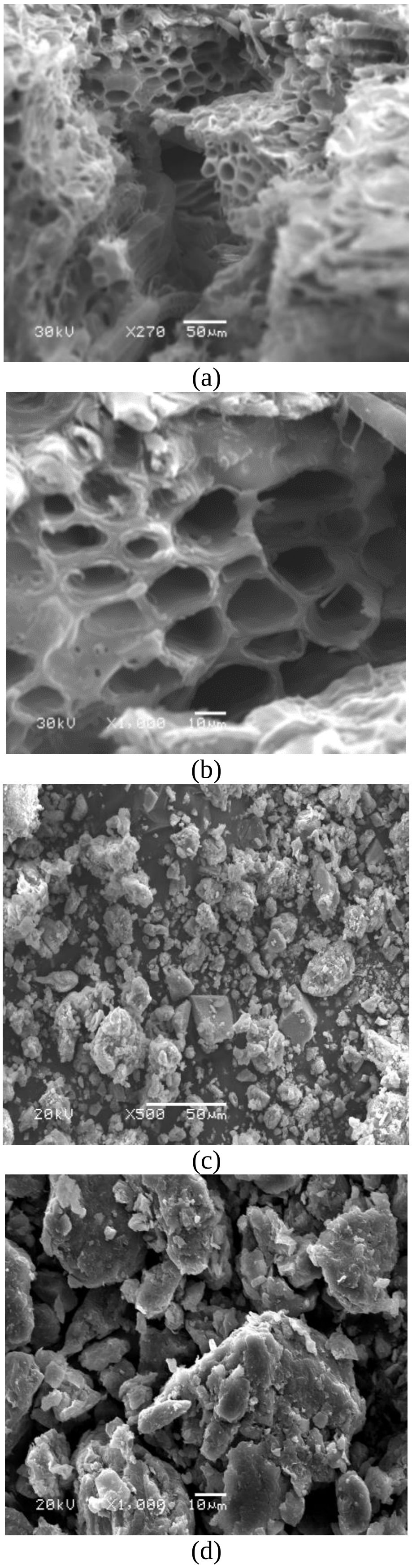

(a)

(b)

(c)

(d)

Fig. 2. a) SEM images for peanut shells with magnification of 270 times b) magnification of 1000 times c) SEM images for talc powder with magnification of 270 times d) magnification of 1000 times

At high magnification (Fig. 2b), peanut shells surface shows high roughness with hollow cavities of porous structures in the range of 7 to 25 µm, while Figs. 2c and 2d show talc powder having both small and big particle aggregates with sharp edges.

Like all vegetable biomass, peanut shells are composed of cellulose, hemicellulose and lignin. Peanut shells mainly consist of polysaccharides, proteins, and lipids, offering many functional groups such as carboxyl, carbonyl, hydroxyl and amino with characteristic chemical structures. The peaks in the FT-IR spectrum on Fig. 3 for peanut shells prior to adsorption were assigned to various groups and bands in accordance to their respective wave numbers (cm^{-1}) showing the complex nature of the adsorbent. The broad band around 3388 cm^{-1} is attributed to the surface hydroxyl groups (-OH), which are most probably due to the interaction and presence of alcoholic, phenolic, amino, and carboxylic derivatives. The peak at 2920 cm^{-1} is assigned to C–H asymmetrical stretching band of most aromatics, aliphatics and olefins [28]. These groups are also present in the lignin structure [29]. The peaks located at 2138 cm^{-1} are characteristic of the C−C stretching band, representing alkyne groups. The peak associated with the stretching in C=O (carbonyl compounds) and C=C is verified at 1629 cm^{-1} and is ascribed to ketones, aldehydes alkenes, esters and aromatic groups, respectively. The absorption peaks at 1480 and 1271 cm^{-1} could be due to C−O, C−H or C−C stretching vibrations. The peak observed at 1051 cm^{-1} is due to the C−O group in carboxylic and alcoholic groups. The band of the C−O group in Fig. 3 was more intense than that of the C=O group, possibly due to the presence of more C−O groups in peanut shells. The peak at 588 cm^{-1} is due to the vibrational bending in the aromatic compounds of lignin.

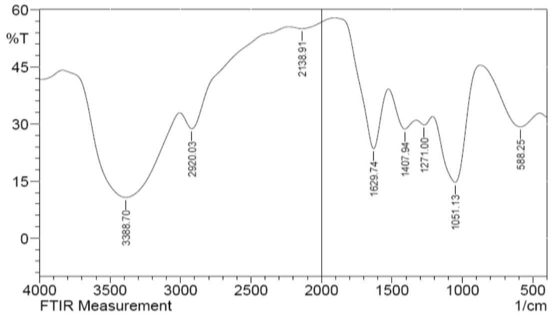

Fig. 3. FT-IR spectrum of raw peanut shells.

The vibrations in the bands of the FT-IR spectrum for talc powder are shown in Fig. 4, where wave numbers of 3676, 3441, 1040, 677 and 476 cm^{-1} dominate. The siloxane group (Si-O-Si) stretching vibrational bands exist with intense peaks at 476 and 1040 cm^{-1}, respectively, while the band at 677 cm^{-1} reflects the Si-O-Mg bond [30]. The bands at 3441 and 3676 cm^{-1} are ascribed to the vibrations of hydroxyl groups linked to Si (Si-OH) and Mg (Mg-OH), respectively [31].

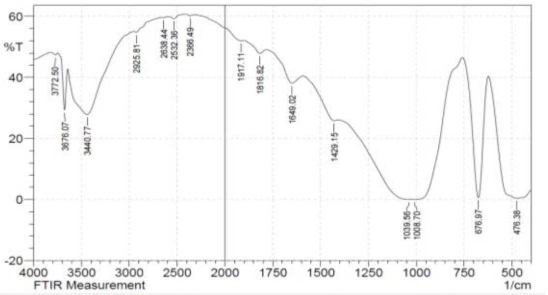

Fig. 4. FTIR spectrum of talc powder

Effect of contact time

Contact time has a strong effect on the adsorption process of chromium as the interaction depends on the physicochemical properties and volume of the adsorbent, as well as the distribution and flow rate in the adsorption column. Thus, higher flow rates and small volumes would mean less contact time with low adsorption capacity, while *vice versa* is valid for higher adsorption capacity. The effect of adsorption time on hexavalent chromium removal with comparative data for both adsorbents (0.5 g) is shown in Fig. 5. The amount of adsorbed hexavalent chromium increased with contact time for the two adsorbents used and equilibrium was attained within 30 min for peanut shells and 70 min for talc powder. The latter showed higher adsorption capacity for hexavalent chromium than peanut shells, because of its smaller average particle diameter, higher pore volume, higher surface area and the probable complexation with the compounds present in the mineral.

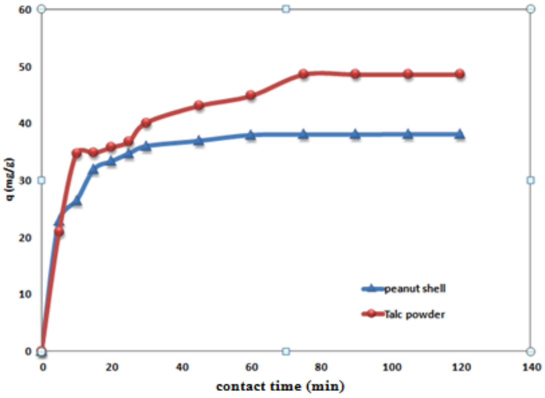

Fig. 5. Effect of contact time on the adsorption capacity of talc powder and peanut shells for hexavalent chromium (initial conc. 3000 mg L^{-1}, adsorbent dosage 0.5 g L^{-1}, temp. 25°C, pH=4.0, 400 rpm)

Effect of adsorbent dosage

Under optimum conditions of stirring and pH, the effect of adsorbent dosage on the adsorption of hexavalent chromium was studied by stirring 100 mL of 3000 mg L^{-1} of hexavalent chromium solution with 0.5 – 3 g L^{-1} of adsorbent for 1 h at 25°C and constant pH 4. The results of the experiments with varying adsorbent dosage are presented in Fig. 6. It was found that the % removal for talc powder increases from 50 to 77 % as the adsorbent dosage is increased from 0.5 to 3.0 g L^{-1}, while that for peanut shells increased from 36 to 72 %. This can be explained by the fact that the more the mass of adsorbent available, the more contact surface is offered to adsorption, resulting in an adsorbate-adsorbent equilibrium. Interestingly, up to 1.5 g L^{-1} both talc powder and peanut shells show similar % removal. However, talc powder shows higher efficiency resulting from the higher surface area exposure for adsorption and lower mass transfer resistance due to the available porous structure and volume.

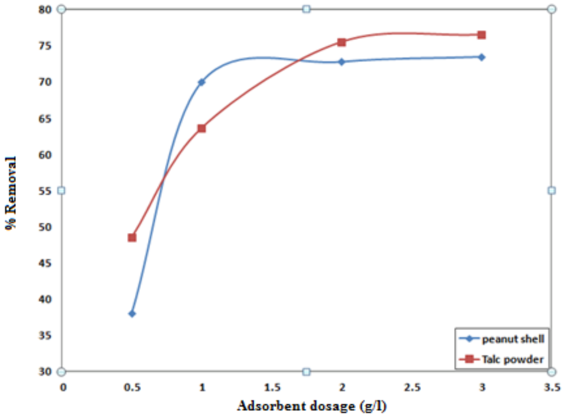

Fig. 6. Effect of dosage of talc powder and peanut shells on hexavalent chromium removal (initial conc. 3000 mg L^{-1}, pH=4.0, temp. 25°C, 400 rpm)

Effect of pH of the solution

In order to optimize the pH for maximum removal efficiency, batch experiments at 25°C were carried out using 100 mL of 3000 mg L^{-1} hexavalent chromium solution with 0.5 g of the adsorbents. The solution pH was continuously adjusted with H_2SO_4 and NaOH solutions for 1 h at pH values of 1, 3, 4, 7 and 9. The results obtained are shown in Fig. 7 which depicts the significant effect of pH on the adsorption of hexavalent chromium on talc powder and peanut shells. Solution pH is one of the most important variables affecting the adsorption characteristics and mechanism. The adsorption of hexavalent chromium was favored when the initial solution pH was between 3.5 and 5.0; the adsorption efficiency decreased slightly as the solution pH increased from 4 to 5. However, a sharp decline in hexavalent chromium adsorption occurred when pH was lower than 3.0 or higher than 5. The pH dependence of metal adsorption is largely related to the ionic forms of chromium in the solution and the surface properties of the adsorbent [32]. Thus, not only pH affects surface modifications of the available functional groups on the adsorbent, but it also disposes the proper ionic formation of the type of chromium to be accessible for the adsorption process.

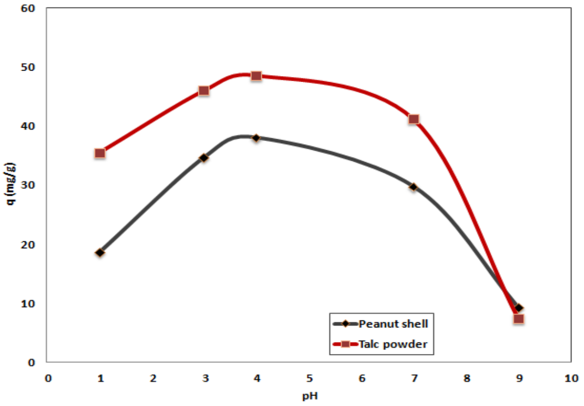

Fig. 7. Effect of pH on sorption capacity of talc powder and peanut shells for hexavalent chromium (initial conc. 3000 mg L^{-1}, adsorbent dosage 0.5 g L^{-1}, temp. 25° C, 400 rpm)

Hexavalent chromium exists in different ionic forms in solution. The most important hexavalent chromium states in solution are chromate (CrO_4^{2-}), dichromate ($Cr_2O_7^{2-}$) and hydrogen chromate ($HCrO^{4-}$), depending on the solution pH and total chromate concentration. From the stability diagram of the Cr(VI)–H_2O system, it is evident that at low pH, acid chromate ions ($HCrO_4^{-}$) are the dominant species which might interact strongly with the surface hydroxyl groups in peanut shells and mineral acidization is followed by chemical complex formation. The optimum pH value was found to be 4, which fits well with similar results obtained with agricultural nuts and shells and biomass-derived active carbons in the literature [33, 34, 24]. When the pH was further increased, a sharp decrease in the adsorption capacity was observed. This might be due to the weakening of the electrostatic force of attraction between the oppositely charged adsorbate and adsorbent and ultimately leads to a reduction in sorption capacity. When the pH was increased beyond 6, a decrease in the percentage adsorption was observed. This might be due to the competition between OH^{-} and chromate ions (CrO_4^{2-}), the former being the dominant species in the pH range outweighing the reaction. The net positive surface potential of the adsorbent decreased with increasing pH resulting in weakening of the electrostatic force between adsorbate and adsorbent which ultimately led to lowering of the adsorption capacity. Talc powder is insoluble in many mineral acids. However, in dilute acids it might slightly dissolve at pH 4 and 5, which might result in chemical interaction with the other elements in the solution.

Modeling of adsorption isotherms

Equilibrium adsorption isotherms are mathematical equations which are used to describe the relationship between the distribution and concentration of adsorbate and adsorbent. Rate expressions and reaction mechanisms of adsorption are of importance in understanding and designing adsorption systems, provided that a set of assumptions is taken into account, such as heterogeneous, homogeneous, surface coverage, diffusion, and interactions between sorbate and sorbent. Due to the complex physicochemical properties of micro/mesoporous structures, flow patterns and chemical nature of the liquid-solid phase process, adsorption models differ to some extent for practical application. The most widely accepted surface adsorption models for single-solute systems are the Langmuir and the Freundlich models. The correlation between the adsorbed amount and the liquid-phase concentration was tested with Langmuir, and Freundlich, whereas Temkin and Dubinin–Radushkevich (D–R) provided further information on the energy of adsorption and mechanism. The applicability of isotherm equations is compared by relating the correlation coefficients that fit the experimental data.

The Langmuir isotherm

Langmuir equation is the most widely applied model for isotherm adsorption as it considers that the adsorption energy of each molecule is constant on the finite number of identical adsorption sites and that adsorption takes place only on a monolayer until saturation with no interactions between the molecules**.**

The adsorption data were tested using Langmuir isotherm equation in the linearized form:

$$\frac{C_e}{q_e} = \frac{1}{q_{max} b} + \frac{1}{q_{max}} C_e \qquad (2)$$

where: C_e is the equilibrium concentration of hexavalent chromium in solution (mg L^{-1}), q_e is the adsorption capacity at equilibrium (mg g^{-1}), and b (L mg^{-1}) and q_{max} (mg g^{-1}) are Langmuir constants, related to the binding constant and the maximum adsorption capacity, respectively.

A plot of the specific sorption (C_e/q_e) *versus* C_e gives a straight line with a slope ($1/q_{max}$) and an intercept ($1/q_{max}$ b). The correlation coefficients shown in Table 2 (R^2 varying between 0.76 and 0.89 for talc powder, and R^2 >0.95 for peanut shells) suggest that the Langmuir adsorption isotherm does not fit well the situation for talc powder whereas it describes the case of adsorption on peanut shell very well.

The Freundlich isotherm

The Freundlich isotherm can be derived assuming a logarithmic decrease in the enthalpy of sorption with the increase in the fraction of occupied sites and is commonly given by the following non-linear equation:

Table 2. Isotherm models for adsorption of hexavalent chromium on talc powder

Isotherm equation	Isotherm parameters	Temperature (°C)			
		15	25	35	45
Langmuir $Ce/qe=1/b\ q_{max}+Ce/q_{max}$	b (L mg^{-1})	0.0025	0.0030	0.00321	0.00390
	q_{max} (mg g^{-1})	25.2525	25.3164	26.3852	26.5957
	R^2	0.7557	0.8322	0.8486	0.89
Freundlich $\log q_e= \log K_f+(1/n) \log C_e$	$1/n$	0.470	0.472	0.391	0.468
	K_F(L mg^{-1})	0.6889	0.032	1.0744	0.87437
	R^2	0.935	0.9538	0.8539	0.9482
Temkin $q_e=B_1 \ln K+B1 \ln Ce$	B_1	4.2867	4.447	3.4233	4.7988
	K (L mg^{-1})	0.0540	0.0587	0.0934	0.002288
	b(kJ mol^{-1})	115.241	108.252	103.513	101.316
	R^2	0.7977	0.84	0.6741	0.8808
D-R $\ln q_e=\ln Q_m - B\ \varepsilon^2$	Q_m (mg g^{-1})	12.98117	13.994	12.472	16.1577
	B (mol^2 kJ^{-2})	0.068	0.0243	0.0102	0.0068
	E (kJ mol^{-1})	2.7116	4.536	7.001	8.5749
	R^2	0.6991	0.7575	0.7746	0.8281

Table 3. Isotherm models for adsorption of hexavalent chromium on peanut shells

Isotherm equation	Isotherm parameters	Temperature (°C)			
		20	30	40	50
Langmuir *$Ce/qe=1/b\ q_{max}+Ce/q_{max}$*	b (L mg^{-1})	0.001085	0.001364	0.001589	0.001238
	q_{max} (mg g^{-1})	128.2051	135.1351	138.8889	147.0588
	R^2	0.9766	0.9534	0.9619	0.9697
Freundlich *$\log q_e= \log K_f+(1/n) \log C_e$*	1/n	0.6965	0.6426	0.6228	0.6609
	K_F(L mg^{-1})	0.490456	0.82699	1.046405	0.64759
	R^2	0.9651	0.966	0.9641	0.9751
Temkin *$q_e=B_1\ \ln K+B1\ \ln Ce$*	B_1	21.499	22.887	23.935	24.454
	K (L mg^{-1})	0.023343	0.028956	0.033082	0.027158
	b(kJ mol^{-1})	577.967	577.133	560.118	516.289
	R^2	0.9468	0.9297	0.9374	0.9314
D-R *$\ln q_e=\ln Q_m - B\ \varepsilon^2$*	Q_m (mg g^{-1})	60.71556	68.10155	73.61141	70.23874
	B (mol^2 kJ^{-2})	0.07	0.04	0.03	0.04
	E (kJ mol^{-1})	2.672612	3.535534	4.082483	3.535534
	R^2	0.8825	0.8756	0.8782	0.8651

$$q_e = K_F C_e^{1/n} \qquad (3)$$

where K_F is a Freundlich constant related to the bonding energy. K_F can be defined as the adsorption or distribution coefficient and represents the quantity of hexavalent chromium adsorbed onto the adsorbent for unit equilibrium concentration. The value of $1/n$ indicates the adsorption intensity of hexavalent chromium onto the sorbent with surface heterogeneity, becoming more heterogeneous as its value gets closer to zero. A value for $1/n$ below 1 indicates a normal Langmuir isotherm while $1/n$ above 1 is indicative of cooperative adsorption. Eq. (3) can be linearized to the logarithmic Eq. (4) and the Freundlich constants can be determined:

$$\log q_e = \log K_F + \frac{1}{n} \log C_e \qquad (4)$$

The applicability of the Freundlich sorption isotherm was analyzed using the same set of experimental data, by plotting log(q_e) *versus* log(C_e). The data obtained from the linear Freundlich isotherm plot for the adsorption of hexavalent chromium on talc powder are presented in Table 2, while those for the adsorption of hexavalent chromium on peanut shells are presented in Table 3. The correlation coefficients (>0.94) showed that the Freundlich model fits well to both types of adsorbents. A higher value of n between 2 and 10 (a smaller value of 1/n) indicates a favorable and stronger interaction during adsorption, n = 1 - 2 reveals moderate adsorption while less than 1 means poor performance [35]. The n value for talc powder is higher than 2 and thus shows favorable adsorption, while it is approximately 2 for peanut shells.

The Temkin isotherm

The Temkin adsorption isotherm model was used to evaluate the adsorption potentials of talc powder and peanut shells for hexavalent chromium. The derivation of the Temkin isotherm assumes that the fall in the heat of sorption is linear rather than logarithmic, as implied in the Freundlich equation. The Temkin isotherm has been commonly applied according to the following equation [36, 37]:

$$\mathrm{q_e} = \frac{\mathrm{RT}}{\mathrm{b}} \ln(\mathrm{KC_e}) \qquad (5)$$

The Temkin isotherm Eq. (5) can be simplified to the following equation:

$$q_e = B1 \ln(K) + B1 \ln(C_e) \qquad (6)$$

where: B1= $(RT)/b$, T is the absolute temperature (K) and R is the universal gas constant, 8.314 J mol^{-1} K^{-1}. The constant b is related to the heat of adsorption. The adsorption data were analyzed according to the linear form of the Temkin isotherm equation (6) and the values of the linear isotherm constants and coefficients are presented in Tables 2 and 3, respectively.

Examination of the data obtained shows that the Temkin isotherm fitted the hexavalent chromium adsorption data on peanut shells better than those for talc powder. The heat of hexavalent chromium adsorption by talc powder was found to be less than that for peanut shells, where the correlation coefficient is also less pronounced. The correlation coefficients R^2 obtained from the Temkin model were less comparable to those obtained from the Langmuir and Freundlich equations for peanut shells.

The Dubinin–Radushkevich (D–R) isotherm

The D–R model was also applied to estimate the characteristic porosity of the adsorbent, the apparent energy of adsorption and the characteristics of adsorption on micropores rather than of layer-by-layer adsorption [38, 39]. The D–R isotherm does not assume homogeneous surface or constant sorption potential. The D–R model has commonly been applied by Eq. (7) with its linear form as shown in Eq. (8):

$$q_e = Q_m \exp(-B\varepsilon^2) \quad (7)$$

$$\ln q_e = \ln Q_m - B\varepsilon^2 \quad (8)$$

where B is a constant related to the adsorption energy (mol^2 kJ^{-2}), Q_m is the theoretical saturation capacity (mg g^{-1}), ε is the Polanyi potential, calculated from Eq. (9).

$$\varepsilon = RT \ln(1 + \frac{1}{Ce}) \quad (9)$$

The slope of the plot of lnq_e *versus* ε^2 gives B and the intercept yields the adsorption capacity Q_m (mg g^{-1}). The mean free energy of adsorption, E (kJ mol^{-1}), defined as the free energy change when one mol of ion is transferred from infinity to the surface of the solid, was calculated from the B value using the following relations [40]:

$$E = -\frac{1}{\sqrt{(2B)}} \quad (10)$$

The values of E calculated using Eq. (10) for the present case were found to vary between 2.67 and 4.08 kJ mol^{-1} for peanut shells and between 2.7 and 8.6 kJ mol^{-1} for talc powder. The values of the mean free energy of adsorption observed in this study for both adsorbents fall between 2.7 and 8.6 kJ mol^{-1}, showing the type of adsorption to be physisorption (physical sorption) [41]. The energy of adsorption also shows that it increases with temperature for the talc powder, while no significant dependence on temperature is shown for the peanut shells.

Kinetics of adsorption

Adsorption kinetics is important as it controls the process efficiency as the rate of uptake of the chromium species on the adsorbent is equilibrated with time. The kinetics of Cr(VI) adsorption on peanut shells and talc powder were analyzed using pseudo-first order, pseudo-second order and intraparticle diffusion models. The pseudo-first order Lagergren rate expression may be written as follows [42]:

$$\log(q_e - q_t) = \log q_e - \frac{k_1}{2.303} t \quad (11)$$

where q_e and q_t are the amounts of hexavalent chromium adsorbed on the two adsorbents at equilibrium and at time *t*, respectively (both in mg g^{-1}), and k_1 is the rate constant (min^{-1}). The values of q_e and k_1 are obtained from the intercept and the slope of the plot of log (q_e-q_t) as a function of time (t) and these values are given in Table. 4

Table 4. Kinetic parameters of the adsorption of hexavalent chromium onto talc powder and peanut shells

Kinetics model	peanut shells	talc powder
Pseudo-first order		
k_1 (min^{-1})	0.128	0.1609
$q_{e\ Calc}$ (mg g^{-1})	39.6	42.476
$q_{Exp.}$(mg g^{-1})	38	45
R_1^2	0.9745	0.9936
Pseudo-second order		
k_2 (g mg^{-1} min^{-1})	0.0052	0.334
$q_{e\ Calc.}$(mg g^{-1})	38.87	39.88
$q_{Exp..}$(mg g^{-1})	38	45
R_2^2	0.9364	0.8929
Intraparticle diffusion		
k_d (mg g^{-1} min$^{-1/2}$)	6.5887	0.8865
c	0.5688	0.022
R^2	0.9886	0.9979

The pseudo-second order kinetic model is expressed by the following relationship [43]:

$$\frac{t}{q_t} = \frac{1}{k_2 q_e^2} + \frac{1}{q_e} t \quad (12)$$

where k_2 is the equilibrium rate constant (g mg^{-1}min^{-1}). The rate constant and q_e were obtained from the slope and the intercept of the t/q_t vs. time (t) dependence. The kinetic parameters along with the correlation coefficients of the kinetic models are also shown in Table (4).

As can be seen from Table 4, higher correlation coefficients (R_1^2) were obtained using the pseudo-first order equation and the calculated q_e values were reasonably close to the experimental data obtained, indicating that the pseudo-first order kinetic model is more suitable to describe the kinetics of the adsorption process of hexavalent chromium on talc powder and peanut shells.

The adsorbate transport from the bulk solution phase to the internal active sites occurs in several steps, where the rate of internal mass transfer is, in most cases, the rate-determining step in adsorption processes. Kinetic data were therefore used to check the possibility of intraparticle diffusion limitations by using the Weber and Morris equation [44], expressed by the following equation:

$$q_t = k_d\, t^{0.5} + c \quad (13)$$

where q_t (mg g^{-1}) is the amount of adsorbed Cr(VI) at time t and k_d is the intraparticle diffusion rate constant (mg g^{-1} min$^{-0.5}$), and c is a constant determined from the intercept.

If the plot of q_t *versus* $t^{0.5}$ gives a straight line passing through the origin, then the adsorption process is only controlled by intraparticle diffusion. However, if the data exhibit multi-linear plots, then two or more stages influence the adsorption process. Figs. 8 and 9 are the plots of q_t *versus* $t^{0.5}$ for peanut shells and talc powder, respectively, which clearly show multilinearity. The multi-linear behavior of the plots of q_t *versus* $t^{0.5}$ is due to the extensive pore size distribution of the studied adsorbents having micro-, meso- and macroporosity. The first one could be attributed to the adsorption of hexavalent chromium over the surface with macropore structure of both adsorbents, and hence it is the fastest adsorption stage. The second one could be ascribed to the intraparticle diffusion through the mesopores, while the third stage may be regarded as diffusion through micropores, and of course, this stage is followed forthwith by the establishment of equilibrium. Table 4 also gives the linear correlation coefficient (>0.98) showing high applicability of the kinetic model of the intraparticle diffusion for both adsorbents.

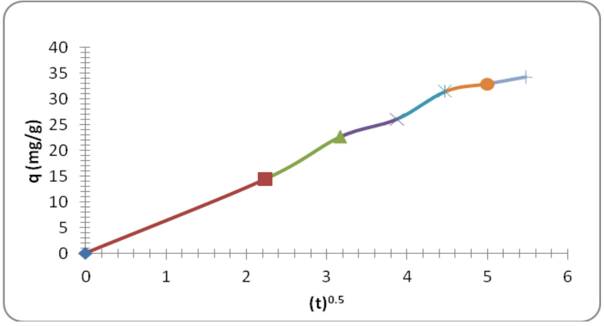

Fig. 8. Intraparticle diffusion for adsorption of hexavalent chromium on peanut shells

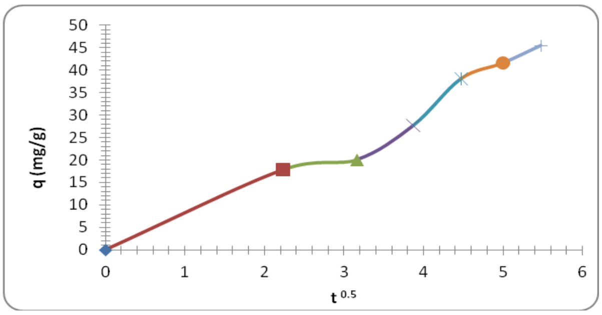

Fig. 9. Intraparticle diffusion for adsorption of hexavalent chromium on talc powder

CONCLUSION

In this study, two abundant natural resources (talc powder and peanut shells) were used as adsorbents for removing hexavalent chromium from simulated wastewater. Different parameters that are known to affect the adsorption process were studied, namely: contact time, amount of adsorbents, and pH of the solution. It was found that the adsorption process using the two adsorbents is simple, fast and reached equilibrium within 30 min for peanut shells and 70 min for talc powder. The adsorption capacity increased with increasing the amount of adsorbent. The optimum pH value for the adsorprion of hexavalent chromium was found to be 4.0. The experimental results were analyzed by using Langmuir, Freundlich, Temkin and Dubinin–Radushkevich isotherm models and the correlation coefficients showed that while Freundlich fitted well with talc powder, peanut shells showed validity for both Langmuir and Freundlich for the adsorption of Cr(VI). The kinetic study of the adsorption of hexavalent chromium on talc powder and peanut shells revealed that they are better described by the pseudo-first order with intraparticle diffusion models. It can be concluded that talc powder and peanut shells could be employed as low-cost adsorbents for the removal of hexavalent chromium from waste water.

Acknowledgement: *The respective Universities and Institutes are acknowledged for their support of this study.*

REFERENCES

1. C.M. Hogan, Heavy metal Encyclopedia of Earth, National Council for Science and the Environment. eds. E. Monosson & C. Cleveland. Washington, D.C., 2010.
2. Y.W. Wu, Y.Y. Jiang, D.Y. Han, F. Wang, J.X. Zhu, Speciation of chromium in water using crosslinked chitosan-bound FeC nanoparticles as solid-phase extractant and determination by flame atomic absorption spectrometry, *Microchim. Acta*, 159 (2007) 333–339.
3. C. Oze, D.K. Bird, S. Fendorf, Genesis of hexavalent chromium from natural sources in soil and groundwater, *PNAS* 104 (2007) 6544-6549.
4. ATSDR, Toxicological profile for chromium. U. S. Department of Health and Human Services, Atlanta, GA, 1998.
5. M.F. Bergamini, D.P. Dos Santos, M.V.B. Zanoni, Development of a voltammetric sensor for chromium(VI) determination in wastewater sample, *Sens. Actuators*, B 123 (2007) 902–908.
6. EPA, Toxicological review of hexavalent chromium, National Center for Environmental Assessment, Washington DC, 1998
7. H. Cuia, M. Fu, S. Yu, M.K. Wang, Reduction and removal of Cr(VI) from aqueous solutions using modified byproducts of beer production, *J. Hazard. Mater*. 186 (2011) 1625–1631.
8. L.N. Døssing, K. Dideriksen , S.L.S. Stipp, R. Frei , Reduction of hexavalent chromium by ferrous iron: A

process of chromium isotope fractionation and its relevance to natural environments, *Chem. Geology* 285 (2011) 157–166.

9. M.S. Bhatti, A.S. Reddy, A.K. Thukral, Electrocoagulation removal of Cr(VI) from simulated wastewater using response surface methodology, *J. Hazard. Mater.* 172 (2009) 839–846.
10. H-T. Hsu, S-S. Chen, Y-S. Chen, Removal of chromium(VI) and naphthalenesulfonate from textile wastewater by photocatalysis combining ionic exchange membrane processes, *Sep. and Purif. Technol.* 80 (2011) 663–669
11. O.D. Uluozlu, M. Tuzen, D. Mendil, B. Kahveci, M. Soylak, 3-Ethyl-4- (p-chlorobenzylidenamino-4,5-dihydro-1H-1,2,4-triazol-5-one (EPHBAT) as precipitant for carrier element free co precipitation and speciation of chromium(III) and chromium(VI), *J. Hazard. Mater.* 172 (2009) 395–399.
12. T. Narukawa, K.W. Riley, D.H. French, K. Chiba, Short communication: speciation of chromium in Australian fly ash, *Talanta* 73 (2007) 178–184.
13. S. Kocaoba, G. Akcin, Removal and recovery of chromium and chromium speciation with MINTEQA2, *Talanta* 57 (2002) 23–30.
14. C.C. Liu, Y.S. Li , Biosorption of chromium, copper and zinc on rice wine processing waste sludge in fixed bed, *Desalination* 267 (2011) 20–24.
15. Z.A. Al-Othman, R. Ali, M. Naushad, Hexavalent chromium removal from aqueous medium by activated carbon prepared from peanut shell: Adsorption kinetics, equilibrium and thermodynamic studies, *Chem. Eng. J.* 184 (2012) 238–247.
16. N. Ballav, A. Maity , S.B. Mishra, High efficient removal of chromium(VI) using glycine doped polypyrrole adsorbent from aqueous solution, *Chem. Eng. J.* 198–199 (2012) 536–546.
17. S. Chen, Q. Yue, B. Gao, Q. Li, X. Xu, Removal of Cr(VI) from aqueous solution using modified corn stalks: Characteristic, equilibrium, kinetic and thermodynamic study, *Chem. Eng. J.* 168 (2011) 909–917.
18. N-H. Hsu, S-Li. Wang, Y-H. Liao, S-T. Huang, Y-M. Tzou, Y-M. Huang, Removal of hexavalent chromium from acidic aqueous solutions using rice straw-derived carbon, *J. Hazard. Mater*. 171 (2009) 1066-1070
19. M. Jain, V.K. Garg, K. Kadirvelu, Equilibrium and kinetic studies for sequestration of Cr(VI) from simulated wastewater using sunflower waste biomass, *J. Hazard. Mater*. 17 (2009) 328-334.
20. A. El-Sikaily, A. El Nemr, A. Khaled, O. Abdelwehab, Removal of toxic chromium from wastewater using green alga ulva lactuca and its activated carbon, *J. Hazard. Mater*. 148 (2007) 216-228
21. D. Park, S-R. Lim, Y-S. Yun, J.M. Park, Development of a new Cr(VI) from agricultural biowaste, *Bioresour. Technol*. 99 (2008) 8810-8818
22. M. Jain, V.K. Garg, K. Kadirvelu, Adsorption of hexavalent chromium from aqueous medium onto carbonaceous adsorbents prepared from waste biomass, *J. Environ. Manag*. 91 (2010) 949-957
23. P. Miretzky, A.F. Cirelli, Cr(VI) and Cr(III) removal from aqueous solution by raw and modified lignocellulosic materials: A review, *J. Hazard. Mater*. 180 (2010) 1-19
24. A. K. Giri, R. Patel, S. Mandal, Removal of Cr(VI) from aquaeous solution by *Eichhornia crassipes* root biomass-derived activated carbon, Chem. Eng. J. 185-186 (2012) 71-81
25. S. Yadav, V. Sirvastava, S. Banerjee, C-H. Weng, Y. C. Sharma, Adsorption characteristics of modified sand for the removal of hexavalent chromium ions from aqueous solutions, kinetic, thermodynamic, and equilibrium studies, *CATENA* 100 (2012) 120-127.
26. Y. Dong, F. Dayou, W. Rong, Y. Jigang, Rapid determination of chromium (VI) in electroplating waste water by use of a spectrophotometric flow injection system, *Spectrochim. Acta, Part A*, **71** (2008) 276-279.
27. P. Huang, D.W. Fuerstenau, *Colloids Surf.*, A, 177 (2–3), (2000), 147–156.
28. E.A-Varol, A.E. Pütün, Preparation and characterization of pyrolytic chars from different biomass samples, *J. Anal. Appl. Pyrolysis* 98 (2012) 29-36
29. R.P. Han, L.J. Zhang, C. Song, M.M. Zhang, H.M. Zhu, L.J. Zhang, Characterization of modified wheat straw, kinetic and equilibrium study about copper ion and methylene blue adsorption in batch mode, *Carbohydr. Polym*. 79 (2010) 1140–1149.
30. M. Sprynsskyy, R. G-Kopciuch, K. Nowak, B. Buszewski, *Colloids Surf*. B 94 (2012) 7-14.
31. L. Lagdic, M. K. Mitchell, B.D. Payne, Highly effective adsorption of heavy metal ions by a thiol-functionalized magnesium phyllosilicate clay, *Environ. Sci. Technol*. 35 (2001) 84-90.
32. U. K. Garg, M. P. Kaur, V. K. Garg, D. Sud, Removal of hexavalent chromium from aqueous solution by agricultural waste biomass, *J. Hazard. Mater*. 140 (2007) 60-68.
33. G:S. Agarwal, H.K. Bhuptawat, S. Chaudhari, Biosorption of aqueous chromium (VI) by tamarindus indica seeds, *Bioresour. Technol*. 97 (2006) 949-956.
34. G. Hunag, J. X. Shi, T. A. G. Langrish, Removal of Cr(VI) from aqueous solution using activated carbon modified by nitric acid, *Chem. Eng. J.* 152 (2009) 4343-439
35. R. Klimaviciute, J. Bendoraitiene, R. Rutkaite, A. Zamaitaitis, Adsorption of hexavalent chromium on cationic cross-linked starches of different botanic origins, *J. Hazard. Mater*. 181 (2010) 624-632.
36. C. Aharoni, D.L. Sparks, Kinetics of soil chemical reactions - a theoretical treatment, in: D.L. Sparks, D.L. Suarez (Eds.), Rate of Soil Chemical Processes, Soil Sci. Soc. Am., Madison, WI, (1991) 1–18.
37. C. Aharoni, M. Ungarish, Kinetics of activated chemisorption. Part 2. Theoretical models, *J. Chem. Soc., Faraday Trans*. 73 (1977) 456–464.

38. M.M. Dubinin, Modern state of the theory of volume filling of micropore adsorbents during adsorption of gases and steams on carbon adsorbents, *Zhurnal Fizicheskoi Khimii* 39 (1965) 1305–1317.
39. L.V. Radushkevich, Potential theory of sorption and structure of carbons, *Zhurnal Fizicheskoi Khimii* 23 (1949) 1410–1420.
40. S. Kundu, A.K. Gupta, Investigation on the adsorption efficiency of iron oxide coated cement (IOCC) towards As(V) - kinetics, equilibrium and thermodynamic studies, *Colloid Surf.* 273 (2006) 121–128.
41. V.J. Inglezakis, S.G. Poulopoulo, Adsorption, Ion exchange and Catalysis: Design, Operation and Environmental Application, Elsevier, Amsterdam, The Netherlands, 2006.
42. S. Lagergren, About the theory of the so-called adsorption of soluble substances, *K. Sv. Vetenskapsakad. Handl*. 24 (1898) 1-39.
43. Y.S. Ho, G. McKay, Pseudo-second order model for sorption processes, *Process Biochem*. 34 (1999) 451-465
44. W.J. Weber, J.C. Morris, Kinetics of adsorption on carbon from solution, *J. Sanit. Eng. Div. Am. Soc. Civ. Eng.* 89 (1963) 31-60

ИЗПОЛЗВАНЕ НА ЧЕРУПКИ ОТ ФЪСТЪЦИ И ПРАХ ОТ ТАЛК ЗА ОТСТРАНЯВАНЕ НА ШЕСТ-ВАЛЕНТЕН ХРОМ ОТ ВОДНИ РАЗТВОРИ

М.Е. Осман[1,2], М.С. Мансур[3], М.А. Фатах[1*], Н. Таха[2], И. Кирос[4]

[1] *Департамент по нефтохимично инженерство, Университет Фарос,Александрия, Египет*
[2]*Изследователски институт по информатика, CSRTA, Александрия, Египет*
[3] *Департамент по инженерна химия, Университет в Александрия, Александрия,Египет*
[4]*Департамент по инженерна химия и химична технология, KTH-Кралски технологичен институт,Стокхолм, Швеция*

Постъпила на 19 август, 2013 г.; коригирана на 28 октомври, 2013 г.

(Резюме)

В настоящата работа са изследвани черупки от фъстъци и прах от талк като потенциални адсорбенти за отстраняването на шест-валентен хром от водни разтвори. Оценени са ефектите на значими параметри, като времето на контакт, pH на средата и дозировката на адсорбента върху степента на адсорбция на хром (IV). Освен това е извършено охарактеризиране с методите FT-IR, SEM и BET за оценяване н физико-химичните свойства на материалите. Експерименталните данни показват че оптималното време на контакт за достигане на равновесие са фъстъчените черупки е 30 мин., а за праха от талк -70 мин. Оптималната киселинност на средата отговаря на pH за двата сорбента. Изпитани са изотермите на Лангмюир, Фройндлих, Тьомкин и Дубинин-Радушкевич за описание на равновесните данни, топлината и енергията на адсорбция за двата адсорбента. Определена е скоростта на адсорбция с помощта на кинетика на реакция от псевдо-първи порядък с вътрешна дифузия за двата адсорбента.

Bulgarian Chemical Communications, Volume 46, Number 3 (pp. 640 – 644) 2014

Sephadex LH-20 column chromatography of the hydrolysed lignan macromolecule of flaxseed

M. Janiak[1], A. Slavova-Kazakova[2], V. Kancheva[2], R. Amarowicz[1*]

[1]*Institute of Animal Reproduction and Food Research of the Polish Academy of Sciences, Olsztyn, Poland*
[2]*Institute of Organic Chemistry with Centre of Phytochemistry, Bulgarian Academy of Sciences, Sofia, Bulgaria*

Received July 26, 2013; Revised December 13, 2013

The lignan macromolecule (LM) was extracted from defatted flaxseeds using ethanol:dioxane (1:1, v/v) and then purified by Amberlite XAD-16 column chromatography with water and methanol as mobile phases. The LM was subjected to base hydrolysis (0.3 M NaOH, 2 days at room temperature under continuous stirring). Four general fractions (I-IV) containing phenolic compounds were obtained from the hydrolysate using Sephadex LH-20 column chromatography with methanol as mobile phase. Secoisolariciresinol diglucoside (SDG) was present in fractions I and II. The applied technique is useful prior to semi-preparative HPLC in the purification procedure of SDG to be used as a standard.

Keywords: flaxseed; lignan; macromolecule; chromatography; Sephadex LH-20

INTRODUCTION

Lignans are a class of diphenolic compounds generally containing a dibenzylbutane skeleton structure. In human nutrition the richest source of lignans is flaxseed (*Linum usitatissimum* L.) [1]. The main lignan of flaxseed is secoisolariciresinol diglucoside (SDG) [2]; it occurs in the plant in the form of a lignan macromolecule (LM). When flaxseeds are consumed, SDG is essentially converted by bacteria to “mammalian” lignans, namely enterodiol (ED) and enterolactone (EL) [3].

The antioxidant activity of extracts from flaxseed and isolated SDG has been confirmed by several authors using different experimental models [4-7]. The potential role of lignans in risk reduction of mammary and prostatic tumors has been confirmed in several studies [8-11]. The similarities in the chemical structures of ED and EL to estradiol have led to the suggestion that both ED and EL can act as weak estrogenic/antiestrogenic compounds [12].

Several chromatographic methods have been employed for the separation and determination of flaxseed phenolic compounds. These include the following: Sephadex LH-20, RP-8, and silica gel column chromatography; TLC; RP-HPLC; and SE-HPLC [3, 13-19].

The aim of this work was the application of a Sephadex LH-20 column with methanol as mobile phase for the separation of phenolic compounds liberated from a flaxseed extract after base hydrolysis. This chromatographic method can be used prior to semi-preparative HPLC in the purification of a SDG standard.

MATERIALS AND METHODS

Chemicals

All solvents used were of analytical grade unless otherwise specified. Methanol, hexane, and acetonitrile were acquired from the P.O.Ch. Company (Gliwice, Poland). Sephadex LH-20 and Amberlite XAD-16 were obtained from Sigma-Aldrich. RP-18 gel (40-63 μm) was purchased from Merck (Darmstadt, Germany).

Plant material

Ground, partially defatted flaxseeds were purchased from the “Ekoprodukt” company (Częstochowa, Poland).

Extract preparation

The material was defatted with hexane, after which the phenolic compounds were extracted using dioxane:ethanol (1:1, v/v) [17]. The extraction was carried out for 16 h at 60°C under continuous shaking in a water bath. Then, the solvent was evaporated using a Büchi Rotavapor R-200 at 40°C.

Extract purification

The extract of phenolic compounds was purified using column chromatography on Amberlite XAD-16 [20]. A 1.0 g portion of the extract was suspended in distilled water and was loaded on the column. Firstly, water-soluble compounds, mainly

---

* To whom all correspondence should be sent:
E-mail: r.amarowicz@pan.olsztyn.pl

sugars and low-molecular-weight organic acids, were eluted with distilled water and discarded. The solvent was then changed over to methanol which eluted the phenolic compounds. The solvent was removed from the collected fraction using the Rotavapor.

Hydrolysis

The purified extract was subjected to base hydrolysis. Briefly, the purified extract was suspended in 0.3 M NaOH, and left for 2 days at room temperature under continuous stirring. The obtained hydrolysate was acidified to pH 3.0 using 2 M HCl [17] and was subjected to column chromatography on RP-18 gel. Water-soluble compounds were eluted with distilled water and discarded, whereas compounds of interest were eluted with methanol. The solvent was removed from the collected fraction using the Rotavapor.

Sephadex LH-20 column chromatography

A 0.6 g portion of the hydrolysate obtained was dissolved in 8 ml of methanol and was applied to a chromatographic column (2 × 60 cm) packed with Sephadex LH-20 and was eluted with methanol. Fractions (5 ml) were collected using a fraction collector and their absorbance was measured at 280 and 320 nm, which are the characteristic wavelength maxima for SDG and hydroxycinnamates, the major phenolic constituents of flaxseed. Eluates were then pooled into major fractions, the solvent was evaporated and the residues were weighed.

UV spectra

UV spectra of individual fractions dissolved in methanol were recorded with a Beckman DU 7500 diode array spectrophotometer.

RP-HPLC

The separated fractions were analysed using a Luna C18 (250 × 4.6 mm, 5 μm; Phenomenex, Torrance, CA) column and a Shimadzu system consisting of two LC-10AD pumps, a SCTL 10 A system controller, and a SPD-M 10 A diode array detector. Gradient elution with acetonitrile:water:acetic acid (5:93:2, v/v/v) [solvent A] and acetonitrile:water:acetic acid (40:58:2, v/v/v) [solvent B], at 0-50 min from 0 to 100% solvent B was employed [16]. The concentration of the sample dissolved in methanol was 2 mg/ml, the injection volume was 20 μl, the flow rate was 1 ml/min. The separation of the compounds was monitored at 280 and 320 nm. The standard of SDG was separated from the hydrolysed LM using a semi-preparative Luna C18 (250 × 10 mm, 5 μm; Phenomenex) column. Flow rate of 3 ml/min and the same gradient elution were used. A volume of 500 μL was injected into the column.

RESULTS AND DISCUSSION

Four fractions (I-IV) containing phenolic compounds were obtained from the hydrolysed purified extract of flaxseed using Sephadex LH-20 column chromatography with methanol as the mobile phase (Fig. 1).

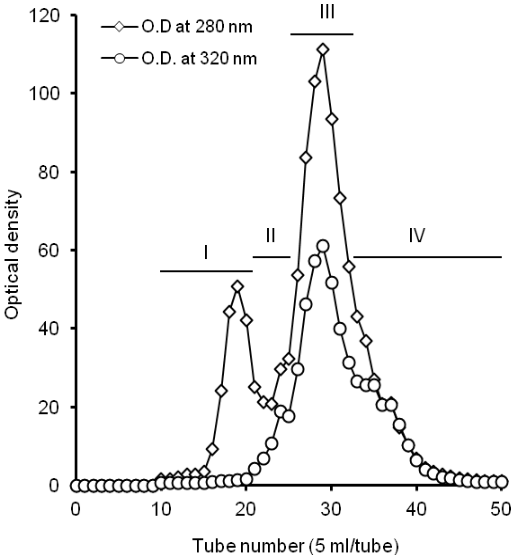

Fig. 1. Separation of phenolic compounds from a hydrolysed flaxseed molecule on a Sephadex LH-20 column with methanol as mobile phase.

The highest relative content of fraction I in the separated hydrolysate was at 53.5%, whereas the smallest content at 13.2% was determined for fraction IV (Table 1).

Table 1. Relative content of individual fractions separated using Sephadex LH-20 column chromatography and their UV spectral data

Fraction	Relative content (%)	λ_{max} (nm)	λ_{sh} (nm)
I	53.5	284	-
II	12.9	284	308
III	21.1	286	306
IV	12.5	286, 308	-

It is interesting to note that the highest content of total phenolic compounds was present in fraction III; the lowest content of total phenolics was found in fraction I.

The UV spectrum of fractions I and II exhibited a maximum at 284 nm. The absorption maxima for fractions III and IV were observed at the longer wavelengths of 286 and 308 nm, respectively (Fig. 2, Table 1).

These results demonstrate the absence of phenolic acids in the first two fractions.

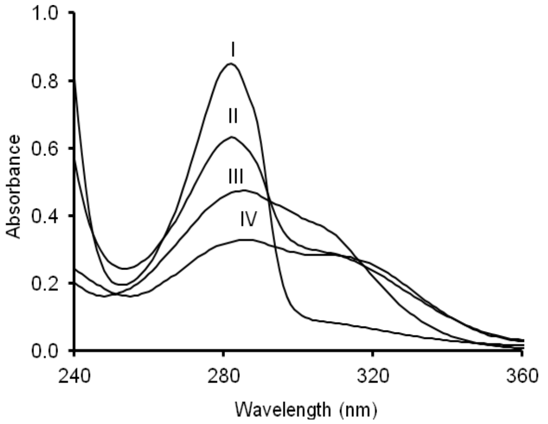

Fig. 2. UV spectra of the individual fractions separated on a Sephadex LH-20 column with methanol as mobile phase.

The RP-HPLC chromatogram of the hydrolyzed LM recorded at 280 nm is characterized by three main peaks (Fig. 3).

According to UV-DAD spectra and literature data [17], the first two peaks originated from glucosides of *p*-coumaric and ferulic acids (CoAG and FeAG). The peak with a retention time of 20.32 min originated from SDG. After Sephadex LH-20 column chromatography, SDG was observed in fractions I and II (Fig. 3). The content of SDG in fractions I and II was found to be534 and 464 mg/g, respectively. Approximately 82% of SDG was found in fraction I (Table 2). CoAG and FeAG were the dominant phenolic compounds present in fractions III and IV (Fig. 4).

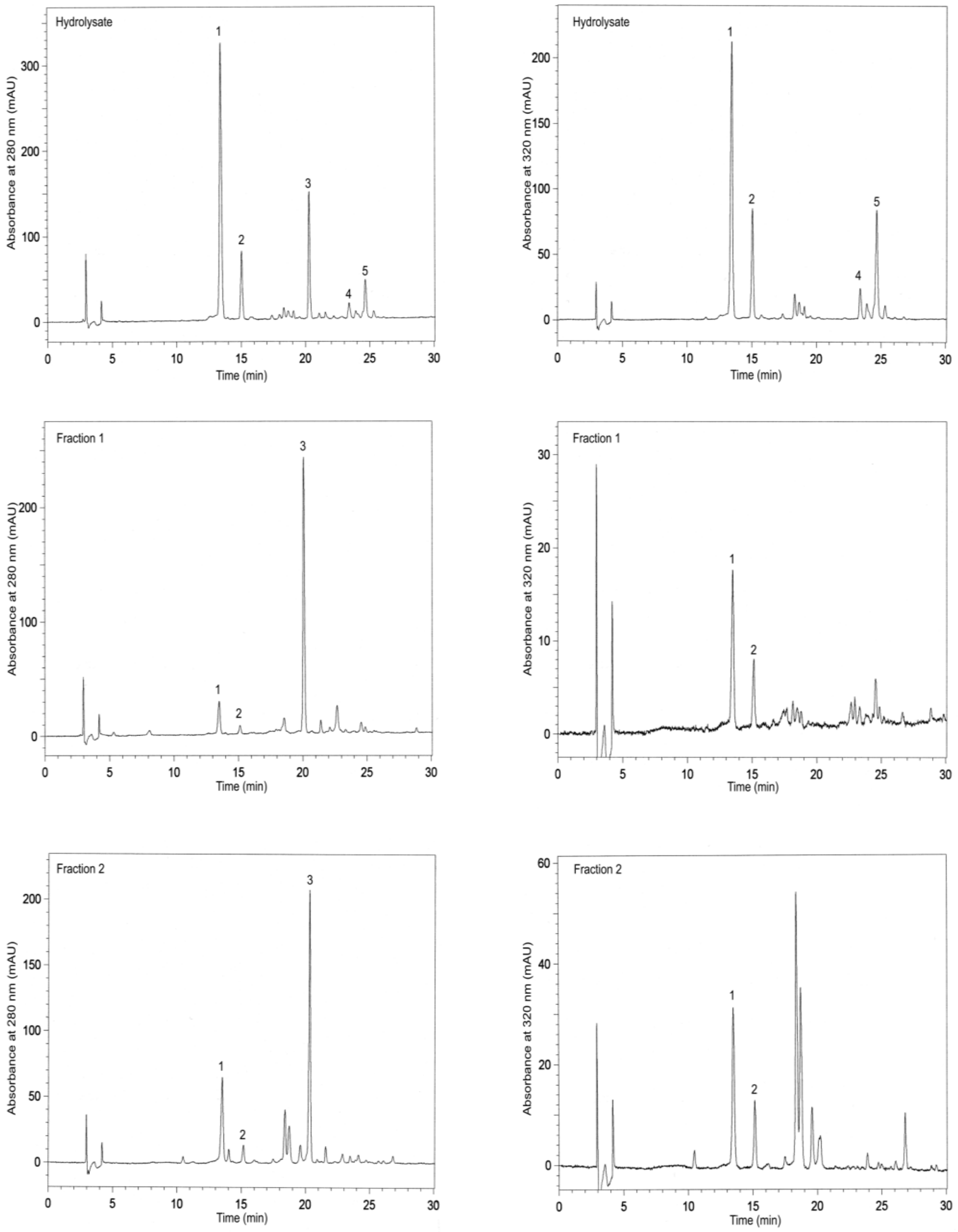

Fig. 3. RP-HPLC chromatograms of the extract and fractions I and II separated on a Sephadex LH-20 column with methanol as mobile phase; 1 – CoAG, 2 – FeAG, 3 – SDG, 4 and 5 – other phenolic compounds.

Table 2. Content of SDG in fractions separated using a sephadex LH-20 column

Fraction	Content of SDG (mg/g)	Relative content (% of total)
I	533	82.1
II	464	17.9
III	-	-
IV	-	-

CONCLUSION

Sephadex LH-20 column chromatography with methanol as mobile phase provides good separation of SDG and other low-molecular-weight phenolic compounds liberated from the flaxseed macromolecule after base hydrolysis. This chromatography seems to be a useful method prior to semi-preparative HPLC in the purification of SDG to be used as a standard.

Acknowledgments: *Financial support of Polish Academy of Sciences and Bulgarian Academy of Sciences for exchange visits are gratefully acknowledged.*

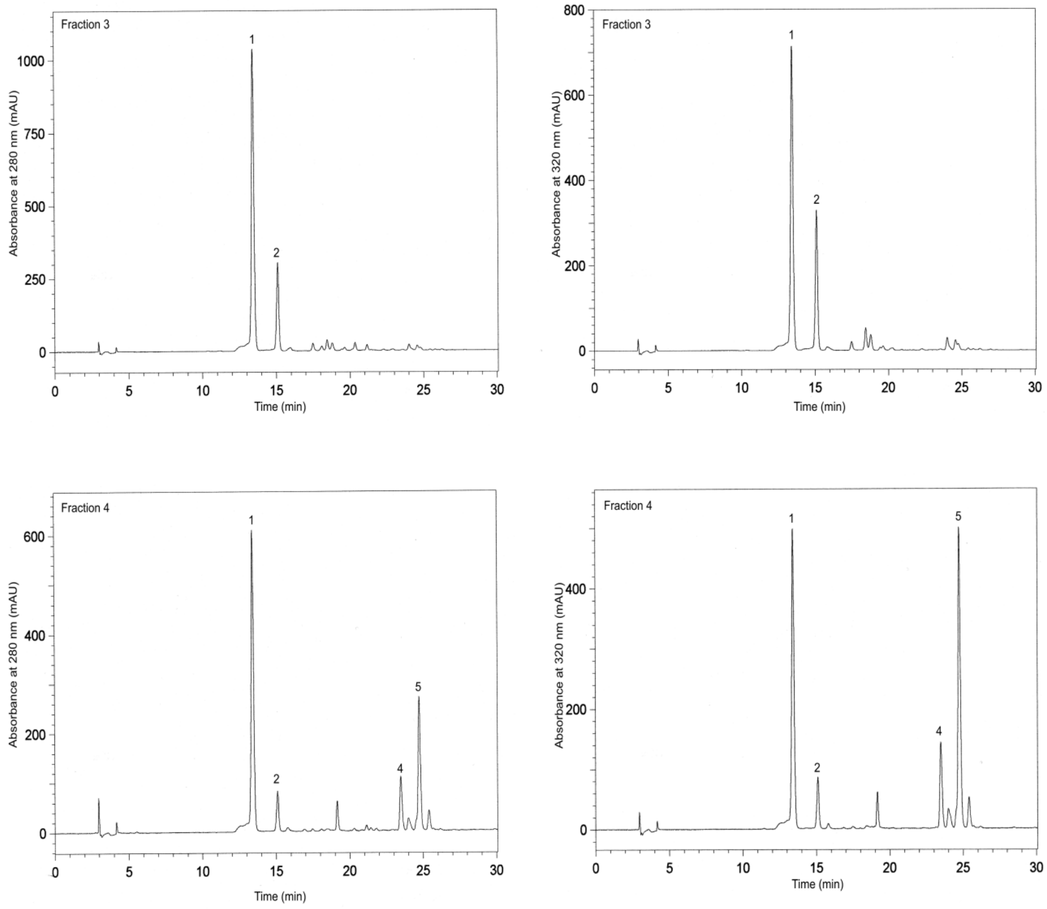

Fig. 4. RP-HPLC chromatograms of fractions III and IV separated on a Sephadex LH-20 column with methanol as mobile phase; 1 – CoAG, 2 – FeAG, 3 – SDG, 4 and 5 – other phenolic compounds.

REFERENCES

1. A. Eldin-Kamal, N. Peerlkamp, P. Johnsson, R. Andersson, R.E. Andersson, L.N. Lundgren, P. Åman, *Phytochem*. **58**, 587 (2001)
2. L.P. Meagher, G.R. Beecher, V.P. Flanagan,W. Li, *J. Agric. Food Chem*. **47**, 3173 (1999).
3. R. Amarowicz, U. Wanasundara, J. Wanasundara, F. Shahidi, *J. Food Lipids*, **1**, 111 (1993).
4. R. Amarowicz, M. Karamać, J.P.D. Wanasundara, F. Shahidi, *Nahrung-Food*, **41**, 178 (1997).
5. H.B. Niemeyer, M. Metzler, *J. Food Engin*. **56**, 255 (2003).
6. F.S. Hosseinian, A.D. Muir, N.D. Westcott, E.S. Krol, *J. Am. Oil. Chem. Soc*. **83**, 835 (2006)
7. C. Hu, Y.V. Yuan, D.D Kitts, *Food Chem. Toxicol.*, **45,** 2219 (2007).
8. M. Jenab, L.U. Thompson, *Carcinog.*, **17**, 1343 (1996).
9. H. Adlercreutz, *Lancet Oncol.*, **3**, 364 (2002).

10. X. Lin, J.R. Gingrich, W. Bao, J. Li, Z.A. Haroon, W. Demark-Wahnefried, *Urology*, **60**, 919 (2002).
11. F. Boccardo, G. Lunardi, P. Guglielmini, M. Parodi, R. Murialdo, G. Schettini, A. Rubagotti, *Eur. J. Cancer*., **40**, 84 (2004).
12. P. Nesbitt, L. Thompson, *Am. J. Clin Nutr*., **69**, 549 (1999).
13. R. Amarowicz, F. Shahidi, J. Liquid Chrom., **17**, 1291 (1994).
14. R. Amarowicz, P.K.J.P.D. Wanasundara, F. Shahidi, Nahrung-Food, **38**, 520 (1994).
15. K. Lorenc-Kukuła, R. Amarowicz, J. Oszmiański, P. Dermann, M. Starzycki, J. Skała, M. Żuk, A. Kulma, J. Szopa, *J. Agric. Food Chem*., **53**, 3685 (2005).
16. K. Lorenc-Kukuła, A. Kosińska, J. Szopa, R. Amarowicz, *Pol. J. Food Nutr. Sci*., **59**, 135 (2009).
17. P. Johnsson, N. Peerlkamp, A. Kamal-Eldin, R.E. Andersson, R. Andersson, L.N. Lundgren, P. Åman, *Food Chem.*, **76**, 207 (2002).
18. K. Struijs, J.-P. Vincken, R. Verhoef, A.G.J. Voragen, H. Gruppen, *Phytochem*., **69**, 1250 (2008).
19. A. Kosińska, A. Urbalewicz, K. Penkacik, M. Karamać, R. Amarowicz, *Pol. J. Food Nutr. Sci*., **61**, 263 (2011).
20. A. Srivastava, P. Greenspan, D.K. Hartle, L. James, J.L. Hargrove, R. Amarowicz, R.B. Pegg, *J. Agric. Food Chem*., **58**, 6102 (2010).

КОЛОННА ХРОМАТОГРАФИЯ СЪС SEPHADEX LH-20 НА ХИДРОЛИЗИРАНА ЛИГНАНОВА МАКРОМОЛЕКУЛА ОТ ЛЕНЕНО СЕМЕ

М. Яниак[1], А. Славова-Казакова[2], В. Кънчева[2] , Р.Амарович[1*]

[1]*Итститут по рерлодуктивност на животни и изследване на храни, Полска академия на науките, ул. „Тувима” 10, 10-748 Олщин, Полша и*
[2]*Институт по органична химия с Център по фитохимиа – Българска академия на науките, бул. „акад. Г.Бончев”, бл. 9,София 1113, България*

(Резюме)

Лигнановата макромолекула (ЛМ) е екстрахирана от обезмаслено ленено семе, използвайки етанол/диоксан (1:1, v/v) и след това е пречистена с Amberlite XAD-16 колонна хроматография с вода и метанол като мобилни фази. Лигнановата макромолекула, ЛМ, е подложена след това на алкална хидролиза. Получени са четири фракции (I-IV), съдържащи фенолни съединения от хидролизирания пречистен естракт на ленено семе, използвайки Sephadex LH-20 колонна хроматография с метанол като мобилна фаза. Секоизо-ларицирезинол диглюкозид (СДГ) присъства във фракции I и II. Тази хроматография е полезна техника преди полу-препаративна високоефективна течна хроматография (ВЕТХ) при пречиднването на СДГ, използван като стандарт.

Bulgarian Chemical Communications, Volume 46, Number 3 (pp. 645– 651) 2014

Qualitative investigation of the convective boiling heat transfer of dilute Al_2O_3-water/glycerol solution inside the vertical annuli

M. M. Sarafraz*, F. Hormozi

Faculty of Chemical, Petroleum and Gas Engineering, Semnan University, Semnan, Iran

Received July 18, 2013; Revised February 22, 2014

In this work, the flow boiling heat transfer coefficient of Al_2O_3-water/glycerol nanofluids was experimentally investigated under different operating conditions. The influence of different operating parameters such as heat flux, mass flux and sub-cooling temperature, as well as concentration of nanofluids on the convective boiling heat transfer coefficient was studied and discussed. The results demonstrated that two heat transfer regions with different heat transfer mechanisms can be distinguished during the convective boiling of nanofluids, namely single-phase forced convection and two-phase nucleate boiling. The results also showed that with increasing the heat and mass fluxes, the heat transfer coefficient of nanofluid increases and with increasing the nanofluid concentration, the heat transfer coefficient decreases which is due to the deposition of nanoparticles on the heater surface. The sub-cooling temperature only influences the onset of nucleate boiling.

Keywords: Al_2O_3, water/glycerol, nanoparticles, forced convection, nucleate boiling

INTRODUCTION

Boiling and two-phase flow phenomena are used in a variety of industrial processes and applications, such as refrigeration, air-conditioning and heat pumping systems, energy conversion systems, heat exchange systems, chemical thermal processes, cooling of high-power electronic components, cooling of nuclear reactors, micro-fabricated fluidic systems, thermal processes in aerospace stations and bioengineering reactors [1]. In nuclear power applications, boiling heat transfer plays a key role both in the efficient energy transportation during the normal operation and in the successful decay heat removal for the transient accident condition, due to the large latent heat of water and the bubble-driven convection or turbulence. Specifically, to prevent the core melt down and to mitigate the leakage of radioactivity to the outside of the reactor vessel, successful removal of decay heat is necessary [2]. Solid particles of nominal size 1–100 nm are called nanoparticles, and low-concentration dispersions of such particles in a base fluid are called nanofluids. Nanofluids are known to display a significant increase in thermal conductivity over that of the base fluid [3-7]. Early studies on the utilization of nanofluids in flow and pool boiling have mainly focused on the critical heat flux and surface characteristics of a heating section, as well as on the thermal conductivity enhancement and the parameters that govern this behavior [8-17]. One may want some more information about the recent flow boiling heat transfer research [18-22]. In previous studies, most investigators pay more attention to the critical heat flux and surface characteristics of the heating sections. Less attention has been paid to the forced convective and flow boiling heat transfer coefficient of the nanofluid due to the undesirable deterioration of the heat transfer coefficient.

The purpose of this study is to experimentally measure the forced and nucleate flow boiling heat transfer coefficient of Al_2O_3-water/glycerol nanofluid and investigate the influence of different operating conditions such as heat flux, flow rate and volumetric concentrations of the test nanofluid as well as sub-cooling temperature on the single phase and two-phase flow-boiling of the Al_2O_3-water/glycerol nanofluid.

EXPERIMENTAL

Different volumetric concentrations of nanofluids were prepared using two-step methods. The Al_2O_3 nanoparticles (45-50 nm, PlasmaChem GmbH, Germany) were uniformly dispersed into the base fluid (70 vol % of water and 30 vol % of glycerol) to obtain a stable nanofluid. In the present work, deionized water was considered as the base fluid. Briefly, the preparation steps were:

---

* To whom all correspondence should be sent:
E-mail: mohamadmohsensarafraz@gmail.com

I. The mass of Al_2O_3 was weighed on a digital electronic balance (A&D EK Series Portable Balances, EK-1200i).

II. The weighed Al_2O_3 nanoparticles were added to the weighed water/glycerol mixture while it was agitated in a flask (using a magnetic motorized stirrer (Hanna instruments Co.) Also, 0. 1 vol. % of QF-STK190 dispersant was added to the nanofluid as a stabilizer. Experiments were carried out on the nanofluids to check their stability and dispersion. Dynamic light scattering (DLS) test was also done (using a Malvern DLS device) to check the nanoparticle size count.

III. UP400S ultrasonic Hielscher GmbH (400W / 24 kHz) was used to uniformly disperse the nanoparticles into the water/glycerol mixture.

In the present work, nanofluids with volumetric concentrations of 0.5%, 1% and 1.5% were prepared using 45-50 nm (claimed by manufacturer) Al_2O_3 nanoparticles and water/glycerol 70:30 base fluid. Particle size measurements and XRD test of the solid particles were performed to check the size and quality of nanoparticles. As can be seen in Fig.1, maximum size count corresponds to 45-50 nm nanoparticles.

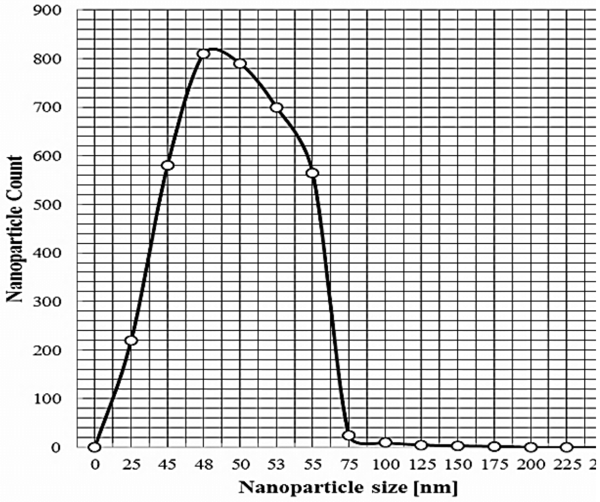

Fig. 1. Particle size distribution of Al_2O_3 nanoparticles

Fig. 2 depicts the TEM image of the Al_2O_3 nanoparticles. This image shows that particles are well dispersed in water/glycerol and there is no agglomeration and clustering inside the nanofluid. The XRD pattern (Fig. 3) depicts a single-phase Al_2O_3 with a monoclinic structure. No significant peaks of impurities are found in the XRD pattern. The peaks are broad due to the nano-size effect. The scheme of the experimental close loop is shown in Fig. 4. The working fluid enters the loop from a main tank through the isolated pipes and is continuously circulated by a centrifugal pump (DAB Co.). Due to the importance of the fluid flow rate in flow boiling heat transfer, a Netflix® ultrasonic flow meter was also installed in the fluid line to measure the flow rate. The fluid temperature was measured by two PT-100 thermometers installed in two thermo-wells located just before and after the annular section. Resistance thermometers or PT, also called resistance temperature detectors (RTDs), are the sensors used to measure the temperature by correlating the resistance of the RTD element with temperature. Most RTD elements consist of a fine coiled wire wrapped around a ceramic or glass core. This type of thermocouple is shown as PT-100. The complete cylinder was made from stainless steel 316a. Thermometer voltages, current and voltage drop from the test heater were all measured and processed with a data acquisition system in conjunction with a proportional-integral-differentiate (PID) temperature controller. The test section shown in Fig. 4 consists of an electrically heated cylindrical DC bolt heater (manufactured by Cetal Co.) with a stainless steel surface, mounted concentrically within the surrounding pipe. The

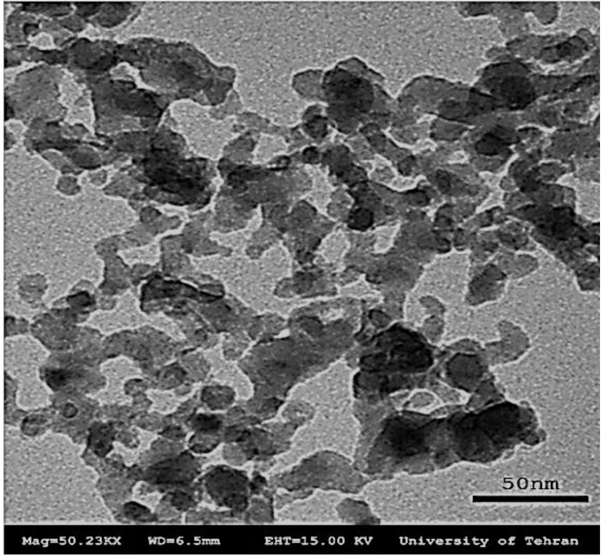

Fig. 2. TEM image of Al_2O_3 nanofluid; vol. %=1.5

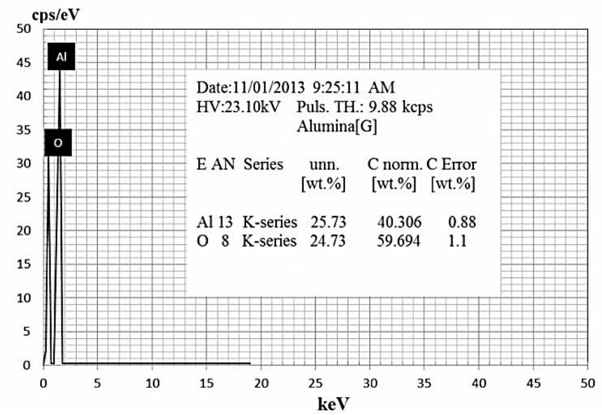

```
Date:11/01/2013  9:25:11  AM
HV:23.10kV   Puls. TH.: 9.88 kcps
             Alumina[G]

E AN  Series     unn.      C norm. C Error
                 [wt.%]    [wt.%]  [wt.%]

Al 13  K-series  25.73     40.306    0.88
O   8  K-series  24.73     59.694    1.1
```

Fig. 3. XRD results of Al_2O_3 solid nanoparticles

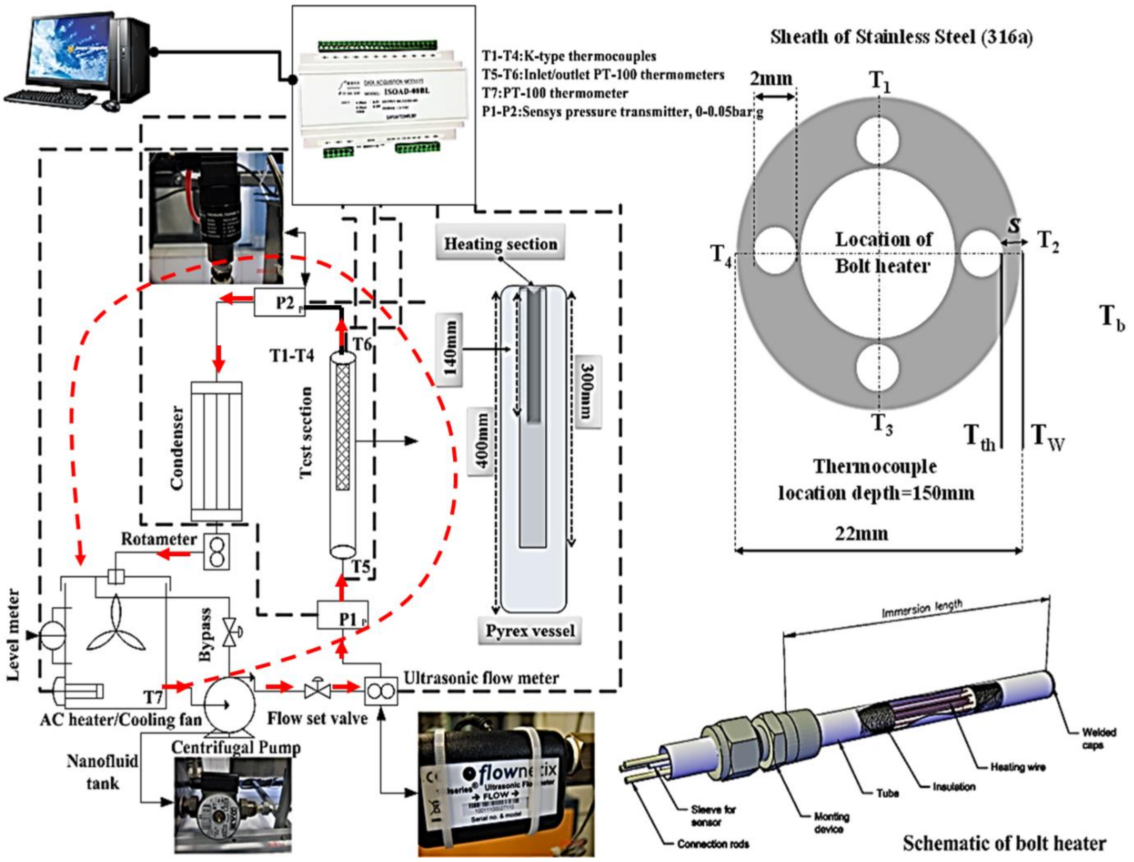

Fig. 4. Scheme of the test loop

dimensions of the test section are: diameter of heating rod 22 mm; annular gap diameter (hydraulic diameter) 30 mm; length of the pyrex tube 400 mm; length of stainless steel rod 300 mm; length of heated section 140 mm which means that just the first 140 mm of stainless steel are heated uniformly and radially by the heater. The axial heat transfer through the rod can be ignored because of the insulation of both ends of the heater. The heat flux and wall temperature can be as high as 190,000 W m^{-2} and 163°C, respectively. The local wall temperatures were measured with four stainless steel sheathed K-type thermocouples installed close to the heat transfer surface. The temperature drop between the thermocouples location and the heat transfer surface can be calculated from:

$$T_w = T_{th} - \dot{q}\,\frac{s}{\lambda_w} \tag{1}$$

The ratio between the distance of the thermometers from the surface and the thermal conductivity of the tube material (s/λ_w) was determined for each K-type thermocouple by calibration using the Wilson plot technique [23]. The average temperature difference for each test section was the arithmetic average of the four thermometers readings around the rod circumference. The average of 10 voltage readings was used to determine the difference between the wall and bulk temperature for each thermometer. All K-type thermocouples were thoroughly calibrated using a constant temperature water bath, and their accuracy was estimated to ±0.3K. The local heat transfer coefficient α was then calculated from:

$$\alpha = \frac{\dot{q}}{\left(T_w - T_b\right)_{ave.}} \tag{2}$$

To minimize the thermal contact resistance and temperature jump, high-quality silicone paste was injected into the thermocouple locations and also on the heater wall to expel the possible air from the center of the heating section and around the heater. To avoid possible heat loss, the main tank circumferences were heavily insulated using industrial glass wool. To control the fluctuations due to alternative current, a regular DC power supply was employed to supply the needed voltage to the central heater. Likewise, to visualize the flow and boiling phenomenon, the annulus was made of Pyrex glass.

The uncertainties of the experimental results were analyzed by the procedures proposed by Kline and McClintock [24]. The method is based on careful specification of the uncertainties in the various primary experimental measurements. The heat transfer coefficient can be obtained using Eq. (3):

$$\alpha = \frac{\rho V C_{pnf}(T_{out} - T_{in})}{(T_w - T_b)_{av.}} \tag{3}$$

As seen from Eq. (3), the uncertainty in the measurement of the heat transfer coefficient can be related to the errors in the measurements of volume flow rate, hydraulic diameter, and all temperatures, as follows:

$$\alpha = f\ \{V, A_h, (T_{out} - T_{in}), (T_w - T_b)\} \tag{4}$$

$$\partial\alpha = \sqrt{\left[\left(\frac{\partial\alpha}{\partial V}\right).\delta V\right]^2 + \left[\left(\frac{\partial\alpha}{\partial A}\right).\delta A\right]^2 + \left[\left(\frac{\partial\alpha}{\partial(\mathrm{Tout} - \mathrm{Tin})}\right).\delta(\mathrm{Tout} - \mathrm{Tin})\right]^2 + \left[\left(\frac{\partial\alpha}{\partial(\mathrm{Tw} - \mathrm{Tb})}\right).\delta(\mathrm{Tw} - \mathrm{Tb})\right]^2} \tag{5}$$

According to the above uncertainty analysis, the uncertainty in the measurement of the heat transfer coefficient was found to be 16.23%. The uncertainty of the equipment is presented in Table 1. The main source of uncertainty is the temperature measurement and its related devices.

Table 1. Summary of the uncertainty analysis

Parameter	**Uncertainty**
Length, width and thickness, (m)	±5×10^{-5}
Temperature, (K)	±0.3K
Water flow rate, (l. min^{-1})	±1.5% of readings
Voltage, (V)	±1% of readings
Current, (A)	±0.02% of readings
Cylinder side area, (m^2)	±4×10^{-8}
Flow boiling heat transfer coefficient, (W/m^2.K)	±16.23 **%**

RESULTS AND DISCUSSION

In this section, the effect of different operating parameters on the flow boiling heat transfer coefficient of Al_2O_3-water/glycerol is briefly discussed.

Effect of heat flux

The experimental results demonstrated that the heat transfer coefficient in both heat transfer regions is a direct function of the heat flux. On increasing the heat flux, the heat transfer coefficient of the nanofluid in both the forced convective and the nucleate boiling heat transfer regions significantly increases due to the increased number of nucleation active sites on the heater surface. On the other hand, on increasing the heat flux, the rate of bubble formation dramatically increases. Fig. 5 presents the influence of the heat flux on the convective boiling heat transfer of the Al_2O_3-water/glycerol solution. Fig. 6 depicts the effect of heat flux on bubble formation of nanofluids.

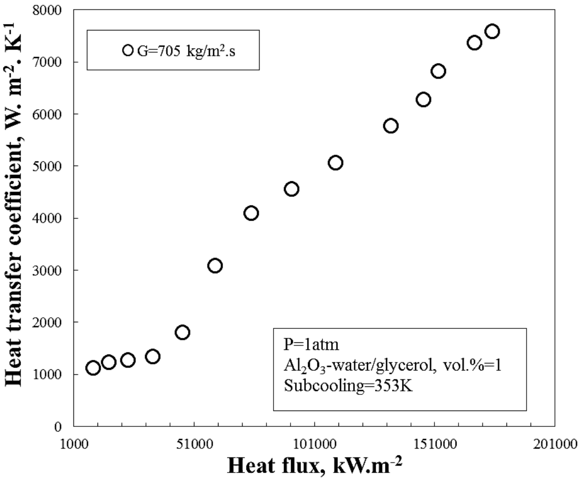

Fig. 5. Effect of heat flux on the flow boiling heat transfer coefficient of the Al_2O_3-water/glycerol nanofluid

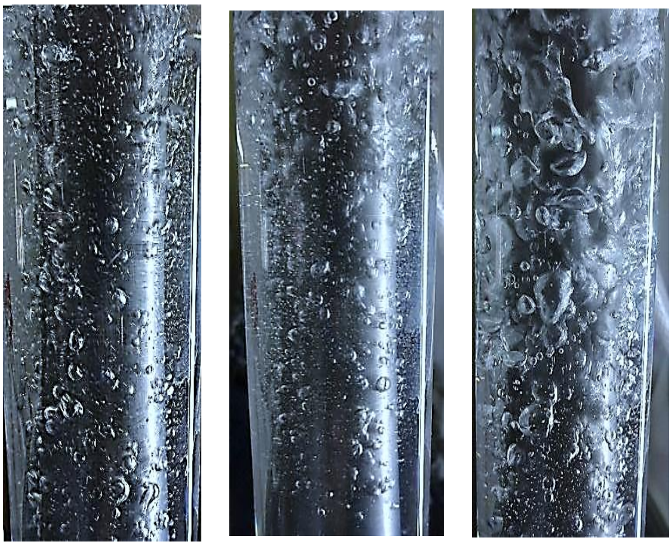

a) Heat flux 34kW/m^2

b) Heat flux 59kW/m^2

c) Heat flux 115kW/m^2

Fig. 6. Bubble formation in flow boiling heat transfer of the Al_2O_3-water/glycerol nanofluid

Effect of mass flux of fluid

Fluid flow rate (volumetric flux or mass flux) has a strong influence on the flow boiling heat transfer coefficient in both heat transfer regions. Experimental results showed that the heat transfer coefficient significantly increases when the fluid mass flux increases.

Fig. 7 presents the effect of fluid flow rate on the flow boiling heat transfer coefficient of Al_2O_3-water/glycerol nanofluids.

Effect of concentrations

The effect of concentration of nanofluids on the heat transfer coefficient in flow boiling of Al_2O_3-

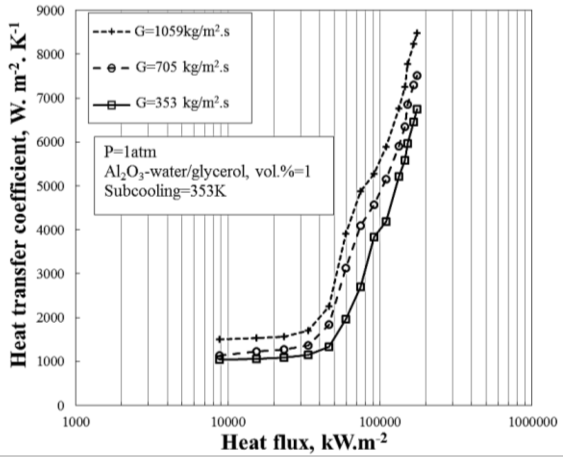

Fig. 7. Effect of mass flux on the heat transfer coefficient of the Al_2O_3-water/glycerol nanofluid

water/glycerol is represented in this section. As can be seen from figures 9 and 10, when the concentration of nanofluids increases, in the forced convective region the heat transfer coefficients increase, while for the nucleate boiling region, the heat transfer coefficients deteriorate. Due to the sedimentation of nanoparticles around the heating section and scales created on the surface, the surface heat transfer resistance increases and the surface becomes isolated against the heat transfer. Moreover, the surface characteristics significantly change and the surface wettability would also be affected by deposition, more bubbles covering the heating surface would lead the heat transfer to decrease. Fig. 8 illustrates the influence of concentration of nanofluids on the flow boiling heat transfer coefficient. For better understanding, the surface roughness was determined before and after the experiments. To this purpose the profile meter Elcometer-7061-MarSurf PS1 surface roughness tester was employed with uncertainty of ±0.2. According to roughness meter results, the surface roughness due to the presence of nanoparticles has significantly increased.

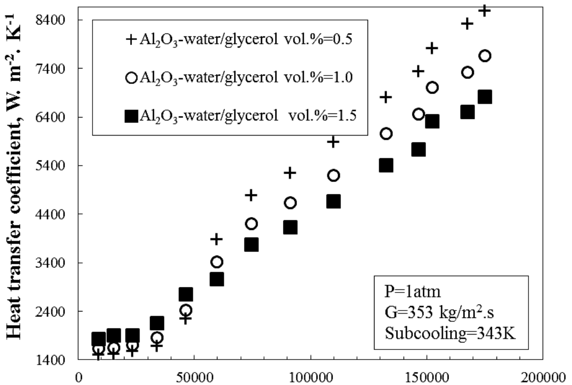

Fig. 8. Influence of the concentration of nanofluid on the flow boiling heat transfer coefficient

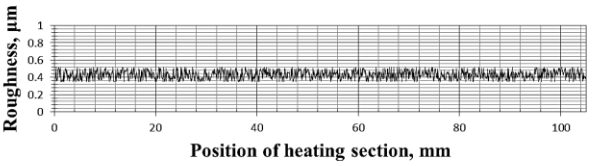

Fig. 9 Roughness of the heating section before scale formation on the surface

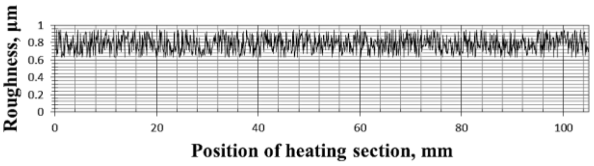

Fig. 10 Roughness of surface after the experiments; vol. %=1.5

Effect of sub-cooling temperature

Influence of the sub-cooling temperature can only be seen on the onset of nucleate boiling (ONB) point. In fact, ONB is the boundary separating the forced convective and the nucleate boiling heat transfer regions. However, the first bubble may be seen at this point or even not be seen by naked eyes. Briefly speaking, with increasing the sub-cooling temperature of the fluid, the heat flux corresponding to the ONB point significantly decreases. A small increase in the heat transfer coefficient in the nucleate boiling region is reported while no significant influence on the forced convective heat transfer coefficient is seen. Fig. 11 presents the influence of sub-cooling temperature on the flow boiling heat transfer coefficient of Al_2O_3-water/glycerol nanofluids.

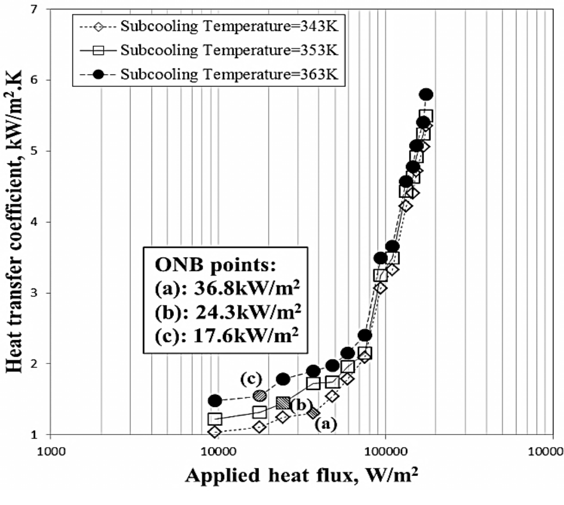

Fig. 11. Effect of sub-cooling temperature on the flow boiling heat transfer of the Al_2O_3-water/glycerol nanofluid

CONCLUSION

A large number of experiments were performed on the convective boiling heat transfer of Al_2O_3-water/glycerol nanofluids at different operating parameters and the following conclusions were drawn:

- Similar to previous studies, two significant heat transfer regions with different heat transfer mechanisms were observed, namely: forced convective and nucleate boiling.
- Investigations on the operating parameters indicated that both heat flux and mass flux had a direct influence on the heat transfer coefficient and the fouling resistance. On increasing the heat and mass fluxes, the heat transfer coefficient increases in both regions.
- On increasing the concentration of nanofluids, deterioration of heat transfer coefficients can be seen which is due to the deposition of nanoparticles on the heating surface.
- The only influence of sub-cooling temperature is to decrease the corresponding heat flux related to the onset of nucleate boiling. In fact, the higher the sub-cooling temperature, the lower corresponding heat flux related to ONB point is reported.
- Nanoparticles deposition can increase the flow pressure drop which was not studied in this work. It is recommended to conduct future research on the possible pressure drop of nanofluids in convective boiling heat transfer.

Acknowledgement: *The authors wish to dedicate this article to Imam Mahdi and appreciate for the financial support by Semnan University.*

NOMENCLATURE

A	area, m^2
b	distance, m
C_p	heat capacity, $J.kg^{-1}.^oC^{-1}$
d_h	hydraulic diameter, m
h	enthalpy, $J.\ kg^{-1}$
k	thermal conductivity, $W.m^{-1}.^oC^{-1}$
L	heater length, m
P	pressure, Pa
q	heat, W
s	distance, m
T	temperature, K

Subscripts-Superscripts

b	bulk
bs	base fluid
nf	nanofluid
c	critical
fb	flow boiling
in	inlet
out	outlet
l	liquid
m	mixture
n	number of components
nb	nucleate boiling
ONB	onset of nucleate boiling
Sat	saturated
th	thermometers
v	vapor
w	Wall

Greek symbols

α	heat transfer coefficient, $W.m^{-2}.K^{-1}$
ρ	density, $kg.m^{-3}$
μ	viscosity, $kg.m^{-1}.s^{-1}$
ϕ	Volume fraction

REFERENCES

1. T. Lee, J. H. Lee, Y. H. Jeong, *Int. J. Heat Mass Trans.* **56** 101, (2013).
2. L. Cheng, L. Liu, *Int. J. Refrigeration* **36**, 421, (2013).
3. S.U.S. Choi, Z.G. Zhang, W. Yu, F.E. Lockwood, E.A. Grulke, *Appl. Phys. Lett***.**, **79**, 2252, (2001).
4. S.K. Das, N. Putra, W. Roetzel, *Int. J. Heat Mass Trans.*, **46**, 851, (2003).
5. Y. Ding, H. Alias, D. Wen, R.A. Williams, *Int. J. Heat Mass Trans.*, **49**, 240, (2006).
6. M.M. Sarafraz, F. Hormozi, *Exp. Therm. Fluid Sci..*, **52**, 205, (2014).
7. M.M. Sarafraz, F. Hormozi, *Int. Commun. Heat Mass Trans..*, **53**, 116, (2014).
8. D. Wen, Y. Ding, *J. Nanoparticle Res.*, **7**, 265, (2005).
9. H. Kim, J. Kim, M.H. Kim, *Int. J. Heat Mass Trans.*, **49**, 5070, (2006).
10. S.J. Kim, I.C. Bang, J. Buongiorno, L.W. Hu, *Appl. Phys. Lett.*, **89**, 153, (2006)
11. H.D. Kim, J.B. Kim, M.H. Kim, *Int. J. Multiphase Flow*, **33**, 691, (2007).
12. S.J. Kim, I.C. Bang, J. Buongiorno, L.W. Hu, *Bull Polish Academy Sci. Tech. Sci*., **55,** 211, (2007).
13. M.M. Sarafraz, S.M. Peyghambarzadeh, *Exp. Therm. Fluid Sci.*, **50**, *154*, (2013).
14. T.I. Kim, Y.H. Jeong, S.H. Chang, *Int. J. Heat Mass Trans.*, **53**, 1015, (2010).
15. D.C. Groeneveld et al., *Nucl Eng.*, **163**, 1, (1996).
16. Y.H. Jeong, M.S. Sarwar, S.H. Chang, *Int. J. Heat Mass Trans.*, **51**, 1913, (2008)
17. Y.H. Jeong, W.J. Chang, S.H. Chang, *Int. J. Heat Mass Trans.*, **51,** 3025, (2008).
18. J. Lee, Y.H. Jeong, *Nucl. Eng. Des*., **240**, 3594, (2010)
19. G.P. Celata, K. Mishima, G. Zummo, *Int. J. Heat Mass Trans.*, **44**, 4323, (2001).
20. Henderson K, Park YG, Liu L, Jacobi AM. *Int. J. Heat Mass Trans*., **5**, 944, (2010).
21. E. A. H. Abdel-Hadi, S. H. Taher, A. M. Torki, S. S. Hamad, *International Conference on Advanced Materials Engineering*, **15**, 80, (2011).

22. R. Saidur, K.Y. Leong, H.A. Mohammad, *Renewable Sustainable Energy Rev.* **15** 1646, (2011).
23. J. F. Seara, F. J. Uhia, J. Sieres, *Exp. Heat Trans.*, **20**, 123, (2007).
24. S. J. Kline, F.A. McClintock, *Mech. Eng.*, **75**, 3, (1953).

КАЧЕСТВЕНО ИЗСЛЕДВАНЕ НА КОНВЕКТИВНОТО ТОПЛОПРЕНАСЯНЕ С КИПЕНЕ В РАЗРЕДЕНИ СУСПЕНЗИИ НА AL_2O_3 ВЪВ ВОДНО-ГЛИЦЕРОЛОВИ СМЕСИ ВЪВ ВЕРТИКАЛНО ПРЪСТЕНОВИДНО ПРОСТРАНСТВО

М.М. Сарафраз [*], Ф. Хормози

Факултет по химично, нефтено и газово инженерство, Университет Семнан, Иран

Постъпила на 18 юли, 2013 г.; коригирана на 22 февруари, 2014 г.

(Резюме)

Експериментално е изследвано топлопренасянето и е определен коефициента на топлопренасяне при кипене на суспензии от наночастици на Al_2O_3 във водно-глицеролови смеси при различни работни условия. Влиянието на различни работни параметри като топлинния поток, масовия поток и температурата на охлаждане, както и концентрацията на наночастици върху коефициента на топлообмен е изследвано и обсъдено. Резултатите показват, че са налице две различни области на топлопренасяне на конвективен пренос с различни механизми на преносния процес: принудени конвекции в една фаза и дву-фазно кипене със зародишообразуване. Резултатите показват също така, че коефициентът на топлопренасяне нараства с нарастване на топлинния и масовия поток, докато той намалява с нарастване концентрацията на наночастиците. Това се обяснява с отлагането на наночастици върху топлообменната повърхност. Температурата на охлаждане влияе единствено върху възникването на зародиши на кипене.

Bulgarian Chemical Communications, Volume 46, Number 3(pp. 652– 657) 2014

Numerical simulation and experimental investigation of mass transfer in liquid-liquid jets

A. Mirzazadeh ghanadi [1*], A.Heydari nasab [1], D. Bastani [2]

[1]*Department of Chemical Engineering, Science and Research Branch , Islamic Azad University, Tehran, Iran*
[2]*Department of Chemical and Petroleum Engineering, Sharif University of Technology, Tehran, Iran*

Received August 23, 2013; Revised December 19, 2013

This paper covers investigation of nozzle diameter and jet velocity effects on mass transfer coefficient under jetting mode by using experimentation and numerical simulation. For this purpose, a chemical system of n-butanol–succinic acid–water was selected and then vertical liquid jet, containing n-butanol and succinic acid, was injected from nozzles (with inside diameters of 1, 2, and 5 mm) into continuous liquid phase (water) axsimmetrically. The level set method was applied for numerical simulation of mass transfer between the liquid jet and the continuous liquid. It was revealed that the results obtained from numerical simulation are in good agreement with experimental data and the mean overall mass transfer coefficient for jet mode is on the scale of 10^{-3} m/s. Also the results of both experimental data and numerical simulation indicate that the overall mass transfer coefficient of the jetting mode is almost one hundred times greater than that of the dropping mode.

Key words: liquid- liquid extraction; jetting mode; mass transfer; numerical simulation.

INTRODUCTION

Many industrial chemical processes include multiphase flows (e.g. multiphase flow reactors, liquid-liquid extraction, etc) that can be categorized as liquid-solid, gas-liquid and liquid-liquid flows. From fluid mechanics aspects, multiphase flows can be taken into account in a mixture in the separated phase from at some scales quite above the molecular level [1]. By moving from one phase to other ones, interfaces and physical properties changes and a complicated behavior is seen near the interface that has not been observed in the single phases.

In a liquid-liquid extraction system it is assumed that a liquid jet is injected into an immiscible liquid phase without any reaction. When a liquid jet is injected with a low velocity from an orifice into a stationary continuous liquid phase, droplets are formed on the outlet of the orifice and no jet is observed. By increasing the velocity at drops change to jet whose length becomes greater with increasing the velocity. When the velocity reaches a maximum, the jet axisymmetric form becomes unstable and the jet begins to break up. Kitamura and Takahashi [2] studied the length of the jet as a function of velocity and various observations of the breakup modes.

It is noteworthy to say that in multiphase flows, before solving the mass transfer equations, interface problem should be solved. There are various methods in literature for solving the convection-diffusion equations under multiphase flows condition. Kim *et al.* [3] studied on phase-field model for breaking up liquid-liquid jet in comparison with experimental data. Numerical simulation on an axisymmetric jet in liquid-liquid systems was studied by Richards et al. [4-6], using volume of fluid method. Homma *et al.* [7] utilized direct numerical simulation for solving the Navier Stokes equations by using the front-tracking method. In all aforementioned works the formation of a liquid jet and its break up into droplets in another immiscible liquid were considered. Most of the researches conducted on mass transfer in two-phase flow focus on the droplets and fewer works were done with respect to the jetting mode. Mass transfer across a moving droplet was simulated by adopting a two stage approach (Deshpande and Zimmerman [8]) which decouples the convection-diffusion equations from the governing equations at the level set method. Mass transfer coefficients obtained from simulations are found to be in the same order of magnitude as those obtained by using empirical correlations. Front-tracking method for computations of interfacial flows with soluble surfactants was studied by Muradoglu and Tryggvason [9]. They studied the axisymmetrical motion and deformation of a moving viscous drop

---

* To whom all correspondence should be sent:
E-mail: asgharmirzazadeh@yahoo.com

in a circular tube. Also Marangoni effect with mass transfer in single drops (Wang *et al*. [10]) and during drops formation (Wang *et al*. [11]) were simulated in liquid –liquid extraction by level set method. Hysing [12] developed mixed element FEM level set method for numerical simulation of a rising bubble in an immiscible fluid and then compared the results of simulation with those of some commercial softwares. Using the level set method, mass transfer during drops formation was studied by Lu *et al*. [13] for a chemical system of MIBK–acetic acid–water and good agreement between experimental and simulation results was observed. It is clear that all the mentioned methods have some advantages and disadvantages that make them appropriated or unsuitable for solving various types of problems. For example, in the volume of fluid method since the interface is represented in terms of volume fraction, it is necessary to consider mass conservation issues. For this, reconstruction algorithm is used that causes the numerical solution more complicated. Also in the front-tracking method, rigridding algorithm is employed which gives more complex computations.

In this paper to investigate the mass transfer in liquid-liquid extraction in the jetting mode without breakup, laboratory experiments were conducted and simultaneously the jet system was simulated by using numerical methods. It should be noted that to give less complicated calculations, the level set method is used in the numerical simulation.

The governing equations

The level set method (Osher [14], Sethian [15]) is based on a function (φ) which describes the evolution of the interface between two phases. Motion of the interface is solved by level set function (φ), represented as equation (1).

$$\varphi_\tau + u.\nabla\varphi = 0 \tag{1}$$

where φ_τ is level set function transformed by the advection equation and u is the fluid velocity.

Fluid pressure and velocity are obtained by solving the incompressible Navier Stokes and continuity equations as equation (2) and equation (3), respectively.

$$\rho(\frac{\partial u}{\partial t} + u.\nabla u) - \nabla.\mu(\nabla u + (\nabla u)^T) = -\nabla p + \rho g + \sigma\kappa\delta\text{n} \tag{2}$$

$$\nabla u = 0 \tag{3}$$

Where σ is the surface tension, n and δ are unit normal and Dirac delta function, respectively. κ stands for the local interfacial curvature and expressed as equation (4).

$$\kappa_{(\varphi)} = \nabla.\text{n} = -\nabla.(\frac{\nabla\varphi}{|\nabla\varphi|}) \tag{4}$$

$$|\nabla\varphi| = \sqrt{(\frac{\partial\varphi}{\partial x})^2 + (\frac{\partial\varphi}{\partial y})^2} \tag{5}$$

Fluid density, ρ, and viscosity, μ, can be defined by using Heaviside function as follows :

$$\rho_{(\varphi)} = \rho_{(c)}H_{(\varphi)} + \rho_{(d)}(1 - H_{(\varphi)}) \tag{6}$$

$$\mu_{(\varphi)} = \mu_{(c)}H_{(\varphi)} + \mu_{(d)}(1 - H_{(\varphi)}) \tag{7}$$

H is Heaviside function, a smoothed function written in different ways, expressed by Sussman *et al*. [16, 17] as equation (8).

$$H_{(\varphi)} = \begin{cases} 0 & \text{if} \quad \varphi < -\varepsilon \\ \frac{1}{2} & \text{if} \quad |\varphi| = \varepsilon \\ 1 & \text{if} \quad \varphi > \varepsilon \end{cases} \tag{8}$$

where ε is the thickness of interface.

Mass transfer from dispersed phase to continuous one, including convection and diffusion, can be expressed as equation (9).

$$\frac{\partial C_A}{\partial t} + u.C_A = D_A\nabla^2 C_A \tag{9}$$

where C_A and D_A are concentration and diffusion coefficient of species A, respectively. D_A can be obtained as:

$$D_{A(\varphi)} = D_{Ac(\varphi)} + D_{Ad(\varphi)}(1 - H_{(\varphi)}) \tag{10}$$

where D_{Ac} and D_{Ad} are the solute diffusion coefficients in the continuous and dispersed phases, respectively.

EXPERIMENTAL SECTION

The experimental apparatus shown in Figure 1 consists of the following parts: (1) a cylindrical vessel with 10 cm inside diameter and 50 cm height. (2) three glass nozzles with 1, 2 and 5 mm inside diameters. (3) syringe pump with adjustable flow rate. (4) syringe with the volume of 50 cc.

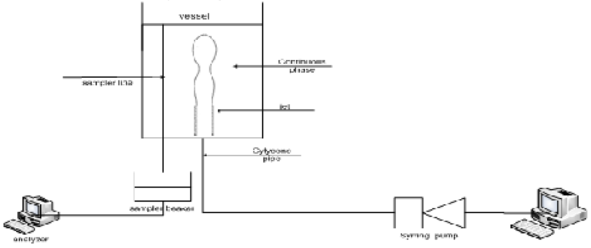

Fig 1. Scheme of experimental apparatus

The chemical system was chosen according to standard test system, recommended by EFCE, which contains succinic acid (99%), deionized

Table 1. Physical properties of continuous phase and dispersed phase

ρ_c (kg/m^2)	ρ_d (kg/m^2)	μ_c (kg/m.s)	μ_d (kg/m.s)	σ (N/m)	D_c (m^2/s)	D_c (m^2/s)
989	852	0.00146	0.0034	1.3x10^{-10}	5.2x10^{-10}	2.1x10^{-10}

water and *n*-butanol (99%). Prior to the experimentation, deionized water and n-butanol were saturated by each other to prevent the effect of partial solution on the mass transfer. The amount of succinic acid transferred from the organic phase into the aqueous phase was analyzed by titration using 0.1N sodium hydroxide in the presence of phenolphthalein indicator, while the concentration of succinic acid in inlet was kept 1 wt%. It should be noted that all chemicals used in the experiments are laboratory grade produced by Merck. The physical properties of the system are obtained as below and listed in Table 1.

1-Densities of the saturated aqueous and organic solution were measured by a picnometer in 20 °C.

2- Viscosities of the saturated aqueous and organic solution were measured by an Ostwald viscometer in 20 °C.

3-Interfacial tension and diffusivity coefficients of succinic acid in aqueous and organic phases are provided by EFCE.

According to EFCE, distribution coefficient of solute (succinic acid) between aqueous and organic phases is approximately considered as 1. The height of continuous phase in vessel should be kept at approximately 4 cm, in which the injected jet neither break nor drop.

RESULTS AND DISCUSSION

Numerical simulation

A jet with initial velocity, u, surrounded by an incompressible Newtonian fluid is considered and the velocity is adjusted to prevent jet breaking. Mean overall mass transfer coefficient, $k_{moA,com}$, between disperse and continuous phases is computed as equation (11).

$$k_{moA,com} = \frac{\overline{N_A}}{\overline{C_{A,d}} - \overline{C_{A,c}}} \tag{11}$$

where $\overline{C_{A,c}}$ and $\overline{C_{A,d}}$ are average concentrations of succinic acid in continuous (water) and disperse (n-butanol) phases, respectively defined as:

$$\overline{C_{A,c}} = \frac{\iiint_{\varphi>0.1} C_A \mathrm{dV}}{\iiint_{\varphi>0.1} \mathrm{dV}} \tag{12}$$

$$\overline{C_{A,d}} = \frac{\iiint_{\varphi<0.1} C_A \mathrm{dV}}{\iiint_{\varphi<0.1} \mathrm{dV}} \tag{13}$$

$$\mathrm{N_A} = \mathrm{J} = -\mathrm{n}.D_A \nabla C_A \tag{14}$$

$\mathrm{N_A}$ is total mass flux at the interface that can be equal with diffusive flux(J).

$$\overline{\mathrm{N}}_{A,\varphi=0.1} = \frac{\iint_{\varphi=0.1} \mathrm{N_A dA}}{\iint_{\varphi=0.1} \mathrm{dA}} \tag{15}$$

$\overline{\mathrm{N}}_A$ is average flux on surface area at a place where level set function is equal to one tenth $(\varphi = 0.1)$.

In this work, these assumptions for numerical modeling of the jet system were applied:

1- Jet velocity and pressure are kept constant.

2- Jet form is axisymmetric which leads to a constant interfacial area.

3- Concentration has no effect on surface tension.

4- Viscosities and densities are constant.

The numerical simulation was conducted by using finite element method in COMSOL software. For this purpose, five steps were taken. in the first step, the vessel with nozzle was drawn by a rectangular in 2D to consider the jet axial symmetric motion in the vessel. In the second step, the object was meshed by using triangle meshes. Equations and boundary conditions were set in the third step. In the fourth step the simulation was run with time step 0.01s and the solution method of BDF (backward differentiation formula). Finally, concentration and flux profiles were studied for each nozzle.

Mesh size influences were investigated for a nozzle with 1 mm inside diameter and it was shown (Figure 2) that beyond the mesh number of 4000, the mean overall mass transfer coefficient reaches the smooth mode, so no more increase in mesh number is needed.

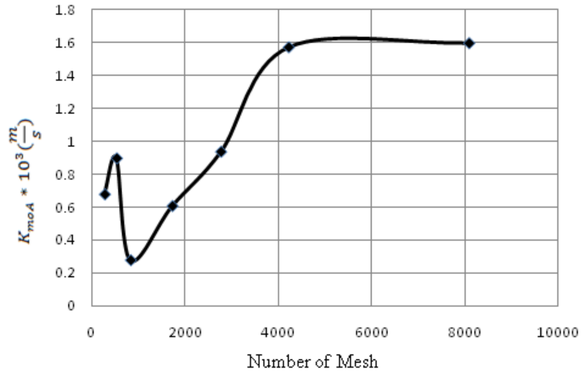

Fig 2. Independence test: mean overall mass transfer coefficient versus mesh grid.

Table 2. Kinds of boundary conditions with boundary equations

Boundary conditions	Kind of the boundaries	momentum	mass
1	Axial symmetry	Axial symmetry	Axial symmetry
2	inlet	$u = u_0 \mathrm{n}$	$C_{A,i} = C_{A,0}$
3	open	$\left[-pI + \mu(\nabla u + (\nabla u)^T)\right]\mathrm{n} = 0$	$-\mathrm{n}.D_A \nabla C_A = 0$
4,5	wall	$u = 0$	$-\mathrm{n}\mathrm{N}_A = 0$

Boundary conditions are shown in the schematics in Figure 3. Two groups of boundary conditions were applied; the first one is related to momentum transfer and the other one is in connection with mass transfer. Table 2 demonstrates employed boundary conditions in this system.

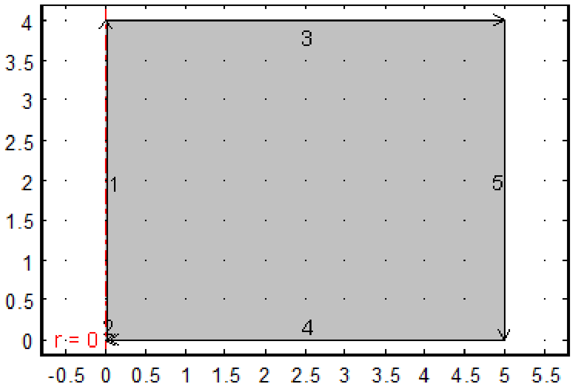

Fig 3. Boundary conditions for system

Experimental results

The mean overall mass transfer coefficient is defined by the following equation

$$R = Q_A (C_{A,i} - C_{A,o}) = k_{moA} S \Delta C_m \qquad (16)$$

where is mean concentration driving force that usually is a logarithmic average.

$$\Delta C_m = \frac{(C_{A,i} - C_{A,i}^{*}) - (C_{A,o} - C_{A,o}^{*})}{\ln[\frac{(C_{A,i} - C_{A,i}^{*})}{(C_{A,o} - C_{A,o}^{*})}]} \qquad (17)$$

$C_{A,i}^{*}$ and $C_{A,o}^{*}$ are the concentrations in equilibrium with continuous phase in the inlet and the outlet, respectively. Since the continuous phase volume is bigger than that of dispersed phase, external resistance becomes negligible compared to internal one.

In equation 14 *R*, Q_A, *S* are the extraction rate, the volumetric flow rate of disperse phase, and the mass transfer surface area, respectively. As shown in Figure 4 the experiments were conducted under jetting mode without any breakup.

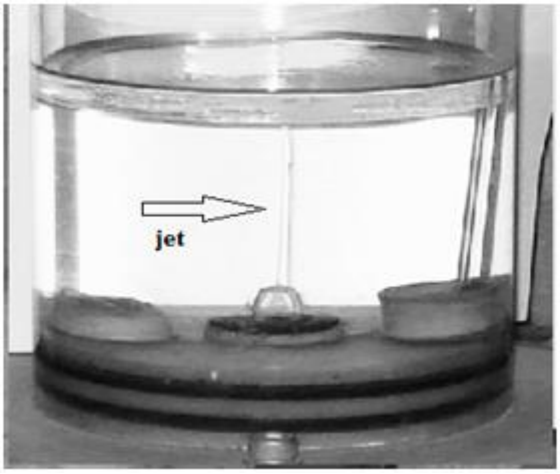

Fig 4. Jetting mode for experimental condition

Comparison between experimental data and numerical simulation results

Figure 5 depicts a comparison between the shapes resulted from numerical simulation and those obtained from experiments. In Figure 5 the image shown in bottom demonstrates the picture of the jet in real size, taken by a high speed camera, and the one shown at the top depicts the results of numerical calculations. As it can be seen in Figure 5 there is a good agreement between numerical simulation and experimental data.

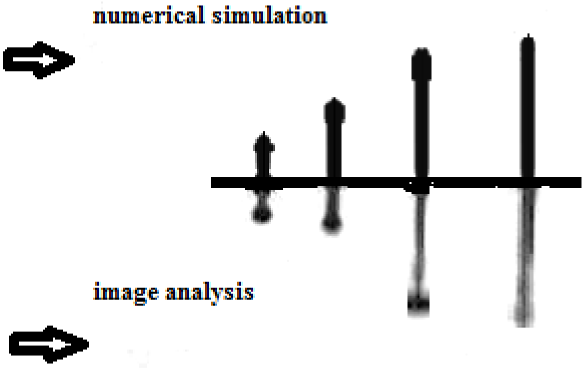

Fig 5. Comparison between numerical simulation results and real picture of the jet.

The experimental and numerical analysis for the effect of nozzle inside diameter in various velocities is shown in Figure 6. It can be observed in Figure 6, mean overall mass transfer coefficient enhances with increasing jet velocity, whereas it decreases with increasing nozzle diameter.

As shown in Figure 6 the mean overall mass transfer coefficient for jet mode is in the scale of while this quantity for a nozzle with the same diameter size is calculated in the scale of for dropping mode [18, 19]. This enhancement in overall mass transfer coefficient from dropping mode to jetting one can be explained by penetration theory. In this theory the overall mass transfer coefficient is inversely proportional to the exposed time, so by increasing the velocity of the dispersed phase, which leads to the reducing of the exposed time, the overall mass transfer coefficient enhances. Also it can be seen in Figure 6 that with increasing the nozzle diameter the mean overall mass transfer coefficient decreases. This observation can be attributed to the fact that in cylindrical systems when the characteristics length increases, the mass transfer coefficient decreases expressed as follows:

$$Sh=CRe^{m}Sc^{n}, \qquad m < 1 \qquad (18)$$

Also it can be found from Fig. 6 that the maximum deviation between numerical simulation and experimental results for k_{moA} is ±10%, indicating good agreement between calculated results and numerical data.

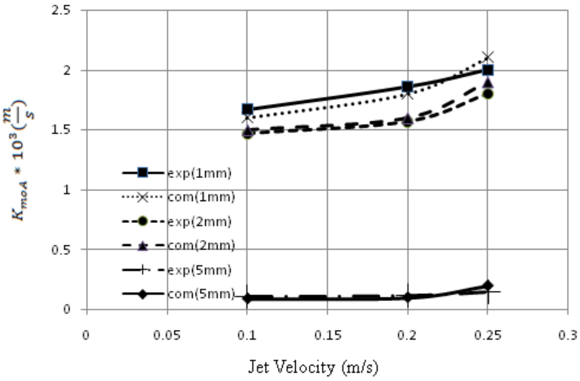

Fig 6. Comparison between experimental data and numerical simulation

CONCLUSIONS

A level set method is used for numerical simulation of mass transfer from a stable jet which moves in a continuous immiscible liquid without any break up. At constant velocity and continuous phase height, with increasing the nozzle diameter the mass transfer coefficient decreases. When no mode change occurs, with increasing the dispersed phase velocity, the mass transfer coefficient increases at constant height and nozzle diameter. By changing the mode from dropping to jetting, mass transfer coefficient increases with increasing the dispersed phase velocity at constant height and nozzle diameter.

REFERENCES

1. G. H. Yeoh, J. Tu. Computational Techniques for Multi-phase Flows .Inst.Chem.Eng, 2010.
2. Y. Kitamura, T. Takahashi. Encyclopedia. fluid mechanics, vol.2Gulf, Houston.1986.
3. C. H. Kim, S. H. Shin, H.G. Lee , J .Kim. J. Korean .Physical. Society, 55,4 (2009) 1451-1460.
4. J.R. Richards, A.N. Beris, A.M. Lenhoff, . Phys. Fluids. A ,5 (1993) 1703–1717.
5. J.R Richards,. A.M.Lenhoff, , A.N. Beris,. Phys. Fluids., 6 (1994) 2640–2655.
6. J.R. Richards, A.N. Beris, A.M.Lenhoff. Phys.Fluids. 7 (1995) 2617–2630.
7. S. Homma, J. Koga, S. Matsumoto, M. Song, G. Tryggvason. Chem. Eng. Sci. 6(2006) 3986-3996.
8. K. B. Deshpande, W.B Zimmerman. Chem.Eng. Sci. 61(2006) 6486-6498.
9. M. Muradoglu , G. Tryggvason. J. Comp. phys .227 (2008) 2238-2262.
10. S. Hysing, J. Com.phys.231 (2012) 2449-2465.
11. J.F.Wang, C.Wang, Z.S. Mao.Sci. China. 51 (2008) 684-694.
12. Z.Wang, P. Lu, Y. Wang, C. Yang, Z.S. Mao. AICH.59 (2013) 4424-4439.
13. P.Lung, Z.Wang, C.Yang, Z.S.Mao, Chem. Eng .Sci.65 (2010) 5517-5526.
14. S. Osher, J. A. Sethian. .J. Com.phys.79, 1 (1988) 12-49.
15. J. A. Sethian., Cambridge, (1999) p.1-60.
16. M. Sussman, E. Fatemi, P.Smereka, S. Osher. Fluids. Comp. phys. 27 (1998) 663-680.
17. M. Sussman , P.Smereka , S. Osher .J. Com.phys.114 (1994) 146-159.
18. C. Yang, Z,S Mao. Chem. Eng .Sci.60 (2005) 2643-2660.
19. J. Wang, P. Lu, Z .Wang, C. Yang, Z..S. Mao. Chem. Eng. Sci.63 (2008) 3141 – 3151.

..1

ЧИСЛЕНО СИМУЛИРАНЕ И ЕКСПЕРИМЕНТАЛНО ИЗСЛЕДВАНЕ НА МАСОПРЕНАСЯНЕТО В ТЕЧНО-ТЕЧНИ СТРУИ

А. Мирзазадеганади[1*], А. Хейдаринасаб[1], Д. Бастани [2]

[1]*Департамент по инженерна химия, Научни-изследвателски клон, Ислямски университет «Асад», Техеран, Иран*

[2]*Департамент по инженерна химия и нефтохимия, Технологичен университет “Шариф”, Техеран, Иран*

Постъпила на 23 август, 2013 г.; коригирана на 19 декември, 2013 г.

(Резюме)

Работата засяга изследването влиянието на на диаметъра на отверстието и скоростта на струята върху коефициента на масопренасяне чрез числено симулиране и експерименти. Използвана е системата n-бутанол–янтарна киселина-вода. Вертикални струи от сместа n-бутанол–янтарна киселина са инжектирани през отверстия с вътрешен диаметър от 1, 2 и 5 mm) във вода като непрекъсната фаза. Установено е, че резултатите от симулирането са в добро съгласие с опитните данни. Осредненият общ коефициент на масопренасяне са струйно течение е около 10^{-3} m/s. Освен това и двете групи резултати показват, че общият коефициент на масопренасяне при струйно течение е почти 100 пъти по-голям, отколкото при капково течение.

ERRATUM

We apologise for an error that occurred in the CONTENT of v. 46(2), 2014 of the journal.
Two papers were inadvertently omitted from the list, namely:

The revised list has been published online.

BULGARIAN CHEMICAL COMMUNICATIONS

Instructions about Preparation of Manuscripts

General remarks: Manuscripts are submitted in English by e-mail or by mail (in duplicate). The text must be typed double-spaced, on A4 format paper using Times New Roman font size 12, normal character spacing. The manuscript should not exceed 15 pages (about 3500 words), including photographs, tables, drawings, formulae, etc. Authors are requested to use margins of 3 cm on all sides. For mail submission hard copies, made by a clearly legible duplication process, are requested. Manuscripts should be subdivided into labelled sections, e.g. **Introduction, Experimental, Results and Discussion**, *etc*.

The title page comprises headline, author's names and affiliations, abstract and key words.

Attention is drawn to the following:

a) **The title** of the manuscript should reflect concisely the purpose and findings of the work. Abbreviations, symbols, chemical formulas, references and footnotes should be avoided. If indispensable, abbreviations and formulas should be given in parentheses immediately after the respective full form.

b) **The author**'s first and middle name initials, and family name in full should be given, followed by the address (or addresses) of the contributing laboratory (laboratories). **The affiliation** of the author(s) should be listed in detail (no abbreviations!). The author to whom correspondence and/or inquiries should be sent should be indicated by asterisk (*).

The abstract should be self-explanatory and intelligible without any references to the text and containing not more than 250 words. It should be followed by key words (not more than six).

References should be numbered sequentially in the order, in which they are cited in the text. The numbers in the text should be enclosed in brackets [2], [5, 6], [9–12], etc., set on the text line. References, typed with double spacing, are to be listed in numerical order on a separate sheet. All references are to be given in Latin letters. The names of the authors are given without inversion. Titles of journals must be abbreviated according to Chemical Abstracts and given in italics, the volume is typed in bold, the initial page is given and the year in parentheses. Attention is drawn to the following conventions:

a) The names of all authors of a certain publications should be given. The use of "*et al.*" in the list of references is not acceptable.

b) Only the initials of the first and middle names should be given.

In the manuscripts, the reference to author(s) of cited works should be made without giving initials, e.g. "Bush and Smith [7] pioneered...". If the reference carries the names of three or more authors it should be quoted as "Bush *et al*. [7]", if Bush is the first author, or as "Bush and co-workers [7]", if Bush is the senior author.

Footnotes should be reduced to a minimum. Each footnote should be typed double-spaced at the bottom of the page, on which its subject is first mentioned.

Tables are numbered with Arabic numerals on the left-hand top. Each table should be referred to in the text. Column headings should be as short as possible but they must define units unambiguously. The units are to be separated from the preceding symbols by a comma or brackets.

Note: The following format should be used when figures, equations, *etc*. are referred to the text (followed by the respective numbers): Fig., Eqns., Table, Scheme.

Schemes and figures. Each manuscript (hard copy) should contain or be accompanied by the respective illustrative material as well as by the respective figure captions in a separate file (sheet). As far as presentation of units is concerned, SI units are to be used. However, some non-SI units are also acceptable, such as °C, ml, l, etc.

The author(s) name(s), the title of the manuscript, the number of drawings, photographs, diagrams, etc., should be written in black pencil on the back of the illustrative material (hard copies) in accordance with the list enclosed. Avoid using more than 6 (12 for reviews, respectively) figures in the manuscript. Since most of the illustrative materials are to be presented as 8-cm wide pictures, attention should be paid that all axis titles, numerals, legend(s) and texts are legible.

The authors are asked to submit **the final text** (after the manuscript has been accepted for publication) in electronic form either by e-mail or mail on a 3.5'' diskette (CD) using a PC Word-processor. The main text, list of references, tables and figure captions should be saved in separate files (as *.rtf or *.doc) with clearly identifiable file names. It is essential that the name and version of the word-processing program and the format of the text files is clearly indicated. It is recommended that the pictures are presented in *.tif, *.jpg, *.cdr or *.bmp format, the equations are written using "Equation Editor" and chemical reaction schemes are written using ISIS Draw or ChemDraw programme.

The authors are required to submit the final text with a list of three individuals and their e-mail addresses that can be considered by the Editors as potential reviewers. Please, note that the reviewers should be outside the authors' own institution or organization. The Editorial Board of the journal is not obliged to accept these proposals.

EXAMPLES FOR PRESENTATION OF REFERENCES

REFERENCES

1. D. S. Newsome, *Catal. Rev.–Sci. Eng.*, **21**, 275 (1980).
2. C.-H. Lin, C.-Y. Hsu, *J. Chem. Soc. Chem. Commun.*, 1479 (1992).
3. R. G. Parr, W. Yang, Density Functional Theory of Atoms and Molecules, Oxford Univ. Press, New York, 1989.
4. V. Ponec, G. C. Bond, Catalysis by Metals and Alloys (Stud. Surf. Sci. Catal., vol. 95), Elsevier, Amsterdam, 1995.
5. G. Kadinov, S. Todorova, A. Palazov, in: New Frontiers in Catalysis (Proc. 10th Int. Congr. Catal., Budapest, 1992), L. Guczi, F. Solymosi, P. Tetenyi (eds.), Akademiai Kiado, Budapest, 1993, Part C, p. 2817.
6. G. L. C. Maire, F. Garin, in: Catalysis. Science and Technology, J. R. Anderson, M. Boudart (eds), vol. 6, Springer-Verlag, Berlin, 1984, p. 161.
7. D. Pocknell, *GB Patent* 2 207 355 (1949).
8. G. Angelov, PhD Thesis, UCTM, Sofia, 2001.
9. JCPDS International Center for Diffraction Data, Power Diffraction File, Swarthmore, PA, 1991.
10. CA **127**, 184 762q (1998).
11. P. Hou, H. Wise, *J. Catal.*, in press.
12. M. Sinev, private communication.
13. http://www.chemweb.com/alchem/articles/1051611477211.html.

CONTENTS

Bulgarian Chemical Communications, Volume 46, Number 3 2014

СЪДЪРЖАНИЕ